STUDIES OF DIBORON COMPOUNDS USING SOLID-STATE MULTINUCLEAR MAGNETIC RESONANCE SPECTROSCOPY

Ying-Tung Angel Wong

A THESIS SUBMITTED IN PARTIAL FULFILLMENT OF
THE REQUIREMENTS FOR THE DEGREE OF

MASTERS OF SCIENCE

Ottawa-Carleton Chemistry Institute
Department of Chemistry and Biomolecular Sciences
Faculty of Science
University of Ottawa

Table of Contents

Abstract

The development of diboron derivatives has gained much attention lately due to the importance and the versatility of these compounds in synthetic and materials chemistry. Since chemical behavior is governed by electronic properties, insights into the bonding nature of these systems would be highly beneficial for the rational design of function-specific diboron motifs. In this thesis, the potential of the indirect spin-spin (*J*) coupling interaction in elucidating electronic structures of B-B bonds is illustrated. The $J(^{11}B, ^{11}B)$ coupling constants of various heterocyclic diboron complexes and electron-precise diborane compounds bearing 2-center 2-electron (2c-2e) $B(sp^3)$-$B(sp^3)$ bonds were measured using ^{11}B double-quantum-filtered (DQF) *J*-resolved solid-state NMR (SSNMR) spectroscopy. Natural localized molecular orbital (NLMO) and natural bond orbital (NBO) analyses were also conducted in order to determine the electronic origin of the *J* couplings. The $J(^{11}B, ^{11}B)$ coupling constants were found to reflect a plethora of bonding properties, ranging from the hybridization state and the strength of the B-B bonds, to the electron withdrawing capacity of the functional groups attached to the boron centers. Specifically, a strong correlation was obtained between the coupling constants and the hybridization state of the boron orbitals which form the B-B bond and the strength of the B-B bonds. These results show that electronic information, and thus chemical behavior, can be directly inferred from the $J(^{11}B, ^{11}B)$ coupling constants. This is further illustrated by the studies on various diboratellurenium compounds. Using the relationship between the *J* coupling constants and the hybridization states, the B-B bond order of these com-

pounds, which was found to be ambiguous by other commonly employed experimental methods, was determined.

Moreover, given the vast interest in the dynamics studies of solids, such as the investigation of motions in molecular machines and metal organic frameworks, the development of new SSNMR techniques for probing dynamics can be valuable. In this thesis, the DQF *J*-resolved experiment is also presented as a novel tool for exploring molecular motions in solids. Using the electron-precise diborane compounds as archetypes, samples which experiences dynamic disorder were identified by ^{11}B and ^{13}C SSNMR experiments, and the results from variable-temperature (VT) experiments indicate the presence of three different motional processes in the temperature range of 248 to 306 K, occurring at a rate of 10^2 to 10^6 s^{-1}. The molecular motions were found to manifest itself in the DQF *J*-resolved spectra in a predictable manner, where the DQF *J* splittings were observed to be amplified by a factor of 3 as compared to the theoretical *J* coupling constants if (1) the borons are static and crystallographically equivalent or (2) the borons are crystallographically inequivalent but magnetically equivalent on the time scale of the experiment as a result of dynamic disorder. Consequently, dynamic disorder must be taken into consideration when analyzing the data from DQF *J*-resolved experiments in order to correctly extract the *J* coupling constants, and conversely, these experiments can potentially be employed to detect the presence of dynamics in solids.

List of Tables

List of Figures

List of Abbreviations and Symbols

2-center 2-electron 2c-2e

δ_{iso} ..... isotropic chemical shift

$\delta_{33}, \delta_{22}, \delta_{11}$ ..... principal components of the CS tensor

γ ..... gyromagnetic ratio

η ..... quadrupolar asymmetry parameter

$\hbar$ ..... reduced Planck's constant

$\widehat{H}_{Z}$ ..... Zeeman Hamiltonian

$\widehat{H}_{\sigma}$ ..... nuclear magnetic shielding Hamiltonian

$\widehat{H}_{\sigma,secular}$ ..... $\widehat{H}_{\sigma}$ formulated under the secular approximation

$\widehat{H}_{Q}$ ..... nuclear quadrupole coupling Hamiltonian

$\widehat{H}_{J}$ ..... *J* coupling Hamiltonian

κ ..... skew of the chemical shift tensor

μ ..... nuclear spin magnetic moment

$\vec{\mu}$ ..... nuclear spin magnetic moment vector

υ_0 ..... Larmor frequency

Ω ..... span of the chemical shift tensor

Ω ..... apparent Larmor precession frequency

$\sigma_{XX}, \sigma_{YY}, \sigma_{ZZ}$ ..... principal components of the magnetic shielding tensor

σ_{ZZ}^{PAS} ..... z-component of the shielding tensor expressed in the PAS

σ_{iso} ..... isotropic average of the magnetic shielding tensor

τ^{-1} ..... rate of motion

θ, θ_R, β and φ ..... angles

ψ ..... wavefunction

B_0 ..... external static magnetic field strength

$\vec{B}_0$ ..... external static magnetic field vector

B_1 ..... RF magnetic field

$\vec{B}_1$ ..... RF magnetic field vector

C_Q ..... nuclear quadrupolar coupling constant

CAAC ..... cyclic (alkyl)(amino)carbene

CMO ..... canonical molecular orbital

CS tensor ..... chemical shift tensor

CT ..... central transition

CP ..... cross polarization

DFT ..... density functional theory

DSO ..... diamagnetic spin-orbital coupling

DQF ..... double-quantum-filtered

e ..... charge of an electron

E_a ..... activation energy

E_m ..... energy of spin state m

$E_m^{(1)}$ ..... first-order quadrupolar coupling energy correction for spin state m

$E_m^{(2)}$ ..... second-order quadrupolar coupling energy correction for spin state m

EFG ..... electric field gradient

FC ..... Fermi-contact coupling

FC/SD ..... Fermi-contact coupling spin-dipolar coupling cross-term

FID ..... free induction decay

FT ..... Fourier transform

FWHM ..... full width at half maximum

GGA ..... generalized gradient approximation

h ..... Planck's constant

I ..... nuclear spin quantum number

$\hat{I}$ ..... nuclear spin angular momentum operator

$\hat{I}_z$ ..... z-component of the nuclear spin angular momentum operator

IDip ..... 1,3-bis[diisopropylphenyl]imidazole-2-ylidene

$\boldsymbol{J}$ ..... J coupling tensor

J_{iso} ..... isotropic component of the J coupling tensor

ΔJ ..... anisotropic component of the J coupling tensor

J coupling ..... indirect spin-spin coupling

KS ..... Kohn-Sham

LDA ..... local density approximation

m ..... magnetic quantum number

M_0 ..... magnitude of the net magnetization vector

M_x and M_y ..... x- and y- components of the net transverse magnetization

MAS ..... magic angle spinning

NBO ..... natural bond orbital

NHC ..... N-heterocyclic carbenes

NLMO ..... natural localized molecular orbital

NMR ..... nuclear magnetic resonance

p ..... nuclear spin angular momentum

PAS ..... principal axis system

PBE ..... Perdew, Burke and Ernzerhof

PSO ..... paramagnetic spin-orbital coupling

Q ..... electric quadrupole moment

$\boldsymbol{q}$ ..... EFG tensor

RF ..... radiofrequency

SD ..... spin-dipolar coupling

SSNMR ..... solid-state NMR

ST ..... satellite transition

T_1 and T_2 ..... longitudinal and transverse relaxation time constants

VT ..... variable-temperature

V_{XX}, V_{YY} and V_{ZZ} ..... principal components of the EFG tensor

XC ..... exchange correlation

ZORA ..... zeroth order regular approximation

Acknowledgements

The past two years have been a challenging, yet rewarding, experience. When I first started, I knew absolutely nothing about NMR spectroscopy besides the basic fundamental principles that I've learned during my undergraduate studies. Nonetheless, my understanding of the technique has greatly expanded during this degree thanks to the help and support of many individuals. Firstly, I'd like to thank my supervisor Prof. David Bryce for introducing me to such an interesting field. Without his patience and support, the work presented in this thesis would not have been possible. I'd also like to thank all the current and past members of the Bryce lab whom I have had the honor of working with. Dr. Libor Kobera, thank you for all of your help (especially for staying late on Fridays to help me set up experiments and for all the times you had to get my rotor out of the probe because my sample spilled) and for teaching me various practical and theoretical aspects of SSNMR. Dr. César Leroy, even though you've only recently joined the lab, nevertheless, you've provided countless valuable inputs and comments, all of which were greatly appreciated. I'd also like to acknowledge the graduate students in the Bryce lab: Yijue (Collette) Xu, Peter Werhun, Scott Southern and Patrick Szell. Collette, thanks for always selflessly helping me with my experiments and thanks for introducing me to various coffee shops on campus, even though the paths to these places were unsettling most of the time. Peter, thanks for all your support and for always checking up on me when I was working late, I will forever remember our Beyoncé sing-alongs. Scott, thank you for all of your help regarding computations, and Pat, thank you for all your valuable com-

ments regarding my work. I would also like to extend my gratitude to the members of our NMR facility, Dr. Glenn Facey and Dr. Gang (Eric) Ye for their support, especially for their help with setting up the VT experiments.

Of course, our collaborators played a key role in the works presented, therefore I'd like to thank Prof. Holger Braunschweig, Dr. Bill Ewing, Theresa Dellermann for providing the diboratellurenium compounds and the corresponding X-ray diffraction data, and Prof. Maik Finze and Johannes Landmann for providing the hexacyanodiborane(6) dianion salts and for performing various analysis that were essential for the publication.

I'd also like to acknowledge my committee members for taking the time to re-viewing my thesis.

Lastly, I'd like to thank Victor Yin for correcting all my misuses of plurals and for always supporting and believing in me when I need it the most. Vic, I love you.

Statement of Originality

I hereby certify that the work and research presented in this thesis are my own, except as specified explicitly or acknowledged through standard scientific referencing. Johannes Landmann and Prof. Maik Finze are acknowledged for providing the hexacyanodiborane(6) dianion salts and for conducting the corresponding characterization using powder X-ray diffraction and single-crystal X-ray diffraction. Dr. Bill Ewing, Theresa Dellermann and Prof. Holger Braunschweig are acknowledged for providing the diboratellurenium compounds and the corresponding single-crystal X-ray diffraction data.

The studies performed on the hexacyanodiborane(6) dianion salts presented in this thesis are based on the work published in and the corresponding figures (Figures 28-40, 42 and 45) are reproduced with permission from:

Wong, Y. T. A.; Landmann, J.; Finze, M.; Bryce, D. L. Dynamic Disorder and Electronic Structures of Electron-Precise Dianionic Diboranes: Insights from Solid-State Multinuclear Magnetic Resonance Spectroscopy, *J. Am. Chem. Soc.* **2017**, *139*, 8200-8211. (http://pubs.acs.org/doi/full/10.1021/jacs.7b01783) Copyright © 2017 American Chemical Society.

The article is licensed under ACS AuthorChoice, and further permissions related to this specific article should be directed to the ACS.

1 Introduction

1.1 General Theory of Nuclear Magnetic Resonance (NMR) and Solid-State NMR (SSNMR) Spectroscopy

1.1.1 Zeeman Interaction

Nuclear magnetic resonance (NMR) spectroscopy exploits the Zeeman interaction between the nuclear spin magnetic moment, μ, of nuclei which possess an intrinsic nuclear spin angular momentum, or "spin", and the external static magnetic field. Since nuclei are subatomic particles, quantum mechanics must be employed in order to describe the corresponding angular momentum. According to quantum mechanics, the angular momentum is quantized and the corresponding magnitude at any given direction can be expressed as:

$$p = \hbar m \tag{1}$$

where p is the angular momentum, $\hbar$ is the reduced Planck's constant and m is the magnetic quantum number.[1] m can take on values of I, I - 1, … -I + 1 , -I, where I is the nuclear spin quantum number; therefore, m can be related to I by:[1]

$$m = (2I + 1) \tag{2}$$

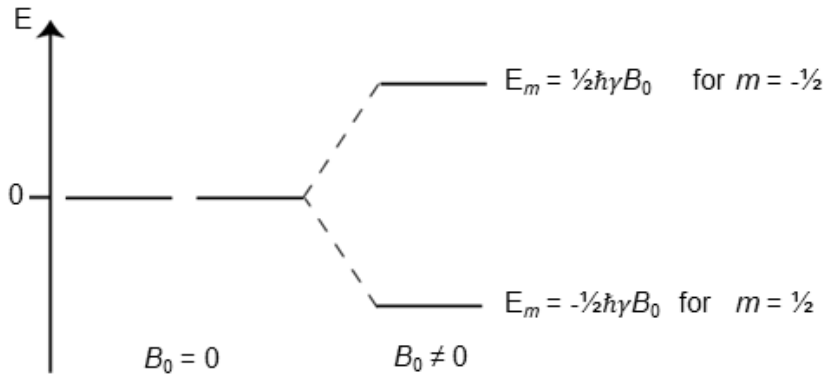

Figure 1 Energy level schemes for the m = 1/2 and m = -1/2 spin states of a spin 1/2 nucleus in the absent of an external static magnetic field ($B_0 = 0$), and in the presence of an external static magnetic field ($B_0 \neq 0$). The m = 1/2 and m = -1/2 states are no longer degenerate when $B_0 \neq 0$ due to the Zeeman interaction.

Equation 2 gives the number of allowed spin states and each state is denoted with a unique value of m. These states are degenerate in the absent of an external magnetic field (Figure 1).[2]

A non-zero spin will give rise to a nuclear spin magnetic moment, μ. When the spin is placed in an external static magnetic field, an interaction between μ and the static field will occur, and this is known as the Zeeman interaction.[2,3] The Zeeman interaction lifts the degeneracy of the spin states,[2] and the corresponding energies can be derived by solving the Schrödinger equation

$$\widehat{H}_Z\psi = E_m\psi \qquad 3$$

where $\widehat{H}_Z$ is the Zeeman Hamiltonian, ψ is the wavefunction and E_m is the energy of spin state m. $\widehat{H}_Z$ is given by

$$\hat{H}_Z = -\gamma B_0 \hat{I}_Z \quad (4)$$

where B_0 is the strength of the external static magnetic field in the z-direction (Tesla), γ is the gyromagnetic ratio (rad s^{-1} T^{-1}) and $\hat{I}_Z$ is the z-component of the nuclear spin angular momentum operator, the component which interacts with the static magnetic field.[2,3] $\hat{I}_Z$ consists of (2I+1) eigenfunctions, ψ_m, each with an eigenvalue of $m\hbar$.[3] For instance, for a spin 1/2 nucleus, there would be two eigenfunctions, $\psi_{1/2}$ and $\psi_{-1/2}$, with eigenvalues of 1/2$\hbar$ and -1/2$\hbar$, respectively. Moreover, ψ_m are also eigenfunctions of $\hat{H}_Z$, and the corresponding eigenvalues are given by $-m\hbar\gamma B_0$.[3] Therefore, in the presence of an external static magnetic field, the spin states are non-degenerate, and the corresponding energies are governed by the respective m values and B_0 (Figure 1). In NMR, the spectra are a result of energy transitions between the states with $\Delta m = \pm 1$, and the corresponding signals are observed at the Larmor frequency, υ_0, (Figure 2) which is given by[3]

$$\upsilon_0[\mathrm{Hz}] = -\gamma B_0/2\pi \quad (5)$$

From this, it can also be seen that nuclei are NMR active if and only if they have a non-zero spin (i.e. $I > 0$) since zero spin nuclei (i.e. $I = 0$) cannot participate in the Zeeman interaction and are therefore NMR silent.

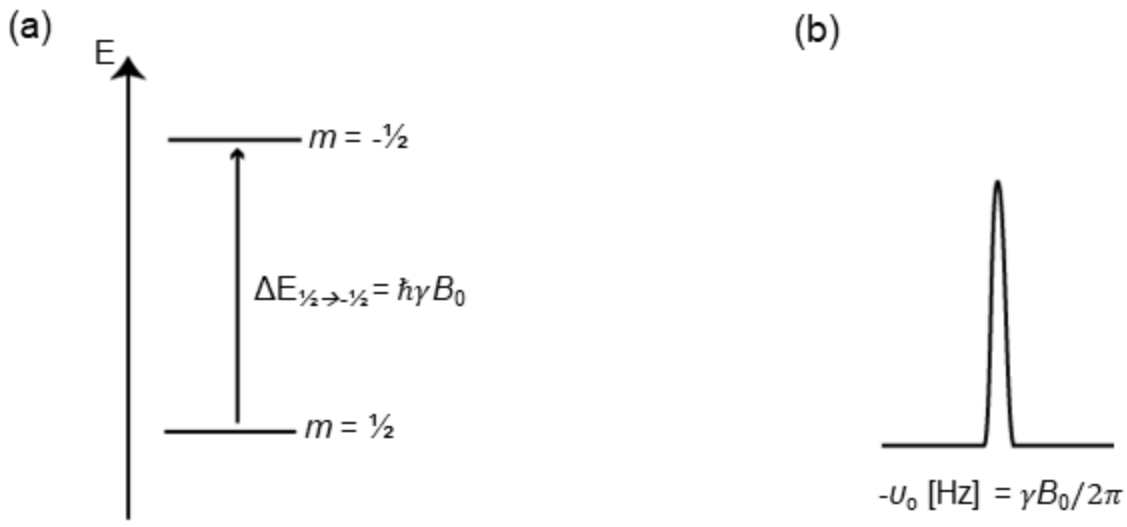

Figure 2 (a) Energy level schemes for a single spin 1/2 nucleus with a positive γ in an external static magnetic field of B_0. The transition from the m = 1/2 to the m = -1/2 state gives rise to a resonance at $-\nu_0 = \gamma B_0/2\pi$ Hz (b).

1.1.2 Internal Interactions

In a realistic sample, molecules are probed instead of a single bare nucleus; consequently, the magnetic and electric interaction which arises from the sample itself (i.e. internal interactions) must also be taken into consideration when the theory of NMR is discussed. Depending on the system, various internal interactions, such as the nuclear magnetic shielding, the nuclear quadrupole coupling and the indirect spin-spin (J) coupling, can be present. In general, the high-field approximation, in which the Zeeman interaction is considered to be dominant, can be employed and the effects of these interactions can be assessed using perturbation theory.[4,5] As such, the Hamiltonian for a system under the influence of the Zeeman interaction and internal interactions can be expressed as

$$\hat{H} = \hat{H}_0 + \hat{H}_1 \quad (6)$$

where

$$\hat{H}_0 = \hat{H}_Z \quad (7)$$

and $\hat{H}_1$ is the sum of the internal interactions present in the system, e.g.

$$\hat{H}_1 = \hat{H}_\sigma + \hat{H}_Q + \hat{H}_J \quad (8)$$

$\hat{H}_\sigma$, $\hat{H}_Q$, and $\hat{H}_J$ are the nuclear magnetic shielding, nuclear quadrupole coupling, and the *J* coupling Hamiltonians. These internal interactions are described by second-rank tensor properties since they are orientation dependent, and are commonly expressed in a molecule fixed axis system known as the principal axis system (PAS) instead of a laboratory fixed axis system. In the PAS, a general tensor, $\boldsymbol{A}$, is given as:

$$\begin{bmatrix} A_{XX} & 0 & 0 \\ 0 & A_{YY} & 0 \\ 0 & 0 & A_{ZZ} \end{bmatrix} \quad (9)$$

where A_{XX}, A_{YY}, and A_{ZZ} are known as the principal components of the tensor.[4] In solution phase NMR, only the isotropic averages (A_{iso} for a general tensor $\boldsymbol{A}$, see equation 10), which are the orientation independent components of the NMR tensors, are measured.

$$A_{\mathrm{iso}} = \frac{1}{3}(A_{\mathrm{XX}} + A_{\mathrm{YY}} + A_{\mathrm{ZZ}}) \quad (10)$$

However, in solid-state NMR (SSNMR), the anisotropic component becomes important and can influence the appearance of the corresponding spectra. Therefore, in order to properly describe the concepts behind SSNMR, a more detailed theoretical background for these internal interactions must be provided.

Nuclear Magnetic Shielding Interaction

When a molecule is placed in a magnetic field, surrounding electrons circulate, thereby generating a local magnetic field.[6] This local magnetic field shields and/or deshields the nucleus, giving rise to the nuclear magnetic shielding interaction.[4,6] For each unique nucleus in the molecule, the shielding Hamiltonian can be formulated as

$$\widehat{H}_{\sigma,\mathrm{secular}} = \gamma \hat{\mathrm{I}}_{\mathrm{z}} \sigma_{\mathrm{ZZ}}^{PAS} B_0 \quad (11)$$

using the secular approximation.[4] $\sigma_{\mathrm{ZZ}}^{PAS}$ is the z-component of the shielding tensor expressed in the PAS, which is given as[4]

$$\sigma_{\mathrm{ZZ}}^{PAS}(\theta,\varphi) = \sigma_{\mathrm{iso}} + \frac{1}{2}(\sigma_{\mathrm{ZZ}} - \sigma_{\mathrm{iso}})\left(3\cos^2\theta - 1 - \frac{\sigma_{\mathrm{YY}} - \sigma_{\mathrm{XX}}}{\sigma_{\mathrm{ZZ}} - \sigma_{\mathrm{iso}}}\sin^2\theta cos2\varphi\right) \quad (12)$$

where σ_{XX}, σ_{YY}, and σ_{ZZ} are the principal components of the shielding tensor, θ and φ are the spherical angles relating the orientation of the z-axis in the PAS to the z-axis in

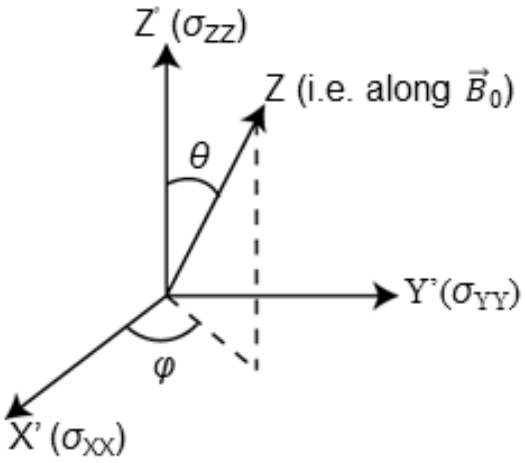

Figure 3 Orientation of the magnetic shielding PAS (Z', Y' and X') with respect to the z-axis of the laboratory-fixed axis system (Z) as described by the spherical angles θ and φ. Z is directed along the external static magnetic field vector, $\vec{B}_0$, by convention.

the laboratory-fixed axis system (Figure 3), and σ_{iso} is the isotropic average for shielding as given by:

$$\sigma_{iso} = \frac{1}{3}(\sigma_{XX} + \sigma_{YY} + \sigma_{ZZ}) \qquad 13$$

The shielding interaction thus consists of an isotropic component, and an anisotropic component which reflects the non-spherical distribution of electrons around a given nucleus.[4]

The effect of magnetic shielding on the appearance of a NMR spectrum can be described by inspecting equation 12. For solution, the anisotropic component is removed since the presence of rapid isotropic molecular tumbling averages the shielding interaction over all possible orientations.[4] Consequently, only the isotropic average (equation 13) is observed and a sharp resonance is detected (Figure 4). Since shielding is given with

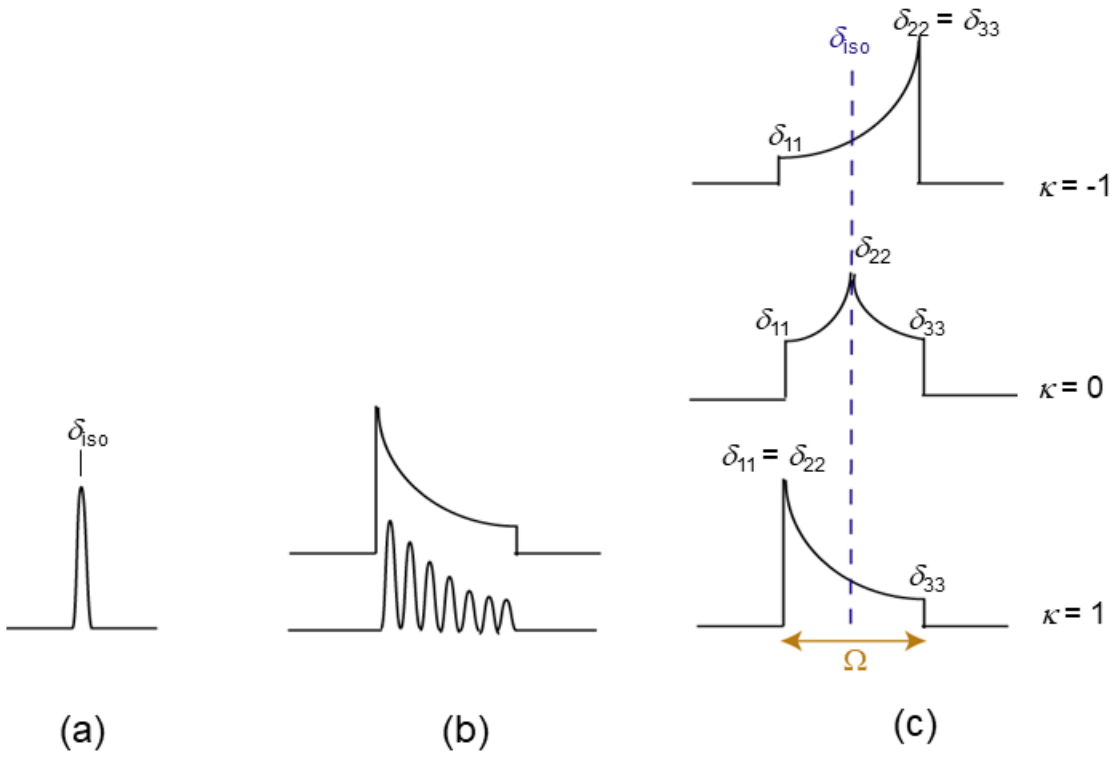

Figure 4 Depiction of NMR spectra of a spin under the influence of magnetic shielding interaction. In solution (a), only the isotropic chemical shift is observed due to rapid isotropic molecular tumbling. On the other hand, a powder pattern ((b), top) is observed instead in the solid state due to the superposition of many individual resonances that arise from different orientation of the crystallites ((b), bottom). The powder pattern can be characterized by its δ_{iso}, Ω and κ (c), where δ_{iso} gives the isotropic value, Ω gives the breadth and κ gives the asymmetry of the chemical shift tensor (δ_{11}, δ_{22}, δ_{33}).

respect to a bare nucleus, experimentally, the chemical shift relative to a standard substance is measured instead. The isotropic chemical shift (δ_{iso}) is related to σ_{iso} by[7]

$$\delta_{\mathrm{iso,sample}}\,[ppm] = \frac{\sigma_{\mathrm{iso,reference}} - \sigma_{\mathrm{iso,sample}}}{1 - \sigma_{\mathrm{iso,reference}}} \times 10^6 \qquad 14$$

On the other hand, for solids without significant amount of molecular motion (i.e. solids without dynamic disorder), shielding anisotropy can be observed and molecules with different orientations with respect to B_0 would have different $\hat{H}_{\sigma,\mathrm{secular}}$ due to distinct values

of σ_{ZZ}^{PAS} (see equation 11 and 12). Consequently, each orientation would give rise to different resonances and a powder pattern consisting of a distribution of signals would be detected for a powder sample (Figure 4).[5] The powder pattern can be described by its span (Ω) and skew (κ) :[7]

$$\Omega\,[ppm] = \delta_{11} - \delta_{33} \tag{15}$$

$$\kappa = \frac{3(\delta_{22} - \delta_{\mathrm{iso}})}{\Omega} \tag{16}$$

where $\delta_{33}, \delta_{22}, \delta_{11}$ are the principal components of the chemical shift (CS) tensor and $\delta_{11} \geq \delta_{22} \geq \delta_{33}$. Ω gives the breadth of the powder pattern and can take on any values greater than 0; whereas κ gives the asymmetry of the tensor and can take on any values between 1 and -1. For an axially symmetric tensor (i.e. $\delta_{22} = \delta_{11}$ and/or $\delta_{22} = \delta_{33}$), κ would be ± 1, and for an axially asymmetric tensor (i.e. $\delta_{22} \neq \delta_{11} \neq \delta_{33}$), κ would deviate from ± 1 (e.g. $\kappa = 0$; Figure 4).

Nuclear Quadrupole Coupling Interaction

Quadrupolar nuclei (i.e. $I > 1/2$) consist of an electric quadrupole moment, Q, due to its non-symmetrical charge distribution. For these nuclei, Q will couple with the electric field gradient (EFG) generated by the surrounding electrons and nuclei, resulting in the nuclear quadrupole coupling interaction.[4] The nuclear quadrupole coupling Hamiltonian, $\widehat{H}_{\mathrm{Q}}$, is

$$\widehat{H}_{\mathrm{Q}} = \frac{e^2 Q}{2I(2I-1)}\, \hat{I} \cdot \boldsymbol{q} \cdot \hat{I} \qquad 17$$

where $\boldsymbol{q}$ is the tensor describing the EFG at the site of the nucleus, $\hat{I}$ is the nuclear spin angular momentum operator and e is the charge of an electron.[4] The EFG tensor is a traceless property, i.e.:

$$V_{\mathrm{XX}} + V_{\mathrm{YY}} + V_{\mathrm{ZZ}} = 0 \qquad 18$$

where V_{XX}, V_{YY} and V_{ZZ} are the principal components of the EFG tensor, and $|V_{\mathrm{ZZ}}| \geq |V_{\mathrm{YY}}| \geq |V_{\mathrm{XX}}|$.[8] The EFG tensor can be described using two independent parameters: the nuclear quadrupolar coupling constant, C_{Q}

$$C_{\mathrm{Q}}[Hz] = \frac{eQV_{\mathrm{ZZ}}}{h} \qquad 19$$

, where h is Planck's constant, and the quadrupolar asymmetric parameter, η

$$\eta = \frac{V_{\mathrm{XX}} - V_{\mathrm{YY}}}{V_{\mathrm{ZZ}}} \qquad 20$$

which can take on values of $0 \leq \eta \leq 1$.[8]

In solution, the nuclear quadrupole coupling interaction does not contribute to corresponding resonance frequency since its isotropic average is zero.[4] Nonetheless, this interaction still greatly influences relaxation and thus line broadening. On the other hand, the nuclear quadrupole coupling interaction is of significant importance for solids and it often dominates the appearance of the corresponding spectra. The effect of this

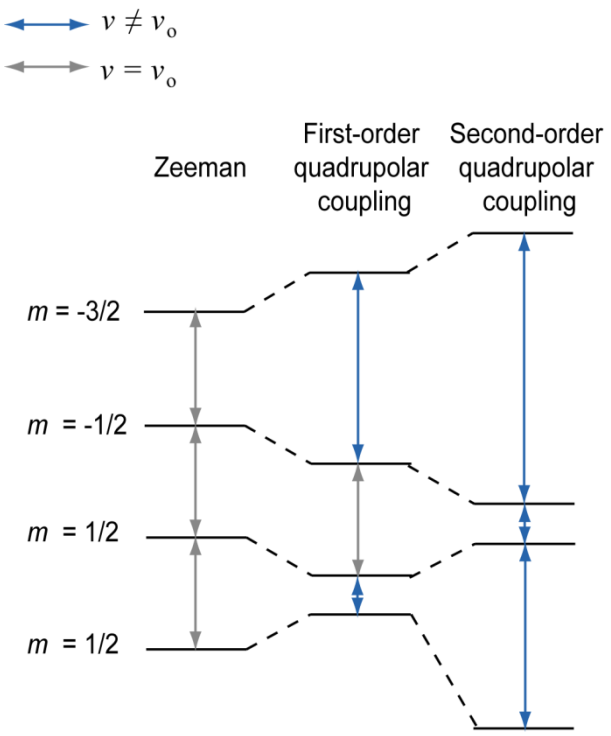

Figure 5 Perturbation of the Zeeman energy levels of a spin 3/2 nucleus by first-order and second-order quadrupolar coupling. First-order quadrupolar coupling only affects the frequency of the STs due to the m^2 dependence of $E_m^{(1)}$ (equation 21); however, second-order quadrupolar coupling influences both the STs and the CT due to the m dependence of $E_m^{(2)}$ (equation 22).

interaction on SSNMR spectra depends on its magnitude in comparison to the Zeeman interaction. For cases where the nuclear quadrupole coupling interaction is much smaller than the Zeeman interaction, first-order perturbation theory can be employed. The resulting first-order quadrupolar coupling energy correction, $E_m^{(1)}$, to the Zeeman energies for a particular spin state, m, is:[5]

$$E_m^{(1)}[Hz] = \frac{C_Q}{4I(2I-1)}(I(I+1)-3m^2)[\frac{1}{2}(3\cos^2\theta - 1) - \eta cos2\varphi(\cos^2\theta - 1)] \quad 21$$

Due to the m^2 dependence of $E_m^{(1)}$, energies for states m = 1/2 and m = -1/2 are perturbed to the same extent and the central transition (CT, m = 1/2 → m = -1/2) is unaffected by first-order quadrupolar coupling (Figure 5). However, the satellite transitions (STs) would be altered and the transition frequencies would deviate from υ_0 (Figure 5). For systems where the nuclear quadrupole coupling interaction is significant in comparison to the Zeeman interaction, second-order perturbation must be invoked in order to describe the appearance of the spectra. The second-order quadrupolar coupling energy correction is[5]

$$
\begin{aligned}
E_m^{(2)}\,[Hz] = \; & -\left(\frac{C_\mathrm{Q}}{4I(2I-1)}\right)^2 \frac{m}{\nu_0}\Big\{-\frac{1}{5}(I(I+1)-3m^2(3+\eta^2) \\
& +\frac{1}{28}(8I(I+1)-12m^2-3)[(\eta^2 \\
& -3)(3\cos^2\theta-1)+6\,\eta_Q\sin^2\theta\cos 2\varphi] \\
& +\frac{1}{8}(18I(I+1)-34m^2-5)[\frac{1}{140}(18 \\
& +\eta^2)(35\cos^4\theta-30\cos^2\theta+3) \\
& +\frac{3}{7}\eta\sin^2\theta(7\cos^2\theta-1)\;\cos 2\varphi+\frac{1}{4}\eta^2\sin^4\theta\cos 4\varphi]\Big\}
\end{aligned}
\qquad 22
$$

As seen in equation 22, second-order quadrupolar coupling energy correction depends on m instead of the m^2 which first-order quadrupolar coupling energy corrections are governed by (equation 21). Therefore, the frequencies of the STs and CT both deviate from that of the Zeeman interaction (Figure 5). Furthermore, the resonance frequency for the CT is now orientation dependent, and as a result, a powder pattern will be observed for a powder sample. For a given value of C_Q, the shape of the powder pattern will

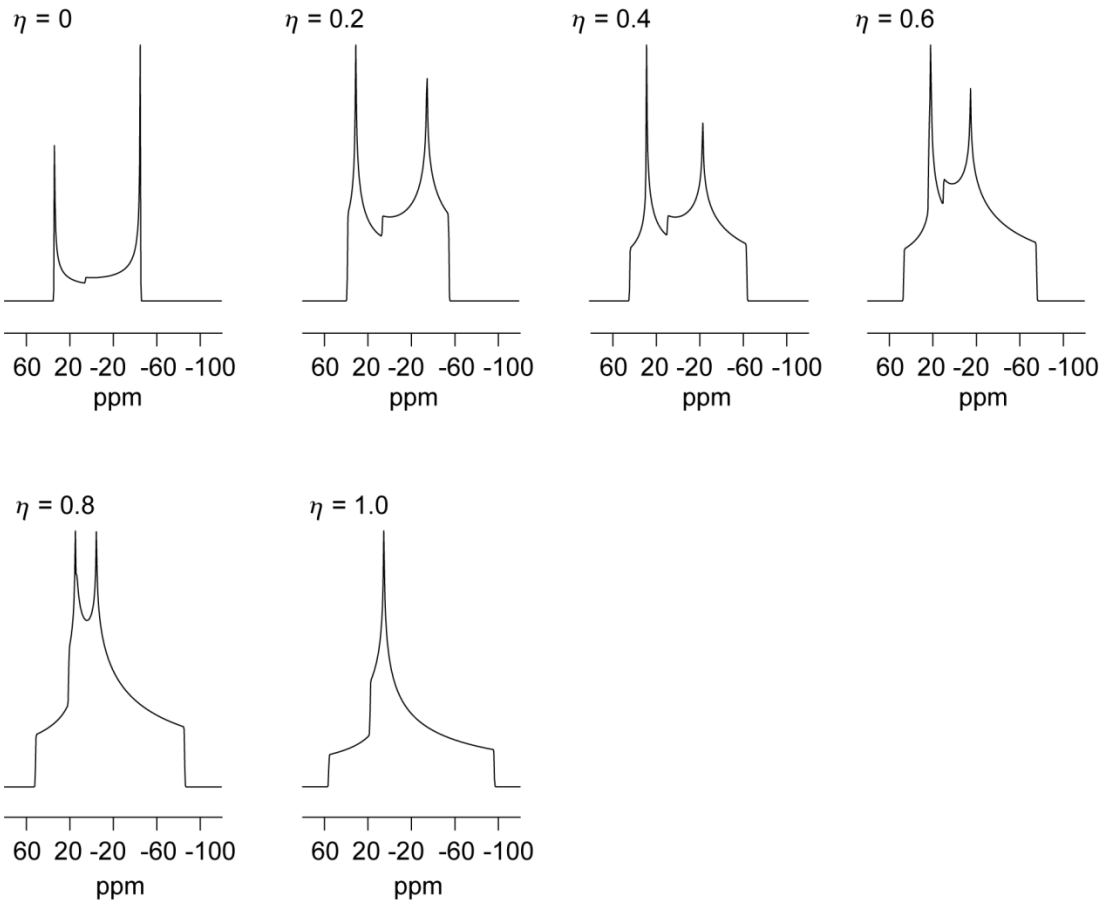

Figure 6 Simulated CT powder spectra of a spin 3/2 nucleus under the influence of second-order quadrupolar coupling (C_Q = 2 MHz, δ_{iso} = 5 ppm) generated using WSolids[9]. The "horns" of the CT move closer together as η increases.

change as η is modified and the "horns" of the CT signal will move closer together as η increases (Figure 6).

Indirect Spin-Spin (J) coupling interaction

For systems with a collection of nuclei, the nuclei can couple to each other through various methods, one of which is known as the *J* coupling interaction. This interaction is mediated by the bonding electrons and can result in a splitting in the resonance frequencies if the energies of the spin states are perturbed to different extents (Figure 7).

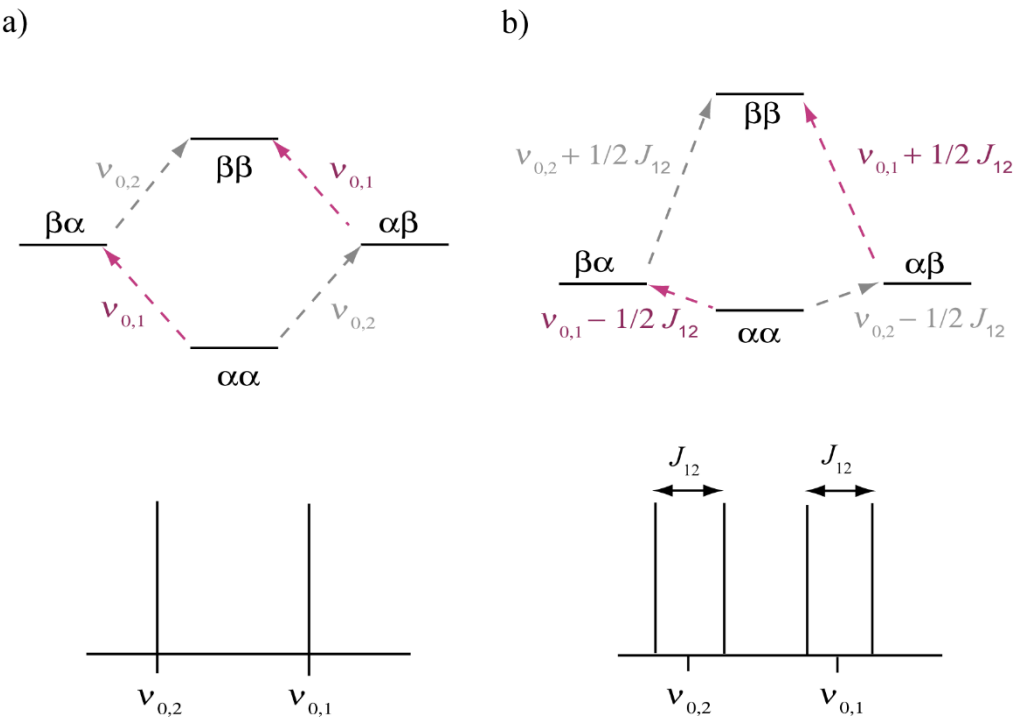

Figure 7 Energy level diagram (top) and the corresponding schematic spectrum (bottom) for a system with two magnetically inequivalent spins (I = 1/2) in the absence of J coupling (a) and in the presence of J coupling (b).

The corresponding Hamiltonian, $\hat{H}_{\mathrm{J}}$, for spin i due to coupling with spin k is[2]

$$\hat{H}_{\mathrm{J}} = 2\pi \hat{I}_{\mathrm{i}} \cdot \boldsymbol{J}_{\mathrm{ik}} \cdot \hat{I}_{\mathrm{k}} \qquad 23$$

where $\boldsymbol{J}_{\mathrm{ik}}$ is the second-rank J coupling tensor. Similar to the nuclear magnetic shielding interaction, the J coupling Hamiltonian consists of a non-zero isotropic (J_{iso}) and anisotropic (ΔJ) component. In solution, rapid molecular tumbling averages out the anisotropic contribution, and the isotropic component gives rise to the resonance splitting that is well known in solution phase NMR. In solid state, the anisotropic portion is preserved; nevertheless, it is difficult to measure since it is often small and also inseparable from dipolar coupling interaction.

There are five different contributions to *J* coupling: Fermi-contact coupling (FC), diamagnetic spin-orbital coupling (DSO), paramagnetic spin-orbital coupling (PSO), spin-dipolar coupling (SD) mechanisms, and the Fermi-contact coupling spin-dipolar coupling cross-term (FC/SD).[10-12] The FC mechanism represents the interaction between the nucleus and the electron at the site of the nucleus. Consequently, it is only non-zero if the orbitals consist of s-character. The DSO and PSO mechanisms account for the interaction between the nuclear spin angular momentum and the orbital angular momenta of the electrons; while SD is a result of the interaction between the nuclear and the electron spin angular momenta. These four mechanisms give rise to J_{iso}, while the last interaction, FD/SD, contributes only to ΔJ.[13] The *J* coupling interaction is commonly decomposed into these five components for analysis; however, experimentally, these five contributions cannot be separated and a sum of these interactions is observed.

1.1.3 Crystal Symmetry and Disorder

The fundamental difference between SSNMR and solution phase NMR is the time scale of the molecular motions. In solution, molecules are, in general, tumbling rapidly and isotropically, therefore the anisotropic interactions are averaged to their isotropic values. In SSNMR, the motions of the molecules are more restricted, and as described in the previous subsection, the anisotropic components are observed in the corresponding spectra. Besides the appearance of the anisotropic interactions, the lack of rapid isotropic tumbling in SSNMR can also lead to differences in the number of chemically and/or magnetically equivalent spins as compared to solution phase NMR. In general, two or more spins are defined as chemically equivalent if they experience the same chemical

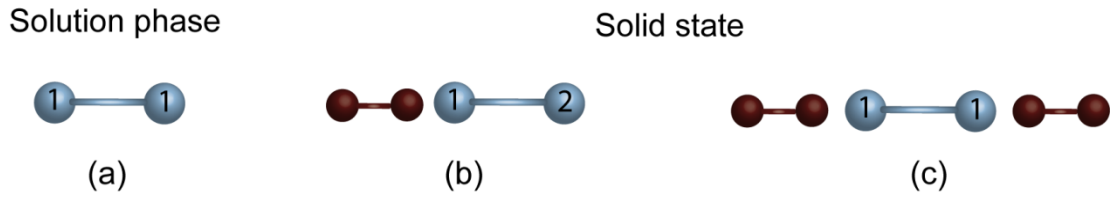

Figure 8 Schematic illustrating the chemical equivalence for a pair of spins (the blue spheres) in solution (a) and in the solid state (b and c). Spins that are chemically equivalent in the solution phase (a) can be inequivalent in the solid state due to a loss in crystallographic symmetry (b). For (a) and (c) one resonance will be observed for the two spins, for (b) two resonances will be observed.

shielding effects and therefore have the same chemical shifts. Since molecules are tumbling rapidly and isotropically in solution, chemical equivalence can therefore be determined based on the symmetry of an isolated molecule and nuclei are said to be equivalent if they are related by molecular symmetry. For instance, the three protons in fluoromethane are chemically equivalent in solution since they are related by an axis of symmetry. However, in SSNMR, the lack of isotropic tumbling means that the effects of the surrounding molecules must also be taken into consideration.[4] Therefore, spins that were considered to be chemically equivalent in solution might lose their equivalence in the solid state due to a loss in symmetry in the crystalline state (Figure 8).

Besides chemical equivalence, the lack of rapid isotropic motion in the solid state also results in differences in how magnetic equivalence is defined. In general, two or more spins are said to be magnetically equivalent if they have chemical and coupling equivalence.[14] This means that in solution, spins are magnetically equivalent if they are related by molecular symmetry and have the same *J* coupling constant to any other spins in the molecule. For example, the protons in fluoromethane are magnetically equivalent since they are chemically equivalent and have the same coupling to the other spins.

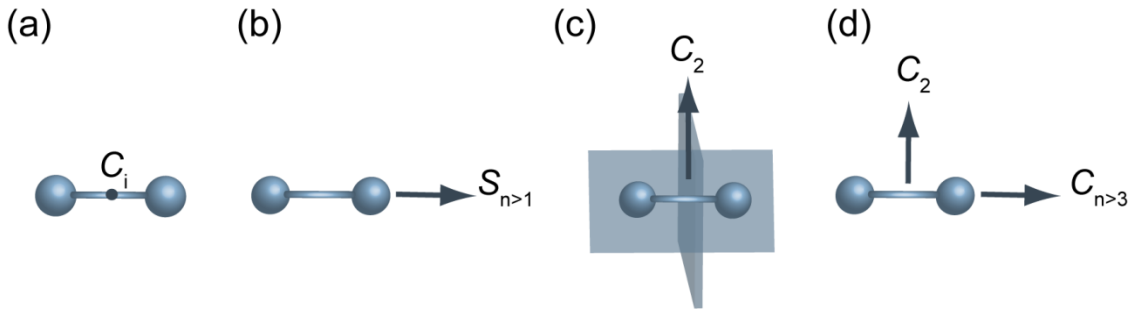

Figure 9 Schematic illustrating the symmetry operations (i.e. (a) C_i, (b) $S_{n>1}$, (c) C_2 and a mirror plane, or (d) $C_{n>3}$ along the bond and C_2 relating the spins) which are required to be present in the crystal structure for two spins to be considered magnetically equivalent in the solid state.

However, the protons of 1,1-difluoroethylene would be chemically equivalent but magnetically inequivalent since the two protons would couple to a given fluorine differently (i.e. proton A would have a coupling constants of $J_{cis}(H_A, F)$, while proton B would have a coupling constant of $J_{trans}(H_B, F)$).[15] On the other hand, for a pair of spin to be considered magnetically equivalent in the solid state, not only do they need to have the same tensor magnitude, they also need possess the same tensor orientations. Practically, this means that for a perfectly static solid, a pair of spins are magnetically equivalent if they are crystallographically related by C_i, $S_{n>1}$, C_2 and a mirror plane, or consist of a $C_{n>3}$ axis along the bond and a C_2 axis relating the nuclei in the corresponding crystal structure (Figure 9).[16] Consequently, it is the crystal structure instead of the molecular structure that needs to be considered when predicting the appearance of the SSNMR spectrum, and a pair of crystallographically inequivalent spins will give rise to two distinct SSNMR spectra given that the solid does not consist of any molecular motion.

Many solids are not perfectly crystalline and therefore display crystallographic disorder. One type of disorder, known as dynamic disorder, can complicate the analysis

of SSNMR spectra. Dynamic disorder is a temporal disorder, where the positions of the disordered atoms change as a function of time.[4] Accordingly, it can alter the appearance of the SSNMR spectra as it introduces molecular motion into the system, and its influence on the spectra depends on the rate of the motion on the NMR timescale, which is defined as the chemical shift differences (in frequency units) between the resonances corresponding to the distinct spins.[4,17] If the motion is static on the NMR timescale (i.e. the rate of motion is significantly smaller than the chemical shift differences), then a resonance corresponding to each inequivalent spin will be observed. On the other hand, if the motion is rapid on the NMR timescale (i.e. the rate of motion is comparable and/or larger than the chemical shift differences), apparent equivalence will emerge and an averaged spectrum would be recorded. Therefore, for spins in crystallographically inequivalent sites, the number of NMR signals observed can be reduced if rapid molecular motion is present. For example, if we consider two crystallographically inequivalent spins in the absence of any detectable molecular motion and only under the influence of the Zeeman and the isotropic magnetic shielding interaction, two distinct resonances will be obtained in the corresponding SSNMR spectrum (Figure 10). As the molecular motion is introduced into the system such that the two spins undergo exchange, the two peaks will begin to broaden. When the motion is fast on the NMR timescale, a single magnetic environment will be detected and an averaged spectrum with a single resonance will be obtained (Figure 10).

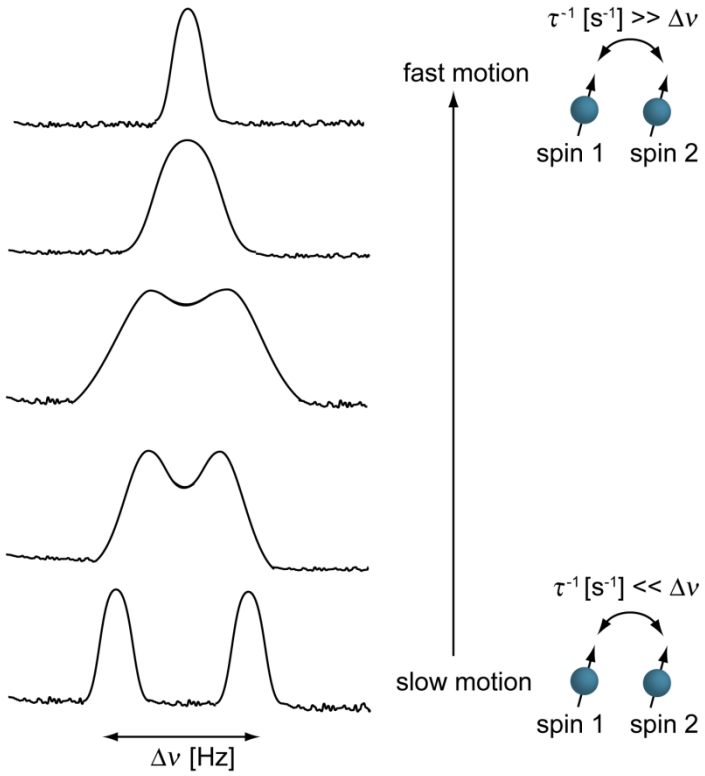

Figure 10 Schematic representation illustrating the resulting SSNMR spectra for a system with two crystallographically inequivalent spins experiencing exchange under the influence of the Zeeman interaction and the isotropic nuclear magnetic shielding interaction. Two resonances are observed when the rate of motion (τ^{-1}) is slow on the NMR timescale ($\tau^{-1} << \Delta\nu$); however, when the motion is fast on the NMR timescale ($\tau^{-1} >> \Delta\nu$), a single resonance is observed.

The example above describes the influence of motions on the isotropic chemical shifts of two spins. However, since numerous spins are present in a powder sample, a powder pattern will be observed. As discussed earlier, the powder pattern results from the presence of different molecular orientation with respect to B_0, with each orientation giving rise to a distinct resonance. As such, changes in orientation as induced by molecular motion would result in a change in the resonance frequencies.[5] If the motional rate is similar to the width of the powder pattern, distortions in the powder pattern will appear and the degree of distortion depends on the rate and the type of motions (Figure 11). Once

motional rate is significantly greater than the width of the powder pattern, the fast motion limit is reached, and the powder pattern will be reduced due to motional averaging of the tensors (Figure 11). For example, in the simple case of fast reorientation around a single axis, the magnitude of the chemical shift anisotropies for the tensors which are effected by motion will be scaled by $\frac{3\cos^2\theta-1}{2}$, where θ is the angle between the z principal axis of the tensor and the axis of rotation (Figure 11).[5] Since the degree of distortion depends on the type of motion and its corresponding rate, information on the dynamics can be obtained by simulating the experimental powder pattern.

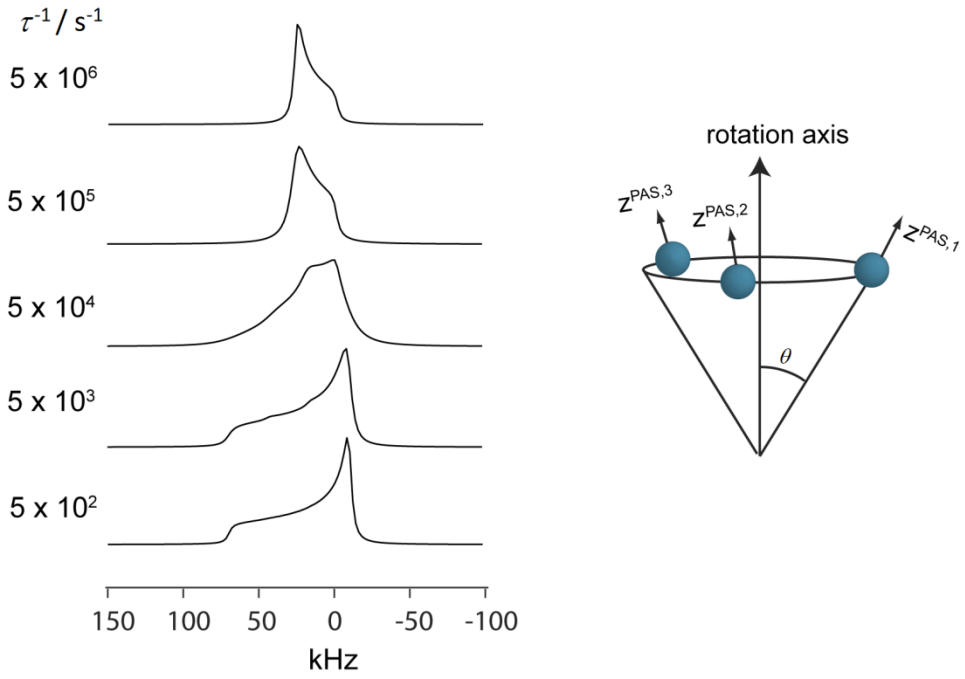

Figure 11 Simulated chemical shift anisotropy line shapes (left) for a spin 1/2 nuclei undergoing three-site hopping about a rotation axis oriented at θ = 71° with respect to the z principal axis of the chemical shift tensor (right). Distortion in the powder pattern is observed when the rate of the motion, τ^{-1}, is similar to the width of the powder pattern ($\tau^{-1} \approx 5 \times 10^3$ s^{-1}). At the fast motion limit ($\tau^{-1} \approx 5 \times 10^6$ s^{-1}), the width of the powder pattern is reduced by a factor of 0.36 due to motional averaging. The spectra were simulated using EXPRESS[18], with δ_{iso}, Ω and κ set as 131 ppm, 800 ppm and -1, respectively.

1.2 Basic Components of an NMR Experiment

1.2.1 One Dimensional (1D) NMR Experiments

As mentioned in section 1.1.1, NMR active nuclei have a non-zero spin (i.e. $I > 0$) and therefore a non-zero magnetic moment (i.e. $\mu \neq 0$). When NMR active nuclei are placed in an external static magnetic field (i.e. in a NMR spectrometer), μ will interact with the field through the Zeeman interaction, resulting in non-degenerate energy states. This interaction can also be depicted using the vector model, which is often employed to explain the key concepts behind NMR experiments. In this model, μ is represented by a vector ($\vec{\mu}$) and the interaction between μ and the field is described as a precession of $\vec{\mu}$ around the external magnetic field vector, $\vec{B}_0$, at a frequency of υ_0 (Figure 12). For a system with a collection of nuclei (i.e. in a realistic sample), there will be a random distribution in the orientation of $\vec{\mu}$, each precessing around $\vec{B}_0$ (Figure 13a).[2] After a time period of T_1, a majority of the magnetic moments will align with the external magnetic field such that a net magnetic moment which points parallel to the external magnetic field is created (Figure 13b). In NMR experiments, signals are generated by the precession of the net transverse magnetization, created using the net magnetic moment, around $\vec{B}_0$. This is accomplished by applying a radiofrequency (RF) pulse such that an oscillating magnetic field (B_1) is generated,[3] which would result in the precession of the individual magnetic moments, and therefore the net magnetic moment, around the RF magnetic field vector, $\vec{B}_1$ (Figure 13c).[2] Using this precession, a transverse magnetization is formed by rotating the net magnetic moment from the z-axis by 90° (Figure 13d). Once this net transverse magnetization is produced, the B_1 field is

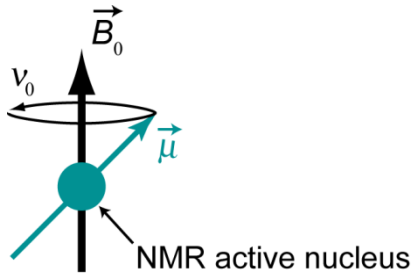

Figure 12 Precession of $\vec{\mu}$ of a NMR active nucleus under the influence of an external static magnetic field as illustrated using the vector model.

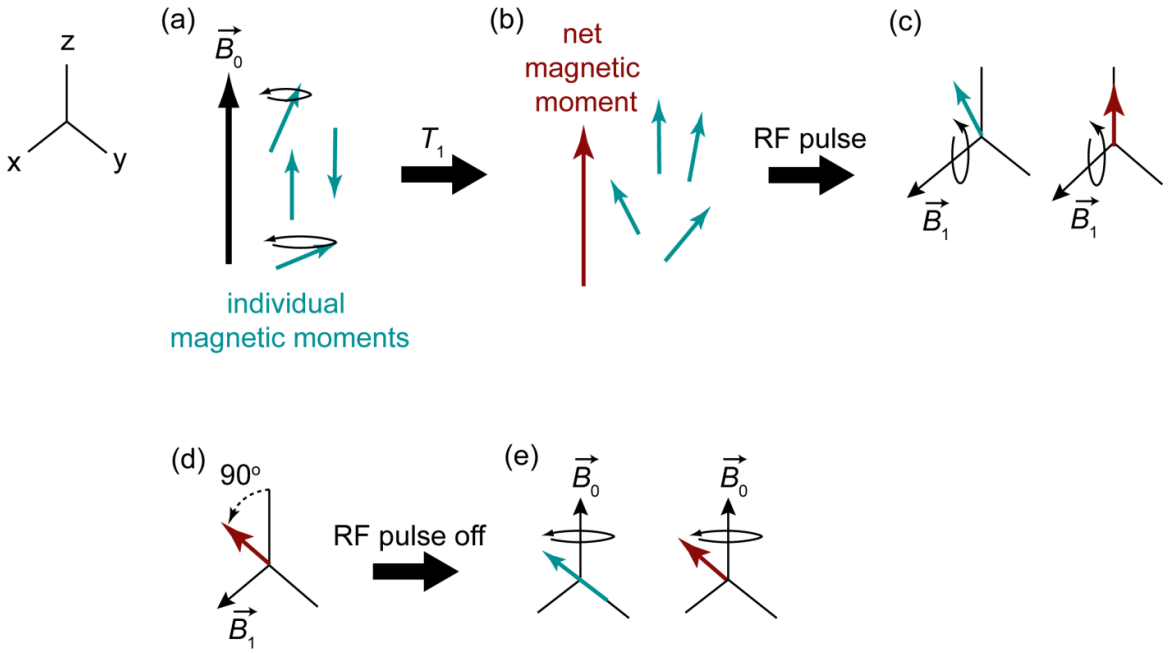

Figure 13 Vector model representation for the generation of a precessing transverse magnetization in a NMR experiment.

then turned off, causing in the individual magnetic moments to precess around $\vec{B}_0$. Since the individual magnetic moments are now precessing around $\vec{B}_0$, the net magnetic moment will do so as well (Figure 13e); consequently, a precession around $\vec{B}_0$ by the net transverse magnetization is

created, which is then detected and Fourier transformed in order to give the corresponding spectrum.

The x- and y- components of the net transverse magnetization, M_x and M_y, take the form of

$$M_x(t) = M_0 \cos(\Omega t) \exp\left(-\frac{t}{T_2}\right) \quad 24$$

$$M_y(t) = M_0 \sin(\Omega t) \exp(-\frac{t}{T_2}) \quad 25$$

, where M_0 is the magnitude of the net magnetic moment vector, T_2 is the time constant which accounts for the decay of the transverse magnetization and Ω is the apparent Larmor precession frequency of the net magnetic moment.[3] The exponential terms in equations 24 and 25 account for the decay of the signal as a function of time. Initially (i.e. at $t = 0$), the precession of the individual magnetic moments are synchronized due to the coherence generated by the RF pulse (Figure 14).[2] However, as time progresses, dephasing will occur due to variations in the local magnetic fields (Figure 14). Since the generation of a net magnetic moment requires the presence of a preferential phase, the loss in coherence thus results in a decrease in the magnitude of the net transverse magnetization. Consequently, the net transverse magnetization generated by the RF pulse, and therefore the NMR signal, will be destroyed as time progresses.

The series of manipulations performed on the spins are commonly expressed schematically as a function of time via pulse sequences. Figure 15 depicts the pulse sequence for a simple one-pulse experiment, in which a RF pulse is applied and the signal is recorded immediately

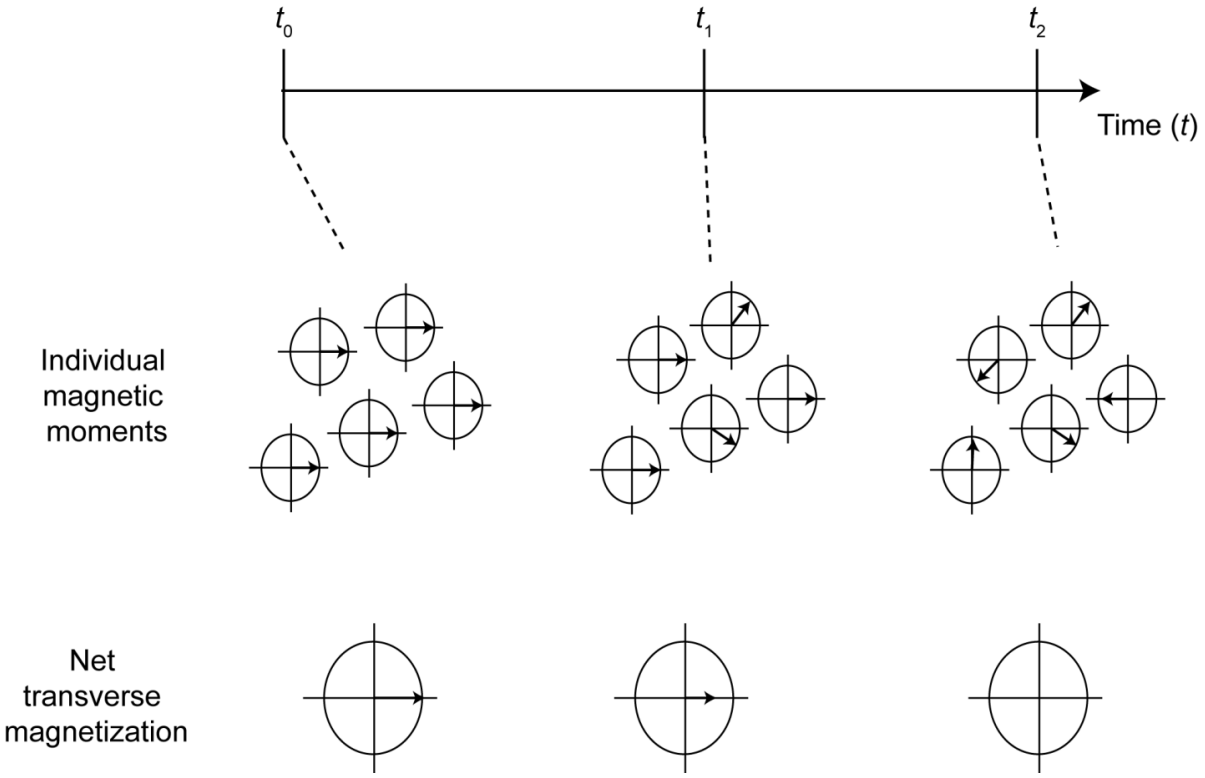

Figure 14 Schematic representation for how the spin coherence generated by the RF pulse (at t_0) is destroyed as a function of time, resulting in a decrease in the magnitude of the net transverse magnetization (at t_1) and eventually, the loss of the magnetization (at t_2). t_0 represents the time immediately after the RF pulse (i.e. $t = 0$), and the magnetic moments are projected onto the xy plane.

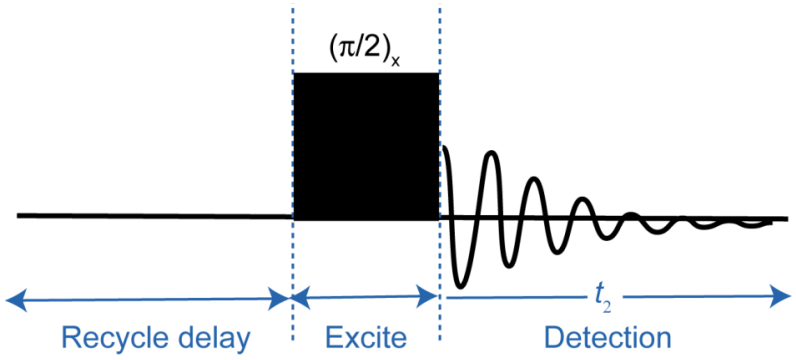

Figure 15 Pulse sequence for a simple one-pulse experiment.

after. The time period before the application of the first pulse is known as the recycle delay. This delay is governed by the time required to generate a net magnetic moment along the z-axis (i.e. T_1), and it dictates how frequent a spectrum can be recorded in a given period of time. Furthermore, each RF pulse is represented by a black box, where the angle of rotation of the net magnetization vector is often expressed above the box as radians (e.g. $(\pi/2)_x$ pulse denotes a rotation of 90^o from the initial axis with x-axis as the axis of rotation). Often, more complicated pulse sequences are employed in NMR in order to achieve various objectives, and the pulse sequences which are commonly employed in SSNMR are discussed in section 2.1.

1.2.2 Two Dimensional (2D) NMR Experiments

In one dimensional (1D) NMR experiments, the spins are first excited by RF pulse(s) and the signals are immediately recorded as a function of the detection time (i.e. time t_2 in Figure 15); accordingly, the spectrum consist of one frequency dimension (the direct dimension) after Fourier transform (FT). For a two dimensional (2D) NMR experiment (Figure 16), the signal is allowed to evolve for an additional (variable) time period (t_1) before detection; therefore, the signal depends on two time variables (t_1 and t_2), resulting in a NMR spectrum with two frequency dimensions (the indirect dimension given by t_1 and the direct dimension given by t_2). Specifically, a 2D NMR spectrum is generated by acquiring a series of 1D spectra, where the t_1 time is increased incrementally in each experiment, then by performing a double FT on the dataset (Figure 17).[3] For example, the first spectrum would be recorded with $t_1 = 0$, then detected during t_2. The next spectrum is then measured with $t_1 = x$, and third spectrum is acquired with $t_1 = 2x$, and so forth, until sufficient data is obtained for the indirect dimension (Figure 17a). The resulting 1D

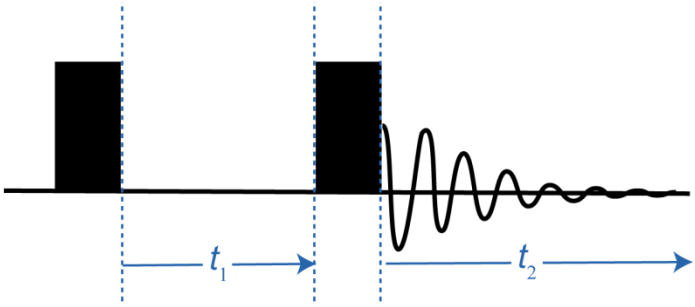

Figure 16 The general scheme for a 2D NMR experiment. The signal is allowed to evolve for two time periods, t_1 and t_2, resulting in a spectrum which consists of two frequency dimensions after FT.

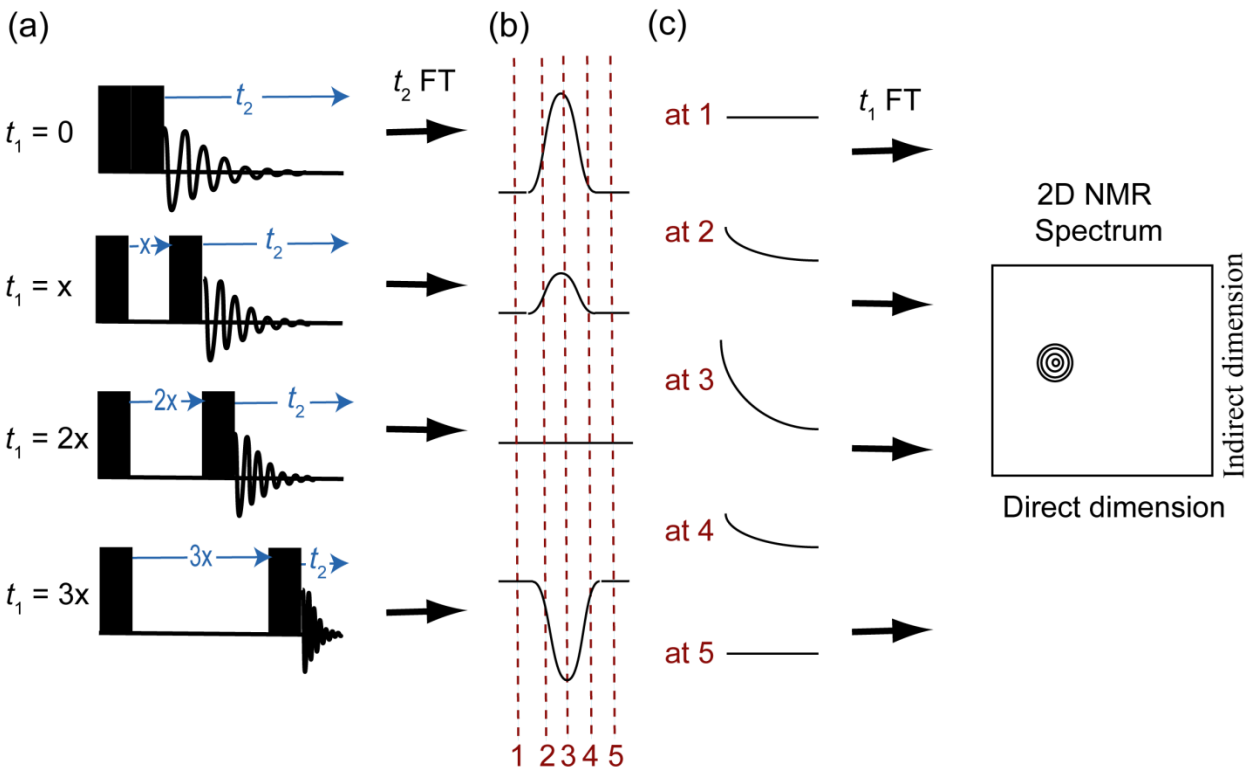

Figure 17 Schematic depiction on how a 2D NMR experiment is performed and processed. A series of 1D spectra with incremented t_1 is first recorded (a) and the data is then FT with respect to t_2 (b). Plots with intensity vs. t_1 are then constructed from the spectra obtained in (b), and a second FT is performed in order to obtain the 2D spectrum (c).

spectra are then FT with respect to t_2 (similar to regular 1D experiments), giving rise to signals with intensities which are modulated as a function t_1 (Figure 17b). The intensities at each point of the spectrum are then plotted as a function of t_1 (Figure 17c), therefore giving rise to series of t_1-dependent data, which are then FT again, resulting in the 2D NMR spectrum.

1.4 DQF *J*-resolved SSNMR Spectroscopy

The *J* coupling interaction is commonly employed for probing the nature of chemical bonding as it originates from electronic orbital overlap. For example, conformational and structural insights into organic and biological systems are often obtained via the homonuclear and heteronuclear *J* couplings involving spin 1/2 nuclei.[19-23] However, the *J* coupling for a pair of quadrupolar nuclei is less utilized in comparison since the corresponding spectral fine structures are more difficult to detect. In solution, rapid quadrupolar relaxation makes the measurement of *J* coupling for a pair of quadrupolar nuclei rarely feasible, while in the solid state, the small *J* splittings are often unobservable due to anisotropic quadrupolar line broadening. Various methods can be employed for obtaining homonuclear quadrupolar *J* coupling constants in the solid state;[24-31] however, these methods often require additional probe hardware and/or relatively tedious data analysis procedures. Recently, our lab has developed a series of easily implantable 2D SSNMR experiments for measuring the *J* coupling constants for pairs of homonuclear quadrupolar nuclei, one of which is the double-quantum-filtered (DQF) *J*-resolved SSNMR pulse sequence (Figure 18).[27] The DQF *J*-resolved sequence employs CT-selective pulses and is based off of the regular 2D homonuclear *J*-resolved sequence which consists of a simple Hahn echo

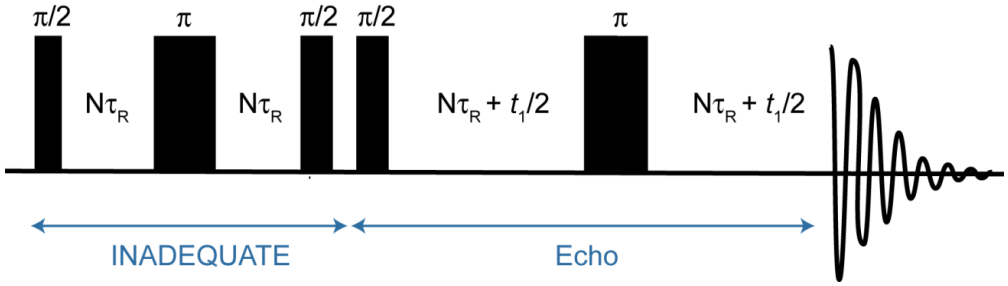

Figure 18 Pulse sequence for DQF *J*-resolved SSNMR experiment.

(Figure 19a)[32]. The Hahn echo refocuses the chemical shift, heteronuclear coupling, and quadrupolar coupling interactions, thereby removing the corresponding effects from the indirect dimension of the spectrum (see section 2.1.3 for a more detailed discussion on the Hahn echo). However, the homonuclear *J* coupling will continue to evolve under the Hahn echo as the π pulse will act on both of the coupled spins, therefore the corresponding information is preserved in the indirect dimension. Consequently, the effects of chemical shift, heteronuclear coupling and quadrupolar coupling interactions are separated from the *J* coupling interaction. This can allow for the *J* coupling constants to be measured more easily and precisely as compared to extracting from a simple 1D spectrum since complications which result from the other NMR interactions (e.g. peak broadening and peak overlap) are now removed. For example, for spin 1/2 nuclei that are only under the influence of isotropic chemical shift and *J* coupling interactions, peak overlap due to similar chemical shifts can obscure the extraction of the *J* coupling constants (Figure 19b). However, this can be avoided by the use of the 2D homonuclear *J*-resolved experiments as the *J* coupling interaction is observed as a simple doublet in the indirect dimension and the separation between the doublet gives the magnitude of the *J* coupling constant (Figure 19c).

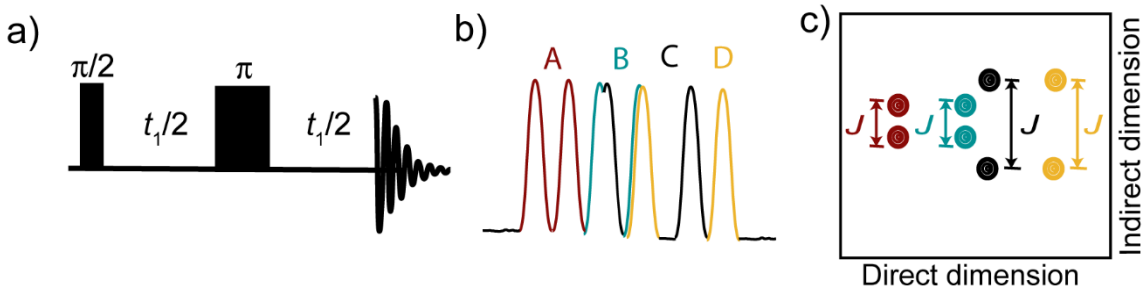

Figure 19 (a) Pulse sequence for a regular 2D homonuclear *J*-resolved experiment, which is just a simple Hahn Echo. (b) Schematic depiction of a theoretical 1D spectrum for a 4 spin system (A, B, C, and D; $I_A = I_B = I_C = I_D = 1/2$) that is under the influence of isotropic chemical shift and *J* coupling interactions. The extraction of the corresponding *J* coupling constants can be difficult due to peak overlap. (c) Schematic depiction of the 2D homonuclear *J*-resolved spectrum for the spin system in (b), illustrating that these experiments can be helpful for extracting the *J* coupling constants in cases where spectral crowding is an issue. The spectra in (b) and (c) are color coded to the corresponding spin.

For a pair of quadrupolar nuclei in the solid state, the homonuclear *J*-resolved experiments will remove the influence of anisotropic quadrupolar line broadening from the indirect dimension, resulting in a more observable and easily measurable *J* coupling interaction. Nevertheless, only spin systems where both spins are in the central state (i.e. $m_I = 1/2$ and $m_S = 1/2$) will be *J* modulated, whereas the transitions involving other spin states (e.g. $m_I = 1/2$ and $m_S = 3/2$) will be refocused, thereby creating a large zero frequency signal in the indirect dimension (Figure 20a). This zero frequency signal can mask the fine *J* splittings, therefore obscuring the extraction of the *J* coupling constants. As such, in the DQF *J*-resolved experiment, an INADEQUATE block is executed before the Hahn echo as a double-quantum filter (Figure 18). In INADEQUATE, only signals that can support double quantum transition ($\Delta M = 2$) can pass through, while other signals are filtered out; consequently, the large zero frequency signal is removed since only spin systems where both spins are in the central state would survive the

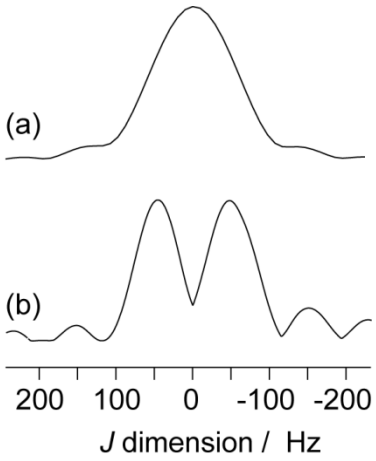

Figure 20 The indirect dimension of (a) a regular ^{11}B homonuclear *J*-resolved spectrum, which consists of a large signal at zero frequency, and (b) a ^{11}B DQF *J*-resolved spectrum, in which the zero frequency signal is suppressed via the use of INADEQUATE. The spectra were acquired on $K_2[B_2(CN)_6]$ at 9.4 T with a spinning speed of 12 kHz.

double-quantum filtering. As a result, the DQF *J*-resolved SSNMR spectrum will consist of a simple doublet in the indirect dimension for each bond (Figure 20b), where the magnitude of the *J* splitting is related to both the *J* coupling constant and the magnetic equivalency of the spin pair.[27,29,30,33] For a pair of magnetically inequivalent nuclei, the *J* splitting will equal to *J* (Figure 21b). On the other hand, for a pair of magnetically equivalent nuclei, the *J* splitting will be amplified by a factor of $(2I+3)(2I-1)/4$ (e.g. for a pair ^{11}B nuclei, the splitting will be 3*J* since $I = 3/2$) (Figure 21a).

As discussed in section 1.1.3, magnetic equivalency in the solid state is closely associated with crystallographic equivalency. For a pair of nuclei in a solid which does not exhibit significant molecular motions, the nuclei are considered to be magnetically equivalent if they are related by C_i, $S_{n>1}$, C_2 and a mirror plane, or consist of a $C_{n>3}$ axis along the bond and a C_2 axis relating the nuclei in the corresponding crystal structure (Figure 9);[16] therefore, not only can DQF

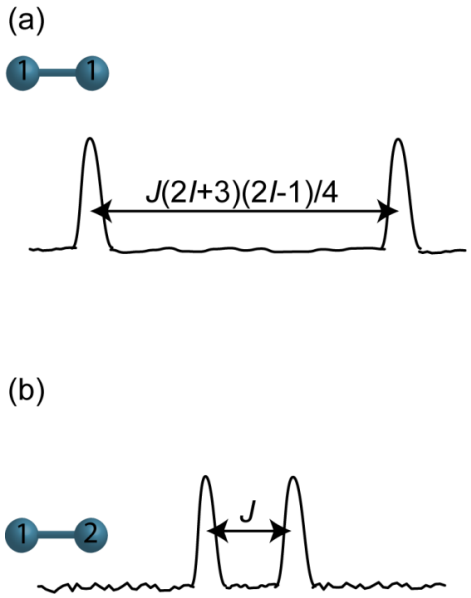

Figure 21 Schematic representations of the DQF *J*-resolved spectra for (a) a pair of magnetically equivalent nuclei and (b) a pair of magnetically inequivalent nuclei.

J-resolved SSNMR experiments provide *J* coupling information, it can also provide crystallographic information on the system.[27,29,30] Moreover, apparent magnetic equivalence can also result due to the presence of molecular motion. This can be easily understood by considering the magnetic equivalence observed in solution phase NMR between the three protons on a methyl group as a result of rapid rotation about the C_3 axis. This then suggests that dynamics can potentially induce amplified *J* splitting for a pair of crystallographically inequivalent nuclei. Consequently, the presence of dynamics could confound the extract of *J* coupling constants, and more importantly, DQF *J*-resolved SSNMR experiments can potentially be employed as a novel tool to detect molecular motions. However, this has yet to be explored as previous studies were conducted on static systems.

1.5 Hexacyanodiborane(6) Dianion Salts and Diboratellurenium Compounds

Diboron compounds consist of a wide range of applications in chemistry. For example, they are commonly employed in reduction, borylation and polymerization reactions,[17,34,35] as well as for the construction of various natural products, pharmaceutical compounds and biologically active compounds.[36] The electronic characterization of these compounds is of significant importance since it would provide a better understanding on their chemical versatility, thereby promoting the synthesis of novel diboron reagents and the development of potential applications. Previous investigations have shown the $J(^{11}B, ^{11}B)$ coupling constants for diboron compounds measured using ^{11}B DQF *J*-resolved SSNMR spectroscopy can be employed to investigate the corresponding electronic features as the coupling constants were observed to strongly correlate to the p-orbital hybridization state of the boron orbitals which form the B-B bond, as well as the strength of the B-B bond.[29,30] This then indicates the possibility of directly extracting electronic information from the measured $J(^{11}B, ^{11}B)$ coupling constants without the need of computations if enough empirical data is obtained. However, these studies were only conducted on compounds with B-B bonds formed from sp^1 to sp^2 hybridized boron orbitals (e.g. $B(sp^2)$-$B(sp^2)$), and none has been performed on compounds with electron-precise two-center-two-electron (2c-2e) $B(sp^3)$-$B(sp^3)$ bonds. Moreover, SSNMR studies relating the $J(^{11}B, ^{11}B)$ coupling constants of heterocyclic boron compounds to the corresponding electronic structures have also yet to be conducted.

Recently, the synthesis of hexacyanodiborane(6) dianion ($[B_2(CN)_6]^{2-}$) salts which encompass 2c-2e $B(sp^3)$-$B(sp^3)$ bonds[37] (Figure 22) and diboratellurenium salts which consists of

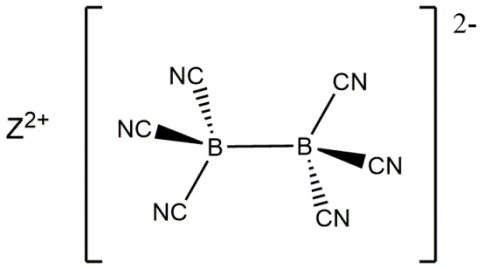

Figure 22 Structures of the $[B_2(CN)_6]^{2-}$ salts investigated in this study, where Z = $Mg(DMF)_6$ (**1**), $Cu(DMSO)_6$ (**2**), K_2 (**3**), $[nBu_4N]_2$ (**4**), or $[BMPL]_2$ (**5**).

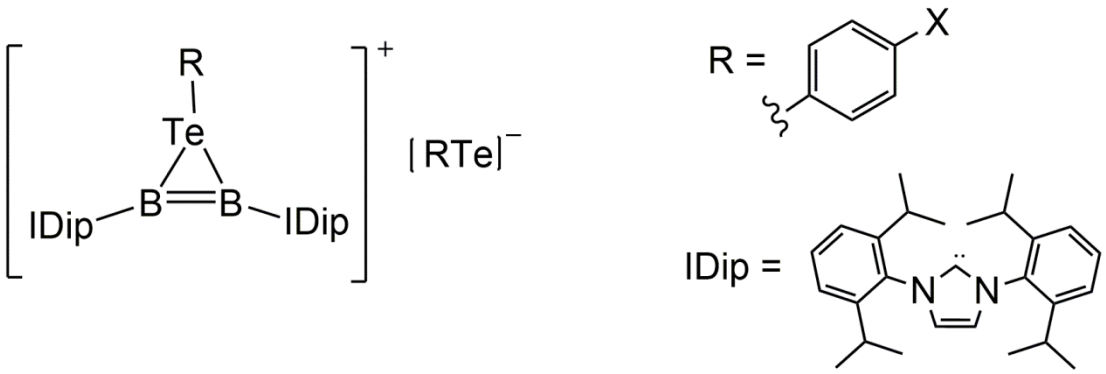

Figure 23 Structures of the diboratellurenium salts investigated in this study, where X = H (**6**) and F (**7**).

B-B bonds that are topped with a bridging Te (Figure 23) have been reported[38]. These compounds serve as excellent models for expanding the previously developed relationship between $J(^{11}B, ^{11}B)$ coupling constants and electronic properties as they consist of electron-precise B-B bonds and boron heterocycles, respectively. For the diboratellurenium cations, it was also found from X-ray diffraction and Raman spectroscopy that the bridging Te decreases the bond order of the B-B bond.[38] However, it was unclear if the bonding structures of these systems are more similar to oxiranes or if they follow the Dewar-Chatt-Duncanson bonding model. Since $J(^{11}B, ^{11}B)$

coupling constants have been shown to strongly correlate to the hybridization of the B-B bonds, ^{11}B DQF *J*-resolved SSNMR spectroscopy is then an ideal tool for probing the bonding structures of these cations. Moreover, a range of crystallographic behaviors was observed for the $[B_2(CN)_6]^{2-}$ salts.[37] Some of the salts were found to contain crystallographically equivalent boron pairs, while others were observed to comprise of crystallographically distinct boron pairs. Salts which consist of nonequivalent borons were also found to be disordered via diffraction techniques, and therefore might exhibit dynamics. As such, these salts serve as excellent archetypes for investigating the influence of dynamics on DQF *J*-resolved SSNMR spectra.

1.6 Objectives

The objectives of this thesis are 1) to examine how molecular motions influence the appearance of the corresponding DQF *J*-resolved SSNMR spectra, 2) to develop a relation between $J(^{11}B, ^{11}B)$ coupling constants and electronic properties of the diboron compounds and 3) to determine the bonding structures of the diboratellurenium salts. The effect of molecular motions on the appearance of the corresponding DQF *J*-resolved SSNMR spectra is examined in section 3.1 using various $[B_2(CN)_6]^{2-}$ salts (Figure 22, $[Mg(DMF)_6][B_2(CN)_6]$ (**1**), $[Cu(DMSO)_6][B_2(CN)_6]$ (**2**), $K_2[B_2(CN)_6]$ (**3**), $[n\text{Bu}_4\text{N}]_2[B_2(CN)_6]$ (**4**), and $[\text{BMPL}]_2[B_2(CN)_6]$ (**5**, [BMPL] = 1-butyl-1-methylpyrrolidinium)) as model systems. The presence of dynamics was determined by ^{13}C and ^{11}B SSNMR spectroscopy, and the types of motional processes present were identified from variable-temperature (VT) experiments. The conclusions reached in section 3.1 were then employed to analyze the corresponding ^{11}B DQF *J*-resolved spectra in order to correctly extract the $J(^{11}B,$

^{11}B) coupling constants of **1**-**5**. The $J(^{11}B, ^{11}B)$ coupling constants of the two diboratellurenium salts (**6** and **7**, Figure 23) were also measured and together with the coupling constants obtained for the $[B_2(CN)_6]^{2-}$ salts and the previously studied diboron systems[29,30], a correlation between $J(^{11}B, ^{11}B)$ coupling constants and electronic properties of the diboron systems was developed (section 3.2). Natural bond orbital (NBO) and natural localized molecular orbital (NLMO) analyses were performed in order to determine the electronic origins of the *J* couplings. Lastly, the bonding structures of the diboratellurenium cations were determined on the basis of the relationship obtained between the $J(^{11}B, ^{11}B)$ coupling constants and the hybridization of the B-B bonds (section 3.3).

2 Methods

2.1 Theoretical Aspects of SSNMR Experiments

2.1.1 Magic Angle Spinning (MAS)

Due to the anisotropic components of the NMR interactions and the general lack of rapid isotropic molecular tumbling, peak overlap as a result of substantial line broadening is frequently observed in SSNMR spectra (Figure 24a). In order to obtain high resolution spectra in the solid state, magic angle spinning (MAS) is often performed (Figure 24b). In this technique, artificial motions are introduced on the solid by spinning the sample in a rotor that's at the "magic angle" of 54.74° with respect to the external static magnetic field (Figure 25a). This can average out magnetic shielding and *J* coupling anisotropies, as well as first-order quadrupolar coupling interactions since their contributions to the SSNMR spectra are scaled by $(3\cos^2\theta - 1)$, where θ is the angle between B_0 and the z-axis of the relevant NMR interaction tensor in its PAS.[4] Experimentally, the value of θ cannot be manipulated; however, it can be shown through geometric arguments that for a sample rotating around an axis at a rate of ω_r, the time average value of $(3\cos^2\theta - 1)$, $<3\cos^2\theta - 1>$, can be expressed as:

$$< 3\cos^2\theta - 1 > = \frac{1}{2}(3\cos^2\theta_R - 1)(3\cos^2\beta - 1) \qquad 26$$

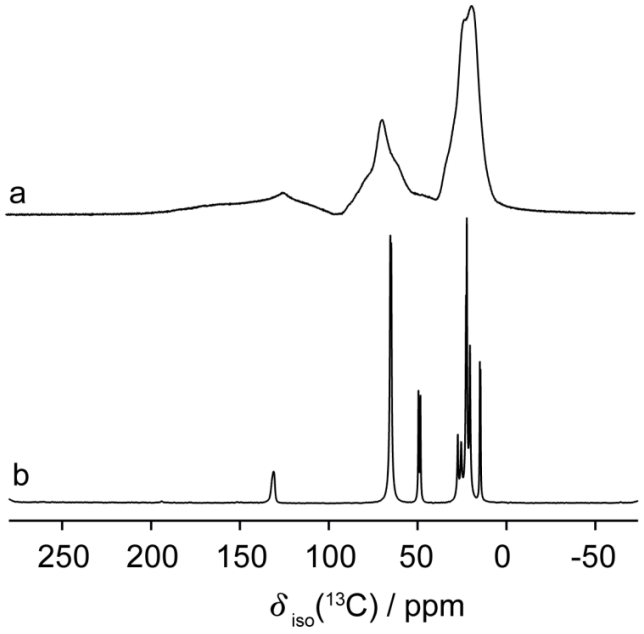

Figure 24 ^{13}C SSNMR powder spectra of $[BMPL]_2[B_2(CN)_6]$ (BMPL = 1-butyl-1-methylpyrrolidinium) recorded with sample under (a) stationary condition and (b) MAS, illustrating that high resolution spectrum can be obtained using MAS.

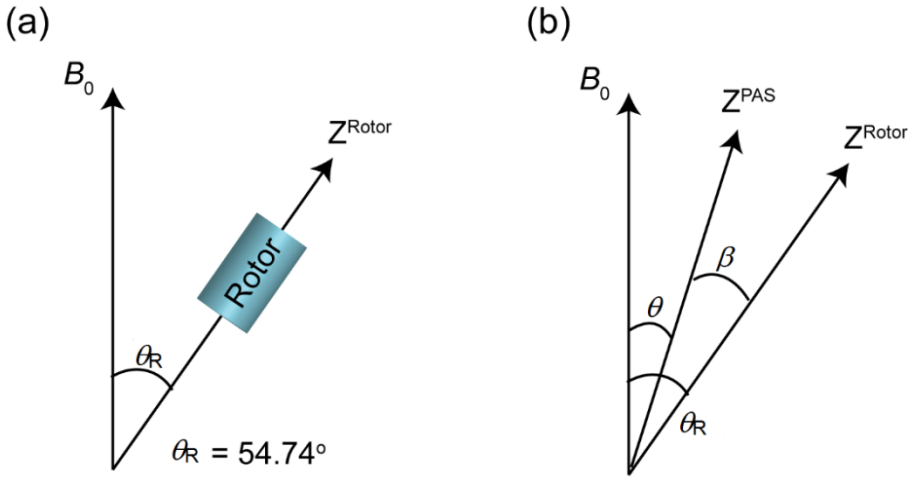

Figure 25 Schematic diagram showing the orientation of the rotor with respect to the external static magnetic field during MAS (a), and the relevant angles θ_R, θ and β for MAS (b, see text).

where θ_R is the angle between B_0 and the z-axis in the rotor frame, and β is the angle between the z-axis of the rotor frame and the z-axis of the NMR interaction in its PAS (Figure 25b).[39] Since $(3\cos^2\theta_R - 1)$, and therefore $<3\cos^2\theta - 1>$, is zero at $\theta_R \approx 54.74^o$, when the sample is spun at an angle of 54.74^o, the anisotropy introduced by magnetic shielding, first-order quadrupolar coupling, and *J* coupling interactions are then removed.

2.1.2 Cross Polarization (CP)

Cross polarization (CP) is a signal enhancement technique commonly employed for the transfer of magnetization from ^{1}H spins to dilute spins (X) with $I = 1/2$ (e.g. ^{13}C), and the NMR spectrum of the dilute spins is then recorded.[4] The ^{1}H → X CP pulse sequence is shown in Figure 26. Transverse magnetization is first created through the application of a π/2 pulse on ^{1}H. Two pulses are then applied simultaneously on the ^{1}H and the X spins, respectively, this period is known as the contact time. During the contact time, magnetization will be transferred from ^{1}H to X if the Hartmann-Hahn match condition, in which the nutation frequencies of ^{1}H and X are equal (i.e. $\gamma^H B_1^H = \gamma^X B_1^X$), is met. Lastly, the NMR signal of X is recorded with high-power proton decoupling.

This technique is essential for SSNMR studies of dilute spins at natural abundance and it consists of two main advantages over the simple direct excitation experiment. Firstly, it allows for a signal enhancement factor of $\frac{\gamma_H}{\gamma_X}$ assuming 100% magnetization transfer.[4] In the case of ^{1}H → ^{13}C CP, this gives a maximum signal enhancement of a factor of 4. Furthermore, since the magnetization originated from the abundant spins, the corresponding recycle delays are then

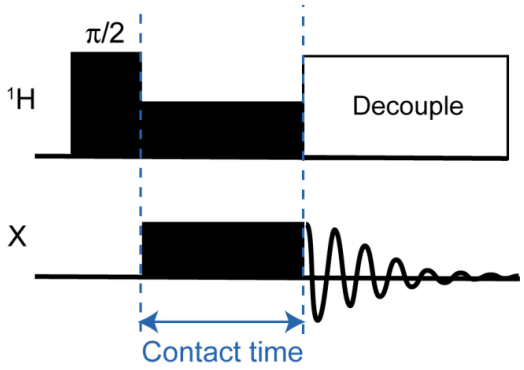

Figure 26 The pulse sequence for $^1H \rightarrow X$ CP, where X is a dilute spin with $I = 1/2$.

governed by the T_1 of the abundant spins instead of the dilute spins. Practically, this can result in a significant decrease in experimental time since in general, $T_{1,H} << T_{1,X}$.

2.1.3 Hahn Echo

The Hahn echo pulse sequence (Figure 27) "refocuses" the effect of chemical shift, heteronuclear coupling and quadrupolar coupling interactions by allowing the transverse magnetization to evolve for a time period of τ under the influence of the relevant NMR interactions, following by an application of a π pulse, then allowing the magnetization to evolve for another period of τ before acquisition.[3,4,40] For example, Figure 27 illustrates the effect of a Hahn echo for a system under the influence of magnetic field inhomogeneity and chemical shifts using vector diagrams. Y-magnetization is first created by the initial $\pi/2$ pulse (Figure 27a), and the spins are then allowed to freely evolve under the influence of chemical shifts for a time period of τ. During τ, dephasing will occur, and at the end of τ, there will be a spread of precession frequencies (Ω_x) with some spins precessing faster than others (Figure 27b). A π pulse is then applied, thereby

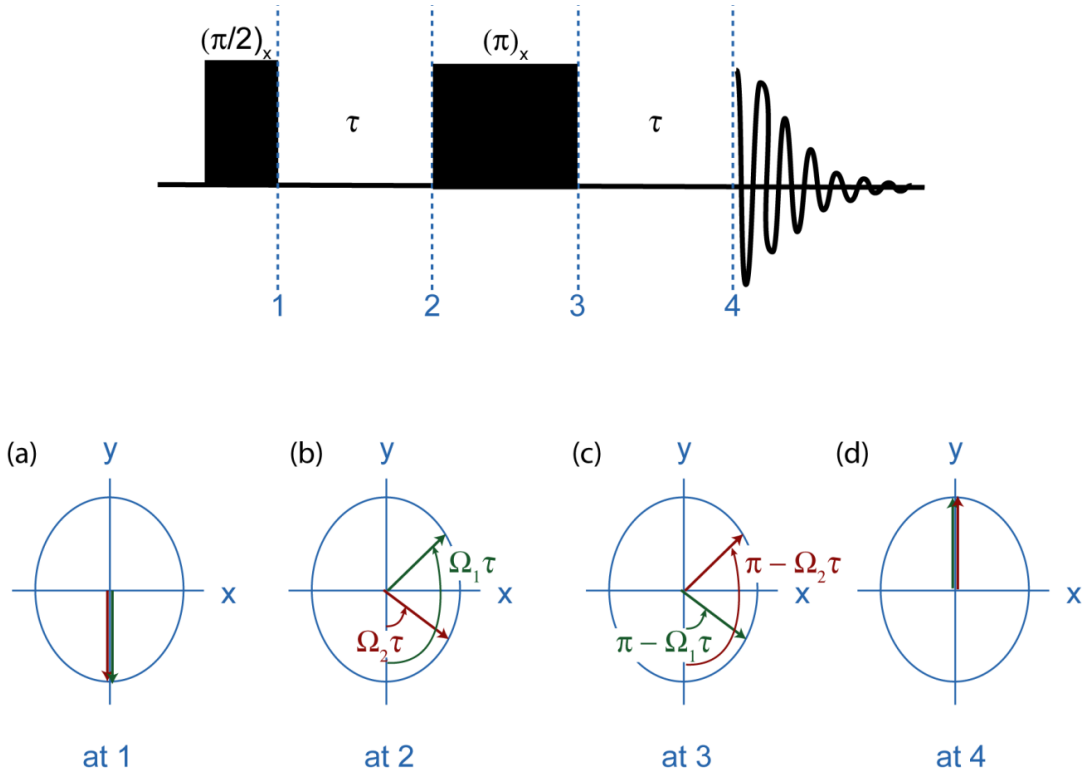

Figure 27 The pulse sequence for a Hahn echo (top) and vector diagrams depicting its effect on spins under the influence of magnetic field inhomogeneity and chemical shift (bottom).

flipping the spins as shown in Figure 27c. Since the precession frequencies and directions of the spins are maintained after the π pulse, evolution of the spins by another period of τ would therefore reverse the effect of the dephasing (Figure 27d). Consequently, the chemical shift is refocused and the influence of the dephasing is removed. This experiment can be used to suppress background signal such as those from the probe and/or rotor cap. Since these parts are outside of the coil, the π pulse in the Hahn echo does not result in a 180° rotation of the corresponding spins, and the effect of dephasing is therefore not entirely removed.

2.2 Theoretical Aspects of SSNMR Calculations

2.2.2 Density Functional Theory (DFT)

Quantum mechanical calculations are regularly employed in conjunction with NMR spectroscopy for the prediction of experimental parameters (e.g. δ_{iso}, C_Q, η, etc.), which can then aid with spectral assignment and interpretation. The calculation of NMR parameters is accomplished by taking the derivative of the electronic energy obtained via solving the Schrödinger equation with respect to the appropriate external parameter.[41] For example, shielding is obtained from the second derivative of the electronic energy with respect to the static external magnetic field and nuclear magnetic moment.[42] Thus, one of the main goals in quantum mechanical calculations is to solve the Schrödinger equation. Nonetheless, for systems with multiple electrons and nuclei, solving for the exact solution to the Schrödinger equation becomes impractical as 1) the corresponding wavefunction consists of 3*N* degree of freedom (i.e. $\psi = \psi(r_1, r_2 \ldots r_N)$, with r being the spatial coordinates of the electron), where *N* is the number of electrons, and 2) the Schrödinger equation becomes a many-body problem since the electron motions are correlated with each other by the electron-electron interactions term in the Hamiltonian ($\sum_{i=1}^{N} \sum_{j<i} U(r_i, r_j)$).[43] Therefore, various types of simplifications have been developed in order to approximate the solution to the Schrödinger equation, one of which is the density functional theory (DFT). DFT is based on the theorems developed by Hohenberg and Kohn,[44] one of which states that the ground state energy of a molecular system is a functional (i.e. function of a function) of the electron density.[41] Therefore, in DFT, the Schrödinger equation is solved by using electron density instead of the wave-

function, which can greatly simplify the calculations as electron density is a function of 3 spatial variables instead of $3N$.[41]

One of the main challenges in DFT is then to obtain the exact electron density function. In modern DFT methods, the Kohn-Sham (KS) approach is employed and the electron density function is acquired by iteratively solving the Kohn-Sham equations. This approach is formally exact; nonetheless, since the exchange correlation (XC) functional must be defined in order to solve these equations and since this functional is unknown except in the case of uniform electron gas, in practice, further approximation is required.[41,43] The simplest approximation for the XC functional is the local density approximation (LDA), which assumes that the exchange correlation energy at a given position is the same as that in a uniform electron gas with the same charge density.[45] An improvement on accuracy can be obtained by the use of the generalized gradient approximation (GGA), which expands on LDA by accounting for electron density gradients. Since electron density gradient information can be incorporated via various methods, a number of GGA functionals have been proposed and one of the more commonly employed functionals for solid-state NMR calculations is the PBE functional developed by Perdew, Burke and Ernzerhof.[46] Furthermore, for NMR calculations involving heavier nuclei, relativistic effects can become important. In these cases, the relativistic effects can be accounted for by the use of zeroth order regular approximation (ZORA) in the corresponding DFT calculation.

2.2.3 Natural Bonding Orbitals (NBOs) and Natural Localized Molecular Orbitals (NLMOs)

Natural bonding orbitals (NBOs) are one- to two- centered orbitals that provide a depiction of the electronic wavefunction that is closely associated with the classical Lewis structure. Further delocalization of the NBOs result in natural localized molecular orbitals (NLMOs), and the corresponding portrayal of the wavefunctions can be considered as a semi-localized representation of the wavefunctions constructed from canonical molecular orbitals (CMOs), such as the Kohn-Sham orbitals used in KS-DFT calculations.[47] Even though NLMOs provide a different interpretation of the electronic wavefunction as compared to those formulated using CMOs, the two are mathematically equivalent.[48,49] Consequently, the physical observables derived using NLMOs are identical to those calculated using CMOs. As such, the additional delocalization effects that are provided by CMOs are removed by the use of NLMOs without any physical penalties and the wavefunctions can be represented in terms of easily interpretable elementary chemical bonding concepts (i.e. Lewis structures).

NLMO/NBO analysis can be employed for the interpretation of various NMR observables, such as *J* coupling constants,[29,30] EFG tensors[50,51] and CS tensors[52]. Such analysis can decompose the NMR interactions into their corresponding electronic contributions, thereby allowing for a greater understanding into the origin of the interactions and the electronic structure of the compounds. For instance, NLMO/NBO analysis of the *J* coupling constants can separate the interaction into its corresponding orbital contributions (e.g. bonding orbitals, core orbitals, etc.), and this information can then be employed to elucidate the relationship between the experimental

J coupling constants and the structural and electronic features (e.g. bond strength and bond order) of the analytes.[29,30]

2.3 Experimental Procedures

2.3.1 ^{13}C SSNMR Spectroscopy

^{1}H → ^{13}C CP experiments were conducted on samples **4** and **5** under MAS and stationary conditions using a Bruker Avance III NMR spectrometer (B_0 = 9.4 T, ν_0(^{13}C) = 100.61 MHz) equipped with a 4 mm triple resonance MAS probe. The chemical shifts were referenced externally to solid glycine (δ_{iso}(^{13}C=O) = 176.4 ppm with respect to TMS). π/2 pulse lengths ranging from 2.5 to 4.8 μs were employed and SPINAL-64 decoupling[53] was executed. Recycle delays were set to 2 s and contact times ranging from 2000 to 4000 μs were employed. A total of 4000 – 40000 scans were acquired for each spectrum in order to obtain optimal signal-to-noise ratio. For the MAS experiments, a spinning speed of 13 kHz was used, and RAMP CP was performed. Proton contact power was not ramped for static experiments. NMR data processing was accomplished using Bruker TopSpin 3.0 software, and the static ^{13}C spectra were fitted using WSolids1[9].

2.3.2 ^{11}B SSNMR Spectroscopy

All ^{11}B SSNMR experiments were performed using a Bruker Avance III NMR spectrometer (B_0 = 9.4 T, ν_0(^{11}B) = 128.38 MHz) with a 4 mm triple resonance MAS probe, and the chemical shifts were referenced externally to solid sodium borohydride (δ_{iso}(^{11}B) = -42.06 ppm with

respect to $F_3B{\cdot}O(C_2H_5)_2$). ^{11}B MAS and static spectra for samples **2**, **4** and **5** were recorded using the Hahn-echo sequence with TPPM decoupling[54] in order to suppress the boron background signal from the probe. The recorded free induction decays (FIDs) were left-shifted to the echo maxima. In order to maximize the CT signal, a $\pi/2$ pulse length of 1.9 μs was employed. The recycle delays were 2 s, and the echo delays were 77.15 μs. 16-3200 scans were recorded per spectrum and the spinning speed was set to 12.5 kHz for ^{11}B MAS experiments.

DQF *J*-resolved experiments with TPPM decoupling[54] were performed on all samples in order to measure the $J(^{11}B, ^{11}B)$ coupling constants. Double-frequency sweeps was also executed for signal enhancement.[55] For the $[B_2(CN)_6]^{2-}$ salts (samples **1**-**5**), the MAS frequency was 12 kHz and a 20 μs CT-selective $\pi/2$ pulse was used. The recycle delays were 2 s and the DQF delays ranged from 208 μs to 4.5 ms. 256 scans were collected per increment and a total of 31 t_1 increments were recorded. The incremented delays were approximately 389 μs. For the diboratellurenium salts (samples **6** and **7**), the samples were packed under argon atmosphere into 4mm o.d. ZrO_2 rotors. The spectra were recorded at 10 kHz MAS frequency with a 20.2 μs CT-selective $\pi/2$ pulse. Recycle delays of 2 s were used, and DQF delays of 1.25 to 1.5 ms were employed. 64 t_1 increments, with 256 scans per increment were obtained with an incremented delay of approximately 389 μs.

Bruker TopSpin 3.0 software was used for NMR data processing. The spectral splittings obtained in the indirect dimension of the ^{11}B DQF *J*-resolved experiments were analyzed by fitting the observed signals using mixed Gaussian/Lorentzian line shapes in order to extract the corresponding $J(^{11}B, ^{11}B)$ coupling constants.

2.3.3 Variable-Temperature (VT) SSNMR Spectroscopy

^{13}C and ^{11}B VT experiments was performed on sample **4** using a 4 mm o.d. zirconia rotor with zirconia caps, and a Bruker Avance III NMR spectrometer in a magnetic field of 9.4 T ($\nu_0(^{13}C)$ = 100.61 MHz, $\nu_0(^{11}B)$ = 128.38 MHz). A 4 mm triple resonance MAS probe was used for all VT experiments. Temperature calibration was conducted at 8 kHz with the ^{207}Pb signal from solid $Pb(NO_3)_2$ in order to correct for frictional heating.[56] Samples were allowed to equilibrate for 20 minutes at each temperature to ensure temperature stabilization. All NMR data were processed using Bruker TopSpin 3.0 software.

For the ^{13}C VT experiments, the sample was cooled using liquid nitrogen boil-off and spectra were recorded at temperatures ranging from 173 to 306 K under stationary conditions. $^{1}H \rightarrow {}^{13}C$ cross polarization with RAMP CP and SPINAL-64 decoupling[53] was performed and the $\pi/2$ pulse lengths were 2.25 μs. Contact times were set to 2000 μs and the recycle delays were set to 2 to 4 s. The chemical shifts were referenced externally to solid glycine ($\delta_{iso}(^{13}C{=}O)$ = 176.4 ppm with respect to TMS). The corresponding spectra were fitted using EXPRESS software[18] in order to extract the type of motions present in the system and the rate of the motions.

For the ^{11}B VT experiments, spectra were recorded at temperatures of 247 to 313 K under MAS condition with a spinning speed of 8 kHz. The Hahn-echo sequence with TPPM decoupling[54] was employed, and 1.9 μs $\pi/2$ pulse was used. Recycle delays of 2 s were employed and the echo delays were set to 98 μs. 64 scans were collected for each spectrum in order to obtain optimal signal-to-noise ratio. The chemical shifts were referenced externally to solid sodium borohydride ($\delta_{iso}(^{11}B)$ = -42.06 ppm with respect to $F_3B{\cdot}O(C_2H_5)_2$).

The $J(^{11}B, ^{11}B)$ couplings for **4** was also measured at low temperatures using DQF *J*-resolved SSNMR spectroscopy with TPPM decoupling[54] and double-frequency sweeps. The sample was spun at 8 kHz and a 20 μs CT selective $\pi/2$ pulse was employed. The recycle delays were set to 2 s and 5 s, and the DQF delay was set to 3 ms. 31 t_1 increments were measured with 256 scans per increment and an incremented delay of approximately 389 μs.

2.3.4 DFT Calculations

For the $[B_2(CN)_6]^{2-}$ salts (samples **1**-**5**), the corresponding $J(^{11}B, ^{11}B)$ coupling constants, the ^{11}B EFG tensors and the ^{13}C magnetic shielding tensors were calculated using the Amsterdam Density Functional Program (ADF, version 2012 and version 2016)[57]. All computations were executed using the revPBE functional with TZ2P basis set. The input structures were generated from the atomic coordinates of the $[B_2(CN)_6]^{2-}$ dianions as obtained from the published crystal structures (CCDC numbers 1049297, 1049194, 1049218, 1054696 and 1054695). Since samples **1**, **3**, **4**, and **5** are crystallographically disordered, the corresponding the minor disorder sites (i.e. sites with low partial occupancy) were removed for the calculations. As expected, geometry optimization resulted in identical geometries and therefore *J* couplings for all 5 samples (see Table 1); consequently, the NMR calculations were conducted on the crystal structures of the dianions without further optimizations. NLMO/NBO analysis was also conducted using the NBO program (version 5.0)[58] that is incorporated into ADF in order to investigate the electronic features of the systems and to determine the electronic origins of the *J* couplings. Sample input files for the DFT calculations are given in the Appendix.

Table 1 Theoretical $J(^{11}B,^{11}B)$ coupling constants of the series of $[B_2(CN)_6]^{2-}$ salts investigated in this study obtained with ($J(^{11}B, ^{11}B)_{geo\ opt}$) and without ($J(^{11}B, ^{11}B)_{no\ geo\ opt}$) geometry optimization of the input structures.

Sample	$J(^{11}B, ^{11}B)_{geo\ opt.}$[a]	$J(^{11}B, ^{11}B)_{no\ geo\ opt.}$[b]
1	27.1	26.9
2	27.1	24.9
3	27.1	28.1
4	27.1	30.3
5	27.1	28.2

[a]The minor disorder sites and the cations were removed from the coordinates obtained from the published crystal structures in order to attain structures consisting only of $[B_2(CN)_6]^{2-}$. The resulting structures were then geometry optimized using B3LYP functional with TZ2P basis set in order to generate the input structures for $J(^{11}B, ^{11}B)$ calculations. [b]Input structures were generated by removing the minor disorder sites and the cations from the coordinates obtained from the published crystal structures. No geometry optimization was performed.

J coupling calculations (using ADF, version 2012 and version 2016) and NBO/NLMO analysis (using the NBO program, version 5.0[58] and/or version 6.0[59], that is incorporated into ADF) were also performed on the diboratellurenium samples. The input structures were generated from the atomic coordinates obtained by single-crystal X-ray diffraction. In order to reduce computational requirements, the solvent molecules were removed and the isopropyl groups in the IDip ligands (IDip = 1,3-bis[diisopropylphenyl]imidazole-2-ylidene) were replaced with protons. The positions of the protons were then optimized using Gaussian 09, rev. D.01,[60] and the PBE functional with 3-21G basis set. NMR calculations were then performed using the same functional but with the TZP basis set. In order to take into account relativistic effects, ZORA was also implemented into the NMR calculations. Sample input files for the geometry optimization and the NMR calculations are provided in the Appendix.

3 Results and Discussion

3.1 Detecting Dynamic Disorder with DQF *J*-resolved SSNMR Spectroscopy

DQF *J*-resolved SSNMR spectroscopy can potentially be employed to detect molecular motions in solids since dynamics can result in apparent magnetic equivalency and magnetically equivalent nuclei have been shown to give rise to symmetry-amplified DQF *J* splittings (see section 1.4); therefore, for a pair of crystallographically distinct borons, we hypothesize that symmetry-amplified *J* splittings can still result if dynamic disorder is present. In order to test this hypothesis, a series of $[B_2(CN)_6]^{2-}$ salts (Figure 22) was investigated, and salts which contain pairs of crystallographically inequivalent borons and display dynamic disorder at room temperature were identified and employed as archetypes. The $[B_2(CN)_6]^{2-}$ salts have been previously characterized by single-crystal X-ray diffraction,[37] and it was found that samples **1**-**3** contains pairs of equivalent borons due to the presence of an inversion center (Figure 28). Since the powder diffraction pattern of **2** acquired at 298 K did not match with the pattern simulated from the previously reported crystal structure that was acquired at 100 K, the crystal structure of **2** was redetermined at room temperature (CCDC-1521872). Similar to the low-temperature structure, the $[B_2(CN)_6]^{2-}$ dianion of **2** at 298 K was found to be located on an inversion center. The cations were found to be disordered, however, no disorder was observed for the anion (Figure 29). On the other hand, the single-crystal X-ray diffraction data shows that **4** and **5** encompasses pairs of

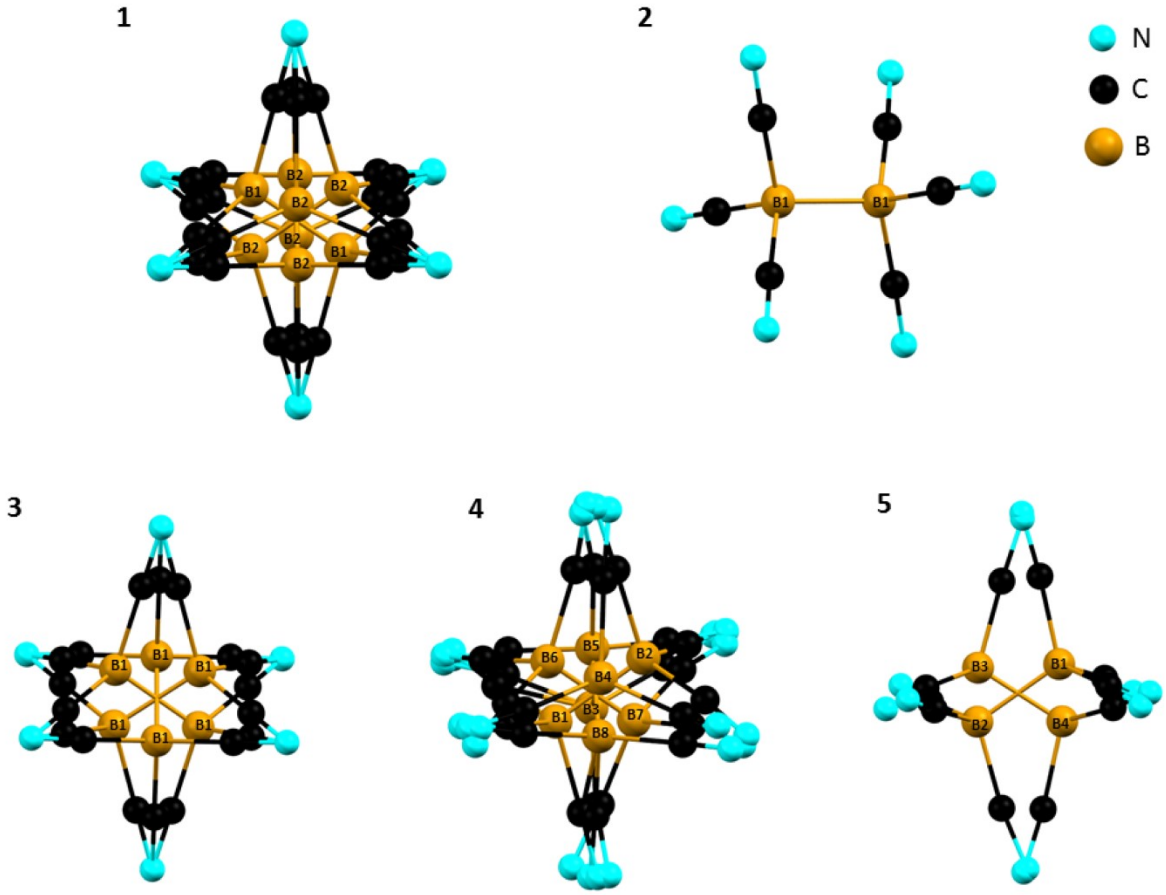

Figure 28 Crystal structures of the $[B_2(CN)_6]^{2-}$ anion of samples **1**-**5** as obtained from single-crystal X-ray diffraction,[37] illustrating the presence of crystallographic disorder in **1**, **3**-**5**. Samples **1**-**3** consist of pairs of crystallographically equivalent boron nuclei, while samples **4** and **5** contain pairs of inequivalent boron nuclei.

crystallographically inequivalent borons as they are unrelated by any symmetry operations (Figure 28). Furthermore, these two salts can potentially exhibit dynamics as the corresponding crystal structure indicates the presence of crystallographic disorder. Consequently, a series of ^{11}B and ^{13}C SSNMR experiments were conducted on **4** and **5** in order to determine if these borons are dynamically disordered.

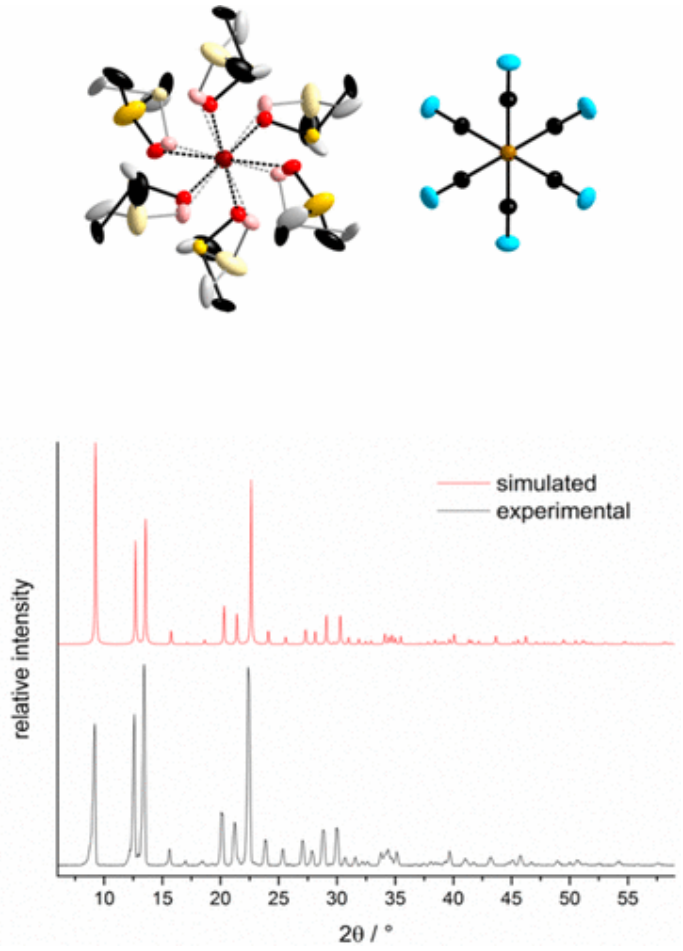

Figure 29 The crystal structure of **2** as obtained at 298 K (view along [001]; displacement ellipsoids at 15% probability) (top) and the corresponding simulated and experimental X-ray diffraction powder patterns (bottom).

Firstly, ^{13}C CP/MAS spectra were recorded for **4** and **5** (Figure 30), and a discrepancy between the number of inequivalent carbons as indicated by X-ray diffraction and the number of detected ^{13}C resonances was observed. According to the crystal structures, **4** and **5** consist of a total of 60 and 44 nonequivalent carbons, respectively, as contributed from both the anion and the cation. Therefore, if these samples do not undergo molecular motions, we would expect 60 and 44 ^{13}C signals for **4** and **5**, respectively, under MAS. However, only 7 peaks for **4** and 12

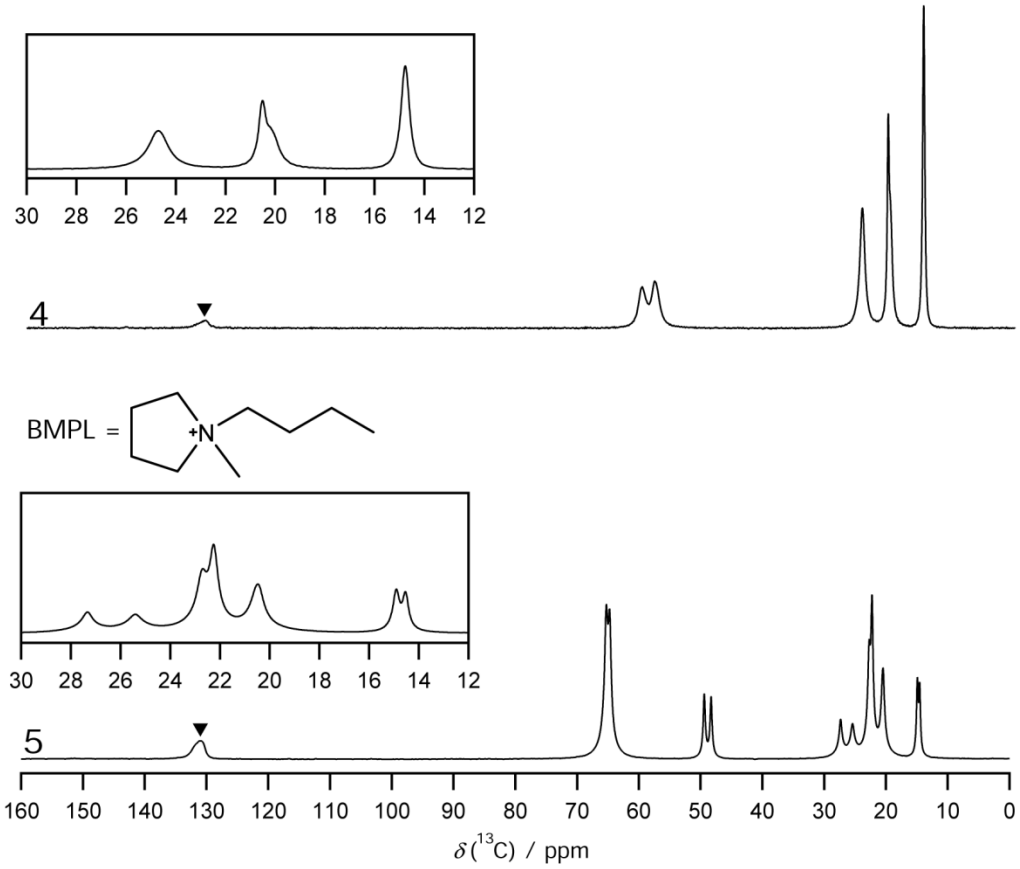

Figure 30 ^{13}C CP/MAS SSNMR spectra of **4** and **5** measured at room temperature and at 9.4 T (MAS speed = 13 kHz). Solid triangles (▼) denote the carbon signals arising from the nitrile carbons. Insets show expansion of the region from 12 to 30 ppm.

peaks for **5** was observed in our ^{13}C CP/MAS spectra, which is significantly less than what is anticipated even when coincidental peak overlap was taken into consideration. Since molecular motion which is fast on the NMR time scale can generate equivalency between different sets of carbons (see section 1.1.3), this reduction in ^{13}C signals then suggests the presence of dynamics in **4** and **5**. Furthermore, the crystal structures of **4** and **5** indicate disorder in the nitrile carbons (Figure 28). Since these carbons are directly bonded to the borons, if the borons are influenced by molecular motion, these carbons should be as well. As seen from the crystal structures, there

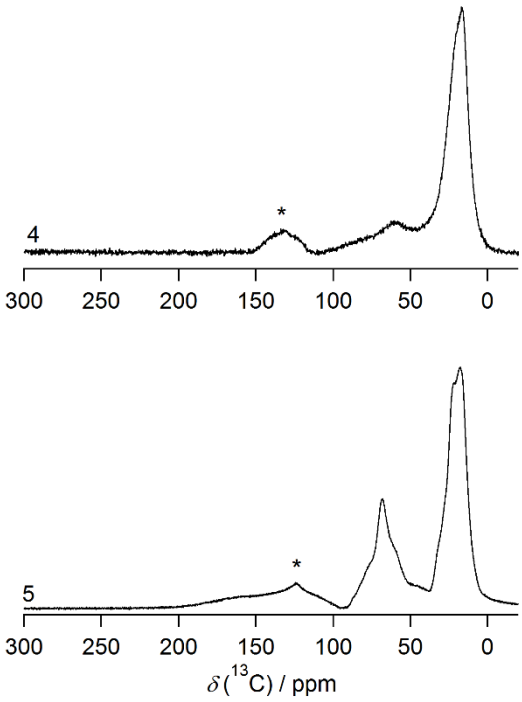

Figure 31 Static ^{13}C CP SSNMR spectra of **4** and **5** recorded at 306 K and 9.4 T. Asterisk denotes the nitrile carbon signal.

are 24 and 8 disorder sites for the nitrile carbons of **4** and **5**, respectively. Nevertheless, only one nitrile carbon peak ($\delta_{iso}(^{13}C)$ = 131.1 ppm) was observed for both of these samples (Figure 30). This significant reduction in the number of nitrile carbon signals indicates that these $[B_2(CN)_6]^{2-}$ anions feature dynamic disorder. Additional evidence for the presence of motions in the $[B_2(CN)_6]^{2-}$ anions of **4** and **5** was also obtained via static ^{13}C CP SSNMR experiments (Figure 31). The corresponding nitrile carbon signals were simulated (Figure 32) in order to obtain the ^{13}C CS tensor parameters which are provided in Table 2 together with the respective theoretical values. The δ_{iso} extracted from the static ^{13}C spectra were in good agreement with the computational values, MAS values (131.1 ppm for **4** and **5**), as well as the literature values for different

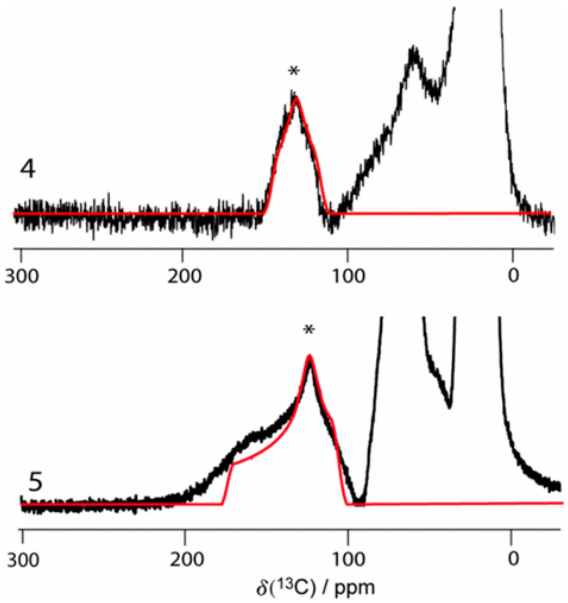

Figure 32 Experimental ^{13}C CP SSNMR spectra of **4** and **5** (black trace) recorded under stationary conditions (B_0 = 9.4 T and T = 306 K) and expanded to highlight the corresponding nitrile signal, which is denoted by the asterisk. Simulated spectra generated from the parameters given in Table 2 is also provided (red trace). The remaining signals located in the range of 0-100 ppm are due to the ^{13}C of the corresponding cation. The full range spectra are given in Figure 31.

nitriles (ca. 108 to 168 ppm)[61-65]. The theoretical Ω was calculated to range from 348 to 352 ppm, which is consistent with the previously reported values (328 to 361 ppm) for nitrile carbons in solids without dynamic (i.e. AgCN, CuCN, $M[Au(CN)_2]$ salts (M = nBu$_4$N, K, and Tl), $Pb(H_2O)[Au(CN)_2]_2$, $Pb[Au(CN)_2]_2$ and $K_n[M(CN)_4]$ salts (M = Zn, Cd, Hg, and Au, n = 1 or 2))[61-65] and the experimental Ω estimated from a statically disordered $[B_2(CN)_6]^{2-}$ salt (328 ppm, see Figure 33). However, the experimental Ω was measured to be 30 ppm for **4** and 69 ppm for **5**, which is 80-90% smaller than the corresponding DFT values. The experimental κ was also found to deviate from the theoretical results. κ was measured to be ~0 for **4** and -0.46 for **5**, however it was calculated to range from 0.95 to 0.96. Since the DFT calculations were conducted

Table 2 Experimental and theoretical ^{13}C CS tensor parameters of the nitrile carbons of samples **4** and **5**

sample	carbon site[a]	theoretical			experimental[b]		
		δ_{iso} / ppm	Ω / ppm	κ	δ_{iso} / ppm	Ω / ppm	κ
4	1	129.8	348	0.96	131.0 ± 1.0	30 ± 7	0.00 ± 0.20
	2	129.6	349	0.96			
	3	130.2	349	0.95			
	4	129.6	348	0.95			
	5	129.5	348	0.95			
	6	129.4	348	0.95			
5	1	132.2	352	0.96	135.2 ± 1.2	69 ± 10	-0.46 ± 0.06
	2	132.4	352	0.95			
	3	132.4	352	0.95			
	4	132.8	352	0.95			
	5	131.5	350	0.95			
	6	131.5	350	0.95			

[a]Each number correspond to a crystallographically distinct nitrile carbon found in the major disorder site. [b]Only one carbon signal was observed in the corresponding SSNMR spectra of **4** and **5**, as shown in Figure 32.

using stationary models (i.e. at 0 K) and since molecular motion can result in the averaging of CS tensors (see section 1.1.3), the reduction in the experimental Ω and the difference between the measured and the calculated κ both suggests that **4** and **5** consist of dynamic disorder.

To further probe the influence of molecular motions, ^{13}C VT experiments were conducted on **4** at low temperatures (Figure 34). As the temperature is decreased from 306 to 258 K, the effect of motion on the CS tensor is lessened, thereby resulting in broadening of the nitrile carbon signal and the appearance of a full powder pattern. No additional changes in the line shapes were observed when the sample temperature was further decreased from 258 K, indicating that the motion is static on the NMR time scale at temperatures $\leq$ 258 K. Information regarding the

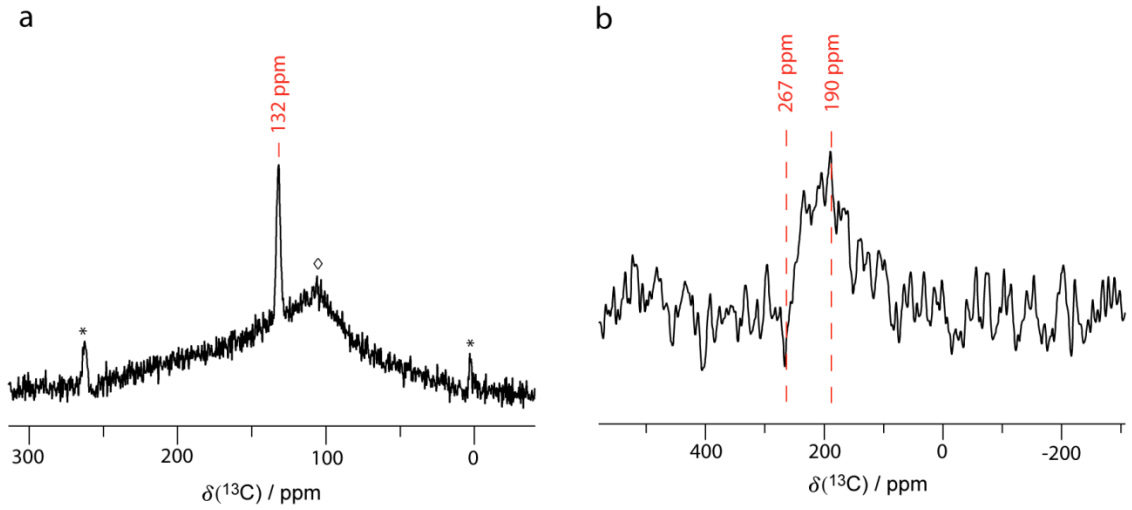

Figure 33 ^{13}C SSNMR spectra of **3** recorded under MAS using a one-pulse experiment (a) and static conditions using the Hahn echo sequence (b) at 9.4 T. Since the sample does not contain any protons, both spectra were obtained using a direct ^{13}C-observe experiments. A 180 s recycle delay was employed. The diamond in (a) denotes background signal, while asterisks denote spinning sidebands. By using δ_{iso} obtained from the MAS spectrum (δ_{iso} = 132 ppm), and the δ_{11} and δ_{22} obtained from the static spectrum (δ_{11} = 267 ppm and δ_{22} = 190 ppm), the Ω was approximated to be 328 ppm.

type and the rate of motion present were also extracted from our spectra via EXPRESS[18]. EXPRESS[18] simulates the effect of dynamics on SSNMR line shapes using the Markov model, where the time spent at each hopping site is assumed to be infinitely small in comparison to the rate of hopping,[5] and has been shown to be effective for determining the types and rates of motions in solids from the corresponding SSNMR spectra.[66] The Ω and κ values (348 ppm and 0.95, respectively) acquired from our DFT calculations on a static molecule were employed for the EXPRESS[18] simulations, and an excellent agreement was obtained between the experimental spectrum recorded at temperatures less than and/or equal to 258 K (where the motion is static on

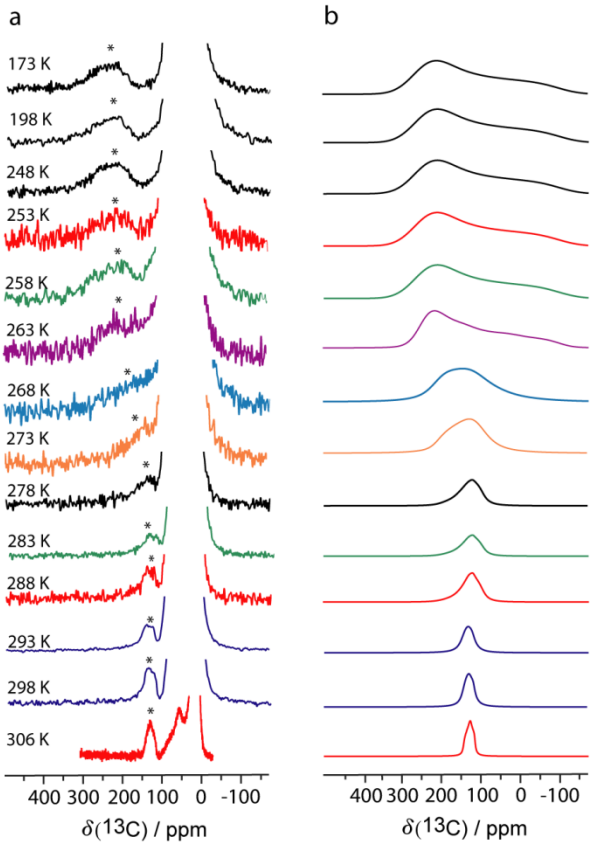

Figure 34 (a) Static ^{13}C CP SSNMR spectra of **4** measured at B_0 = 9.4 T and at temperatures ranging from 306 to 173 K. The nitrile carbon signal (as denoted by the asterisks) was simulated using EXPRESS[18] (b) in order to extract the rates for motional processes A, B and C (Table 3). The remaining signal observed in the experimental spectra result from the *n*Bu$_4$N cation. Additional simulation parameters (angles and CS tensor values) are given in Table 4.

the NMR time scale) and the simulated spectrum (Figure 34). In order to determine the motional processes exhibited by the dianion, the crystal structure of the dianion of **4** (Figure 28) was inspected. As the bonding structures of the B(CN)$_3$ groups are geometrically similar to that of a CH$_3$ group, the effects of a 3-fold jump along the B-B axis (denoted as process A from here on), which is analogous to a methyl group rotation, on the spectra is first examined. Theoretically, this would reduce the chemical shift anisotropies by a factor of 0.34 as compared to that of a

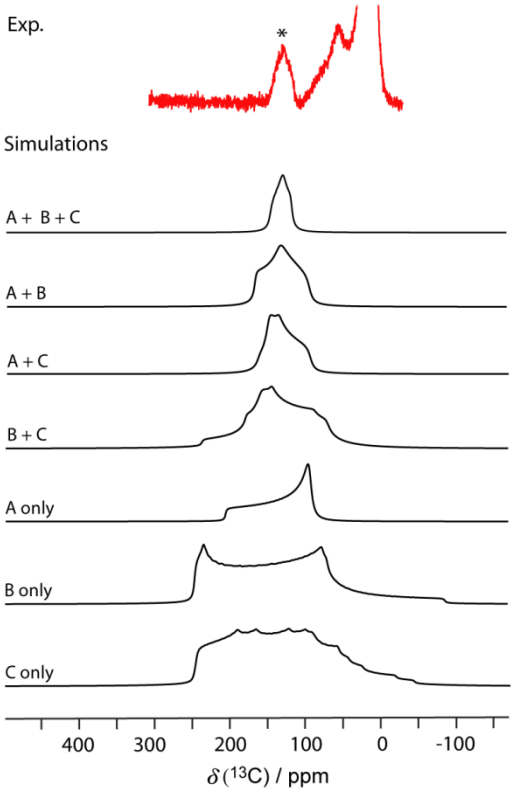

Figure 35 The nitrile ^{13}C resonance of **4** recorded at 306 K is simulated here using EXPRESS[18] and different combinations of the motional processes A, B, and C. In order to successfully reproduce the experimental spectrum, all three processes must to be considered

static model since fast reorientation around a single axis would scale the chemical shift anisotropies by $\frac{3\cos^2\theta-1}{2}$ (see section 1.1.3),[5] where $\theta = 71^{o}$ in this case. Nonetheless, as the Ω at the high temperature limit was measured to be ca. 80-90% smaller than that at the low temperature limit, process A alone is not enough to account for the observed line shape at 306 K (Figure 35); consequently, additional modes of motions must be considered. Two other types of 2-fold jump motions (process B and process C) were examined based on the disorder sites identified in the single-crystal diffraction structure. In process B, one of the borons in the $[B_2(CN)_6]^{2-}$ dianion (boron X) jumps from site B4 to B6, while the other boron (boron Y) jumps from site B3 to B7

Table 3 Rates for motional processes A, B and C (τ^{-1}_A, τ^{-1}_B, τ^{-1}_C) in **4** over the temperature range of 306-173 K. The rates were obtained by simulating the ^{13}C VT SSNMR spectra using EXPRESS[18] as shown in Figure 34.

Temperature / K	τ^{-1}_A / kHz	τ^{-1}_B / kHz	τ^{-1}_C / kHz
306 K	1000	200	200
298 K	600	50	50
293 K	500	30	30
288 K	500	10	10
283 K	400	9	9
278 K	400	8	8
273 K	80	3	3
268 K	40	0.8	0.8
263 K	50	0.3	0.3
258 K	1	0.1	0.1
253 K	1	0.1	0.1
248 K	1	0.1	0.1
198 K	1	0.1	0.1
173 K	1	0.1	0.1

(see Figure 28 for the disorder site labels). In process C, boron X moves from sites B4 and B6 to B5 and B2, while boron Y moves from sites B3 and B7 to B1 and B8 (see Figure 28 for the disorder site labels). Similar to process A, process B and process C alone is inefficient in reproducing the experimental results (Figure 35). However, when the three processes are all taken into consideration, the experimental spectra were successfully simulated (Figure 34 and Figure 35), and the corresponding rates and angles employed for the simulations are provided in Table 3 and Table 4, respectively. Consistent with previous SSNMR studies on molecular dynamics which illustrated that ^{13}C CS tensors are sensitive to motions occurring at ca. 10^2 to 10^9 s^{-1},[66-69] the motional rates for process A were found to range from 10^6 to 10^3 s^{-1}, while the rates for process B

Table 4 ^{13}C CS tensor magnitudes (δ_{iso}, Ω, κ) and angles (α, β and γ) employed to simulate the ^{13}C VT SSNMR spectra of **4** (Figure 34). The same angles were employed for the entire temperature range (306-248 K).

δ_{iso} / ppm	131.0
Ω / ppm	348
κ	0.95
α_A / º	0, 0, 0
α_B / º	0, 0
α_C / º	0, 0
β_A[a] / º	71, 71, 71
β_B[a] / º	0, 72.6
β_C[a] / º	90, 36.3
γ_A / º	0, 120, 240
γ_B / º	0, 300
γ_C / º	45, -45

[a]Angles were extracted from previously published single-crystal X-ray diffraction data acquired at 100K.

and C were found to be ~10^5 to 10^2 s^{-1} (Table 3). Moreover, these motions could render the nitrile carbons and the borons equivalent in the fast motion limit, which is in agreement with the observed ^{13}C MAS spectra (Figure 30) and the ^{11}B MAS spectra (discussion will be presented in the upcoming paragraph). Nonetheless, it should be noted that the motional model purposed here is not the only model which can be employed to simulate our data. As with any line shape analysis, various models which would all provide equally adequate fits can often be employed for spectral fitting in motion analysis.[5] Furthermore, as see in Figure 34, some of our spectra consist of low signal-to-noise ratio. Line broadening due to various processes (such as peak overlap of the resonances from crystallographically distinct carbons and broadening due to coupling interactions between ^{13}C and ^{11}B, ^{10}B and ^{14}N) that are reintroduced as the motion is slowed down can also be seen in our low temperature spectra, resulting in relatively indistinct spectral features.

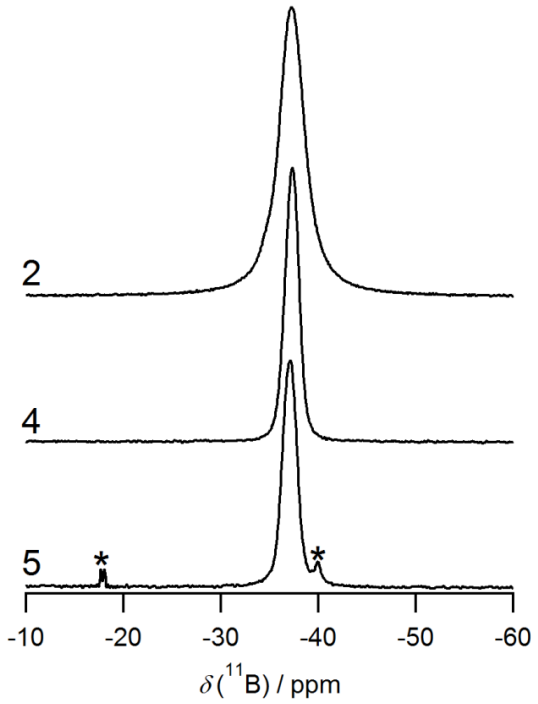

Figure 36 ^{11}B Hahn echo MAS spectra of **2**, **4** and **5** recorded at room temperature with a spinning frequency of 12.5 kHz. B_0 = 9.4 T. Asterisks denote impurities.

As such, it is impossible to unambiguously fit all of our spectra and to explicitly determine the motional model.

Since our interest lies in the boron atoms, a series of ^{11}B SSNMR experiments were conducted in order to directly probe the corresponding motions. In agreement with our ^{13}C data, the results obtained from ^{11}B experiments also indicate that the $[B_2(CN)_6]^{2-}$ dianions are dynamically disordered. For both **4** and **5**, a single pseudo-Lorentzian ^{11}B peak (δ_{iso} = -37 ppm) was observed under MAS (Figure 36). This is consistent with the pseudo-tetrahedral environment of the borons since quadrupolar nuclei in highly spherical electronic environments can be expected to experience minimal second-order quadrupolar coupling.[8] Similar results were obtained from our

Table 5 Theoretical ^{11}B EFG tensor parameters for samples **1**-**5**.

sample	boron site[a]	C_Q / MHz	η
1	1[b]	-0.90	0.00
2	1[b]	-0.88	0.03
3	1[b]	-0.94	0.05
4	1	-0.96	0.02
	2	-0.94	0.05
5	1	-0.80	0.08
	2	-0.79	0.11

[a]Each number corresponds to a crystallographically distinct boron in the major disorder site. [b]Both borons were found to be crystallographically equivalent by single-crystal X-ray diffraction.

theoretical calculations (Table 5) where a small $C_Q(^{11}B)$ was calculated for the inequivalent borons in the major disorder sites (-0.96 and -0.94 MHz for **4** and -0.80 MHz and -0.79 MHz for **5**). Moreover, the linewidths of **4** and **5** (full width at half maximum (FWHM) = 203.9 Hz for **4** and 214.8 Hz for **5**) is noticeably narrower than that of **2** (FWHM = 388.2 Hz) (Figure 36), which also consists of borons in a pseudo-tetrahedral environment and therefore a similar $C_Q(^{11}B)$ value (-0.88 MHz). Since **2** is not crystallographically disordered (Figure 29) and therefore the corresponding $[B_2(CN)_6]^{2-}$ dianions are static, the decrease in linewidth seen in **4** and **5** can be attributed to the motional averaging of the anisotropic tensors. Similar observation has been made in the case of carborane, where rapid isotropic reorientation in the solid state was found to result in remarkably narrow ^{11}B linewidths.[70,71] This effect was also detected in our static ^{11}B SSNMR spectrum of **4**, in which the corresponding resonance was found once again to be sharper than that of **2** (Figure 37). We were unable to draw similar conclusion for **5** due to peak overlap as a result of impurities (see Figure 38). Referring back to our ^{11}B MAS spectra, the X-ray diffraction data indicates that a total of 8 and 4 ^{11}B resonances should be

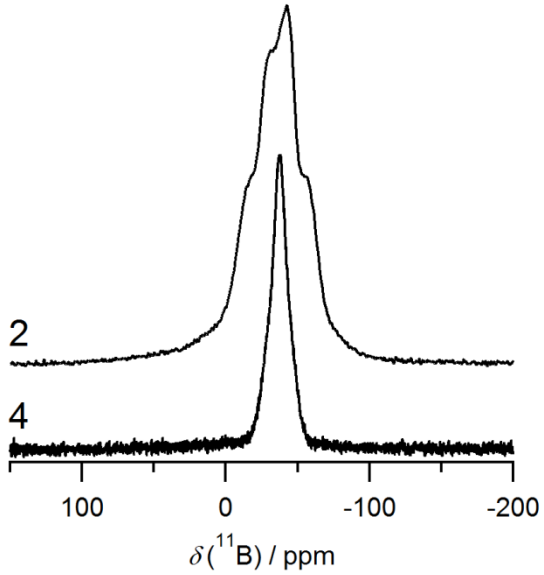

Figure 37 ^{11}B SSNMR spectra of **2** and **4** measured using the Hahn echo sequence under stationary conditions (room temperature, B_0 = 9.4 T).

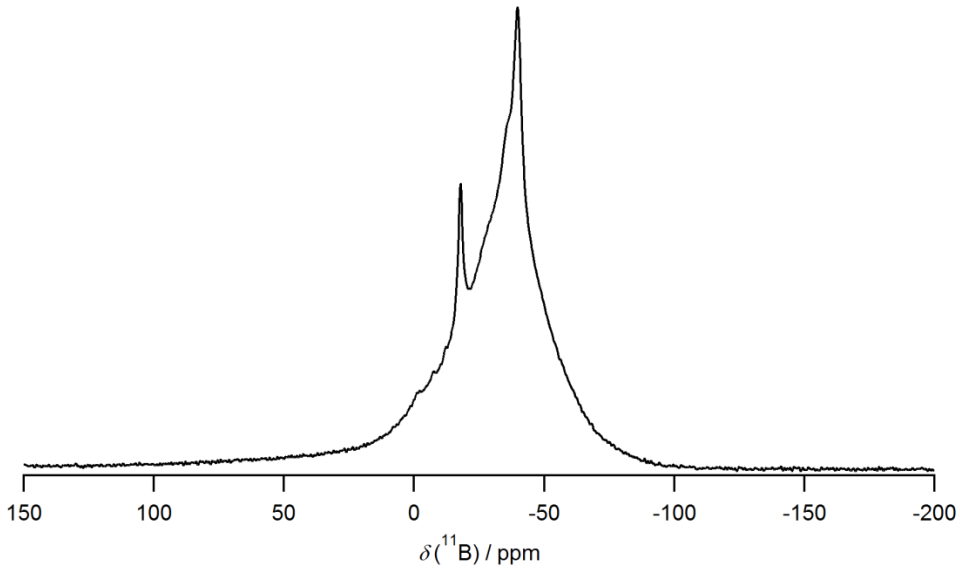

Figure 38 SSNMR spectrum of **5** recorded using the Hahn echo sequence under stationary condition at room temperature (B_0 = 9.4 T).

observed for **4** and **5**, respectively, under MAS due to the crystallographic inequivalency of the borons. However, only a single peak was found for both compounds, indicating that equivalency between different sets of boron is generated as a result of the fast reorientation of the dianions. More important, since each ^{11}B NMR signal corresponds to a distinct boron, the single resonance detected thus suggests that all of the boron nuclei in **4** and **5** are at least chemically equivalent on the time scale of the experiment.

^{11}B VT MAS experiments were also conducted on **4** to further investigate the dynamic process (Figure 39). It has been illustrated by Griffin et al. that activation energy (E_a) can be estimated from VT MAS experiments via the Arrhenius equation, assuming that the motionally broadened linewidth is proportional to the rate constant.[72] Consequently, E_a can be obtained from a $\ln(\Delta\nu^{mot})$ vs 1/T plot via the relation

$$\frac{\mathrm{d}\ln(\Delta\nu^{mot})}{\mathrm{d}\,(1/T)} = \pm\frac{E_a}{R} \qquad 27$$

where $\Delta\nu^{mot}$ is obtained by subtracting the inherent linewidth from the observed MAS linewidth, T is temperature, and R is the molar gas constant 8.314 J K^{-1} mol^{-1}.[72] However, our attempt to extract the E_a of the motional processes from our ^{11}B linewidths was unsuccessful since multiple dynamic processes are present and the inherent linewidth was unknown. From our data, the E_a was found to be 9.1 kJ mol^{-1} (Figure 40) if the inherent linewidth was estimated to be half of the FWHM of the high temperature linewidth. Given that the motion can be slowed down at near room temperature, as indicated by the change in the ^{11}B linewidths at temperatures of 247 to

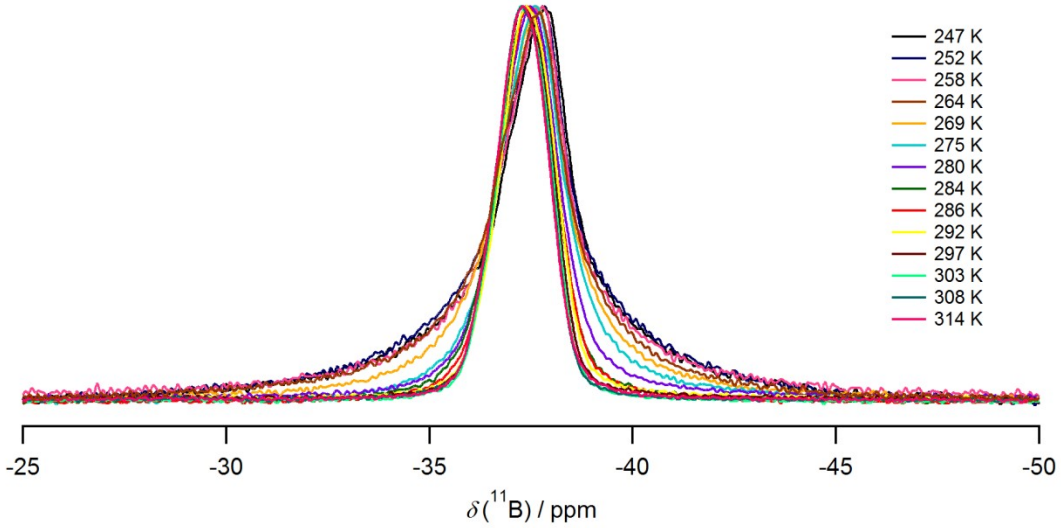

Figure 39 ^{11}B VT MAS SSNMR spectra of **4** recorded at temperatures ranging from 247 to 314 K with a spinning speed of 8 kHz. B_0 = 9.4 T.

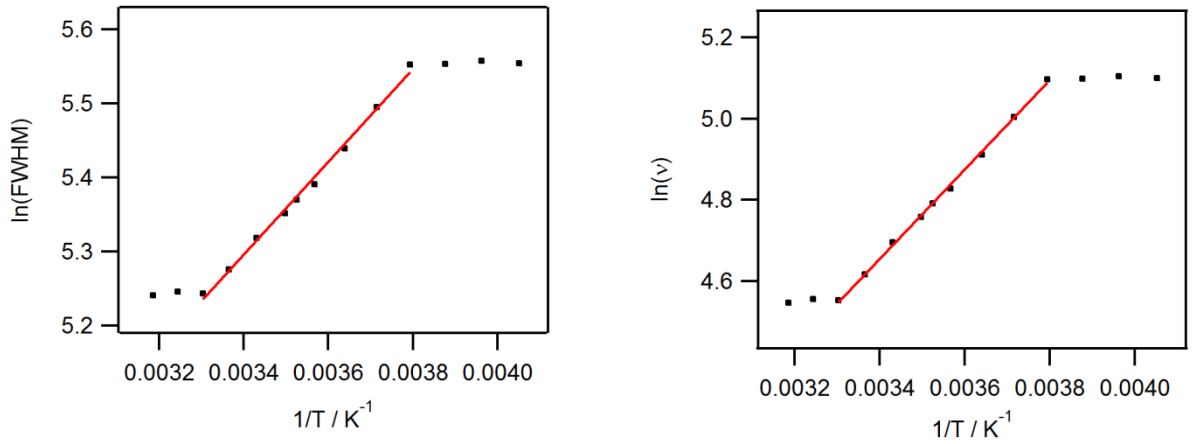

Figure 40 Arrhenius plots constructed based on the ^{11}B MAS linewidth of **4**. When the FWHM was employed (left), an activation energy of 5 kJ mol^{-1} is obtained. On the other hand, when the inherent linewidth, which was estimated to be half of the FWHM of the high-temperature linewidth, was subtracted from each of the FWHM, an activation energy of 9.1 kJ mol^{-1} is acquired (right).

314 K (Figure 39), we would expect the E_a to be relatively large in comparison to molecular motions which are known to be persistent even at low temperatures, such as a methyl rotation. However, when compared to the E_a for methyl rotation (ca. 12 kJ mol^{-1})[73], the E_a we extracted from our ^{11}B spectra seems too low to be physically meaningful. Nonetheless, these ^{11}B VT experiments provide additional evidence for the existence of dynamics in **4** as a decrease in temperature resulted in an increase in linewidth, which is consistent with the reintroduction of the anisotropic broadening interactions and distinct sites at lower temperatures.

As mentioned in section 1.4, it has been established by previous works that, in the absent of dynamics, a splitting of *J* will be observed in the ^{11}B DQF *J*-resolved spectra if the borons are crystallographically (and therefore magnetically) inequivalent, while for a pair of magnetically equivalent borons, the splitting will be 3*J*.[27,29,30] Even though the boron nuclei in **4** and **5** were found to be crystallographically distinct by X-ray diffraction, we still anticipate the corresponding DQF *J* splittings to be amplified by a factor of 3 due to the apparent magnetic equivalence that is induced by dynamic disorder. As expected, the DQF *J* splittings for these two samples were found to be approximately 3 times larger than the calculated *J*(^{11}B, ^{11}B) values (107.3 Hz vs 30.3 Hz for **4**, and 101.2 Hz vs 28.2 Hz for **5**), and the corresponding spectra are provided in Figure 41. VT ^{11}B DQF *J*-resolved experiments were also performed on **4** at 297 to 247 K (Figure 42). A splitting of 3*J* was found in this temperature range; however, a decrease in temperature resulted in a substantial decrease in the signal-to-noise and at temperatures lower than 284 K, no signal was observed. This was most likely due to a decrease in the ^{11}B T_2 as attributed to the reduction in the dynamic rate. Previous simulations on the transition from magnetic equivalence to chemical equivalence also suggests that a reduction in signal-to-noise can be

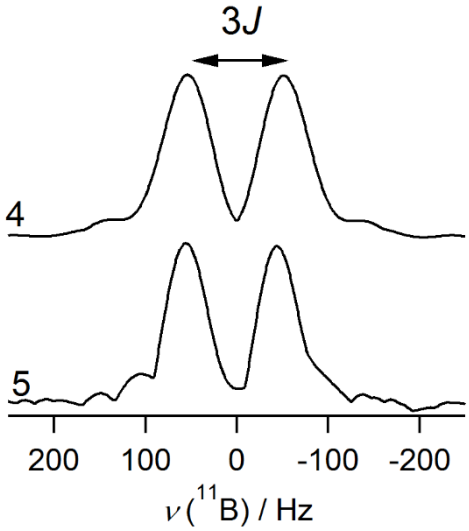

Figure 41 Indirect dimension of the ^{11}B DQF *J*-resolved SSNMR spectra of **4** and **5** recorded at room temperature and at 9.4 T. The sample was spun at 12 kHz. The *J* splittings were found to be 3 times larger than the corresponding calculated $J(^{11}B, ^{11}B)$ coupling constant (as provided in Table 6) due to the apparently magnetic equivalence generated by molecular motions.

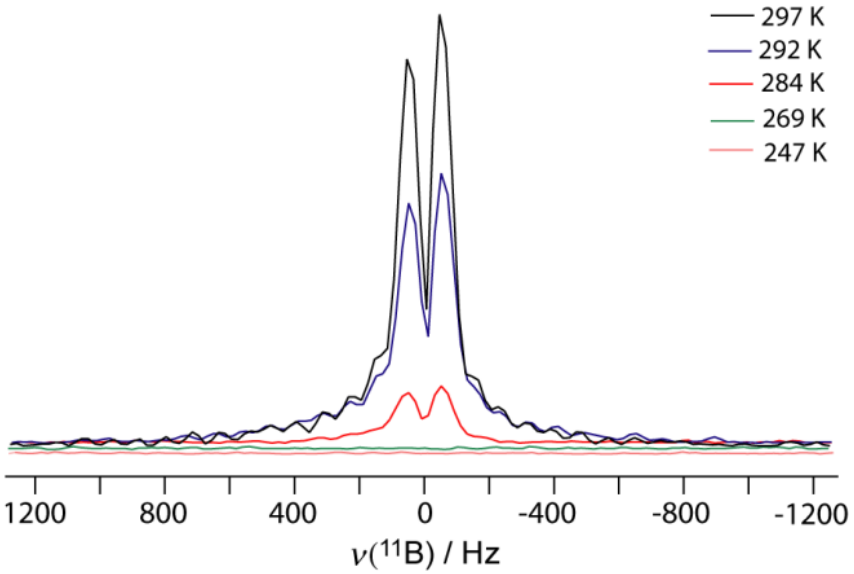

Figure 42 Indirect dimension of the ^{11}B DQF *J*-resolved spectra of **4** recorded at temperatures of 297 to 247 K with a spinning speed of 8 kHz (B_0 = 9.4 T). A splitting of 3*J* was observed in this temperature range. The decrease in temperature resulted in a decrease in signal-to-noise, and no signal was observed at temperatures below 284 K.

expected.[74] Nonetheless, these low temperature data are consistent with our initial hypothesis, and our ^{11}B DQF *J*-resolved experiments illustrate that the appearance of the DQF *J*-resolved spectra can be influenced by the effective magnetic equivalency between boron spins generated by molecular dynamics. Consequently, in order to correctly extract the *J* coupling constants, dynamic disorder must be accounted for when performing DQF *J*-resolved experiments. More significantly, these results suggest that these experiments can potentially be employed to investigate molecular dynamics if the crystallographic symmetry of the system and the corresponding *J* coupling constants are known.

3.2 Probing the Electronic Structures of Diboron Systems with *J*(^{11}B, ^{11}B) Coupling Constants

The *J*(^{11}B, ^{11}B) coupling constants have been previously reported to correlate with various electronic features of the diboron systems; however, these studies were only performed on non-cyclic compounds with B-B bonds formed from sp^1 to sp^2 hybridized boron orbitals.[29,30] In order to develop a more comprehensive relation between *J* coupling constants and electronic structures, we've measured the *J*(^{11}B, ^{11}B) coupling constants of systems with electron-precise 2c-2e B(sp^3)−B(sp^3) bonds (i.e. the $[B_2(CN)_6]^{2-}$ salts, Figure 22) and cyclic boron compounds (i.e. the diboratellurenium salts, Figure 23) using ^{11}B DQF *J*-resolved SSNMR spectroscopy. The corresponding spectra are provided in Figure 41 and Figure 43, while the measured *J* coupling values are given in Table 6. As anticipated, symmetry-amplified DQF *J* splittings were observed

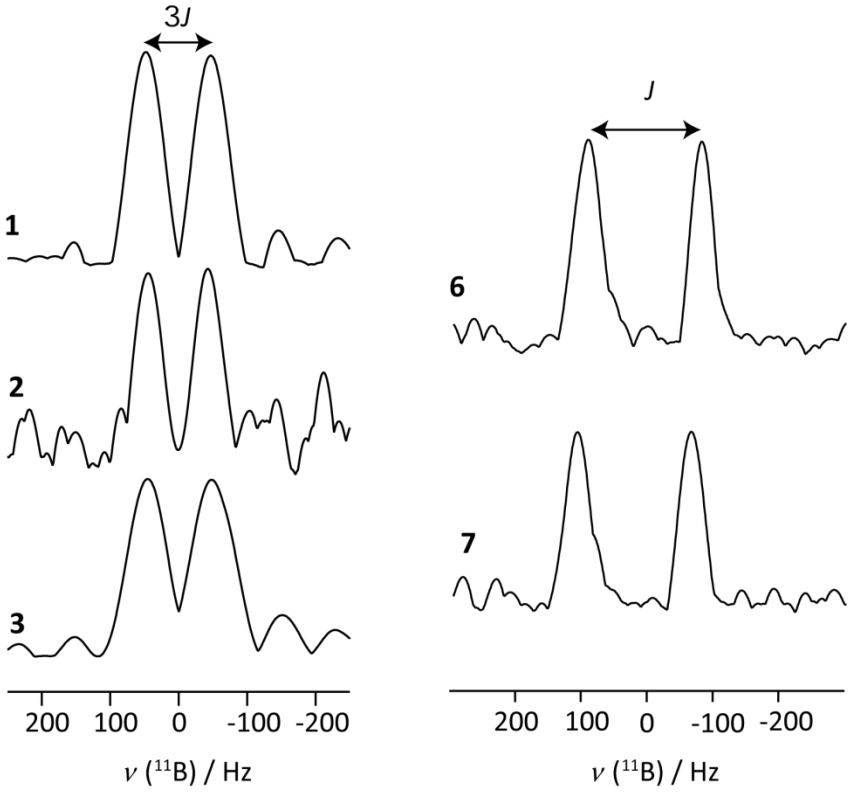

Figure 43 Indirect dimension of the ^{11}B DQF *J*-resolved SSNMR spectra of **1**-**3**, **6** and **7** recorded at B_0 = 9.4 T with a spinning speed of 12 kHz for **1**-**3** and 10 kHz for **6** and **7**.The DQF *J* splittings were found to be amplified by a factor of 3 for **1**-**3** as the borons are equivalent due to the presence of an inversion center (Figure 28), while a splitting of *J* was observed for **6** and **7** since these samples consist of pairs of inequivalent borons (Figure 44).

for samples **1** (*J* splitting = 95.3 Hz, $J(^{11}B, ^{11}B)_{calc.}$ = 26.9 Hz), **2** (*J* splitting = 88.3 Hz, $J(^{11}B, ^{11}B)_{calc.}$ = 24.9 Hz) and **3** (*J* splitting = 95.0 Hz, $J(^{11}B, ^{11}B)_{calc.}$ = 28.1 Hz) since the bonded borons in these samples are related by an inversion center as indicated by X-ray diffraction (Figure 28). Samples **4** and **5** also gave amplified *J* splittings (*J* splitting = 107.3 Hz and $J(^{11}B, ^{11}B)_{calc.}$ = 30.3 Hz for **4** and *J* splitting = 101.2 Hz and $J(^{11}B, ^{11}B)_{calc.}$ = 28.2 Hz for **5**) due to the presence of dynamics as discussed in the previous section. On the other hand, a splitting of *J* was observed for both **6** and **7** (*J* splitting = 171.4 Hz and $J(^{11}B, ^{11}B)_{calc.}$ = 171.8 Hz for **6**, and

Table 6 Experimental ($J(^{11}B, ^{11}B)_{exp.}$) and theoretical ($J(^{11}B, ^{11}B)_{calc.}$) $J(^{11}B, ^{11}B)$ coupling constants, B-B σ-bonding NBO energies (σ(B-B) NBO energy) and the p-orbital hybridization indexes of the B-B bonds (hybridization index) of the samples investigated in this study.

sample	$J(^{11}B, ^{11}B)_{exp.}$ / Hz	$J(^{11}B, ^{11}B)_{calc.}$ / Hz	σ(B-B) NBO energy / a.u.	hybridization index
1	31.8 ± 0.2	26.9	-0.066	2.90
2	29.4 ± 0.3	24.9	-0.061	2.99
3	31.7 ± 0.4	28.1	-0.067	2.83
4	35.8 ± 0.4	30.3	-0.072	2.76
5	33.7 ± 0.5	28.2	-0.070	2.84
6	171.4 ± 0.6	171.8[a]	-0.534[a]	1.03[a]
7	172.8 ± 0.7	171.5[a]	-0.534[a]	1.04[a]

[a]The isopropyl groups of the IDip ligands were replaced with protons in the input structure used for calculations.

J splitting = 172.8 Hz and $J(^{11}B, ^{11}B)_{calc.}$ = 171.5 Hz for **7**) since the borons in these samples were found to be crystallographically inequivalent (Figure 44). Furthermore, it has been illustrated that the coupling constants can be retrieved using DFT calculations as the experimental $J(^{11}B, ^{11}B)$ coupling constants were found to correlate linearly with the corresponding theoretical value for diboron systems without dynamic disorder.[29] As seen in Table 6, we obtained a good agreement between the calculated and experimental $J(^{11}B, ^{11}B)$ coupling constants for the $[B_2(CN)_6]^{2-}$ dianions and the diboratellurenium compounds. Nevertheless, a slight deviation from linearity was observed when the J coupling constant measured for the $[B_2(CN)_6]^{2-}$ dianions was plotted against the respective theoretical values (Figure 45, $J_{exp.} = 1.14J_{calc.} + 0.89$ Hz; $R^2 = 0.90$). Since the DFT calculations were conducted using the atomic coordinates of only the major disorder sites and also under static conditions (at $T = 0$ K), the deviation of R^2 from linearity is therefore expected as the input structures for samples with dynamic disorder do not fully represent the real system.

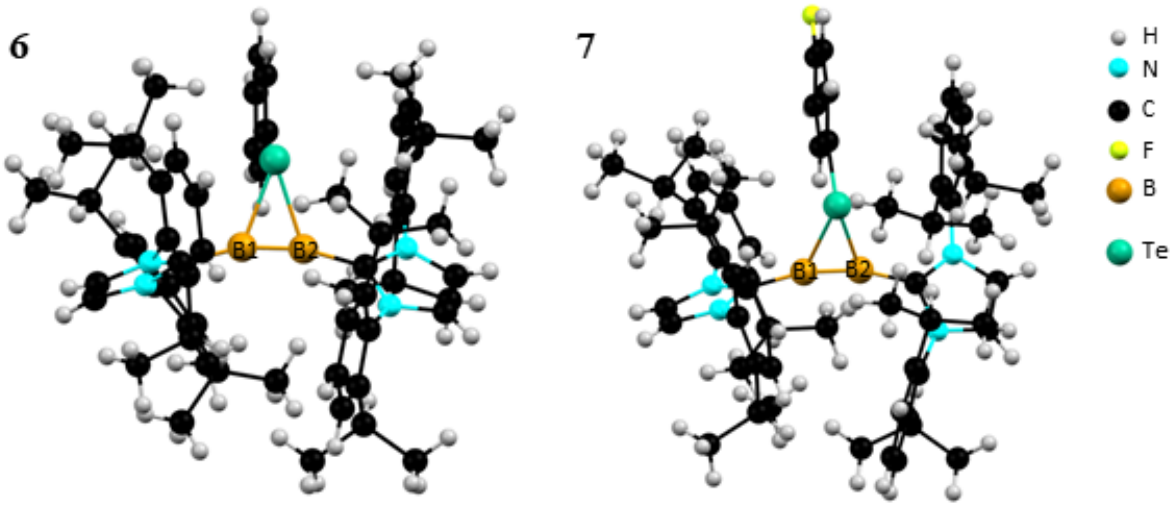

Figure 44 The crystal structures of the cations in the diboratellurenium compounds (**6** and **7**) investigated here. Both compounds consist of pairs of crystallographically, and therefore magnetically, inequivalent borons.

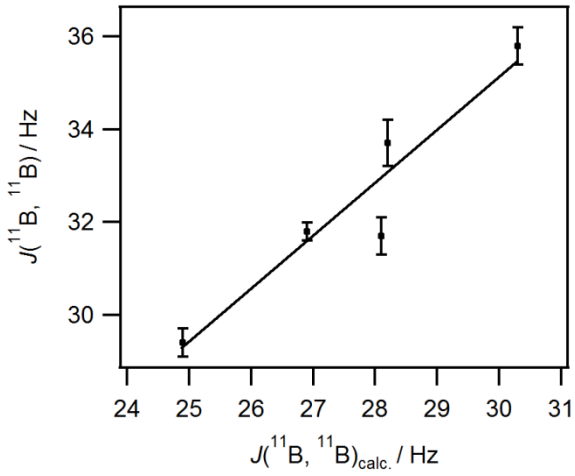

Figure 45 Correlation between the experimental and the calculated $J(^{11}B, ^{11}B)$ coupling constants for **1-5** ($J = 1.14J_{calc.} + 0.89$ Hz, $R^2 = 0.90$). The experimental values were obtained using ^{11}B DQF *J*-resolved SSNMR experiments and the theoretical values were calculated using revPBE/TZ2P. Data taken from Table 6.

The experimental $J(^{11}B, ^{11}B)$ coupling constants of the diboratellurenium compounds (171.4 Hz for **6** and 172.8 Hz for **7**) were found to be in agreement with the literature values for diboron compounds featuring multiply bonded boron spin pairs (ca. 75-187 Hz)[30]. On the other hand, the $J(^{11}B, ^{11}B)$ coupling constants for the $[B_2(CN)_6]^{2-}$ dianions were measured be consistently smaller than the previously studied B-B single bonds. The $J(^{11}B, ^{11}B)$ coupling constants for diboranes were found to range from 98 to 136 Hz,[29] while the *J* coupling constants of **1**-**5** were measured to range from 29.4 to 35.8 Hz, which is consistent with the value of 33.2 Hz as obtained by simulating the ABX pattern acquired from ^{13}C NMR of $[^{11}B_2(^{13}CN)(CN)_5]^{2-}$ in CD_3CN solution.[37] According to previous studies which correlated the $J(^{11}B, ^{11}B)$ coupling constants of diborane compounds with various electronic metrics, an increase in p-orbital contribution to the B-B bond can result in a decrease in the *J* coupling value.[29] Since the literature *J* values for diborane compounds were extracted from systems bearing $B(sp^x)$-$B(sp^x)$ bonds with $x \approx 1$-2, while the $[B_2(CN)_6]^{2-}$ dianions are expected to encompass $B(sp^3)$-$B(sp^3)$ bonds, the magnitude of the $J(^{11}B, ^{11}B)$ coupling for the dianions can be anticipated to be smaller. This rationale was further verified via NBO/NLMO analysis, which was conducted as to investigate the electronic origins of the *J* couplings and to relate the *J* coupling constants with the electronic features of the diboron compounds**.** Such analysis has been previously conducted on various diborane, diborene and diboryne systems,[29,30] and it was shown be successful at deconvoluting the *J* coupling constants into the corresponding electronic contributions and at providing insights into the relationship between the coupling constants and the structural and electronic features of the diboron compounds. Firstly, the *J* couplings were decomposed into their corresponding NLMO contributions in order to gain a greater understanding into the electronic origins of the interaction.

Table 7 The main NLMO contributions to the $J(^{11}B, ^{11}B)$ coupling constants of **1**-**7**.

sample	B core NLMO / %	B-B bonding NLMO / %
1	71.4	39.1
2	71.8	40.7
3	70.5	39.7
4	69.5	40.1
5	71.6	37.7
6[a]	61.8	49.3
7[a]	62.0	49.1

[a]The isopropyl groups of the IDip ligands were replaced with protons in the input structure used for calculations.

For all samples, the main NLMOs which contribute to *J* couplings were found to be the boron core orbitals (ca. 70 % for **1**-**5** and ca. 62 % for **6** and **7**) and the B-B σ-bonding orbitals (ca. 40 % for **1**-**5** and ca. 50 % for **6** and **7**) (Table 7), indicating that most of the *J* coupling originates from the FC mechanism. This is consistent with literature, which reports a ca. 50 % contribution from the boron core orbitals and the B-B σ-bonding orbitals, respectively, for diborane compounds,[29] and a ca. 60% contribution from boron core orbitals and a ca. 30% contribution from B-B σ-bonding orbitals for diborons with double and/or triple B-B bonds.[30] Furthermore, our results illustrate that the *J* coupling constants can be employed to assess the strength of the B-B bonds and the nature of the boron bonding orbitals. Similar to previous reports,[29] an inverse correlation was observed between the *J* coupling values and the p orbital contributions to the B-B bond and the $\sigma_{B\text{-}B}$ NBO energies (Table 6 and Figure 46). This is consistent with our NLMO analysis which revealed that the major NLMO contributions to these *J* couplings are from the FC mechanism (Table 7). Since only orbitals with significant s character can contribute to *J* coupling via the FC mechanism, compounds with greater p orbital contribution to the B–B bond would

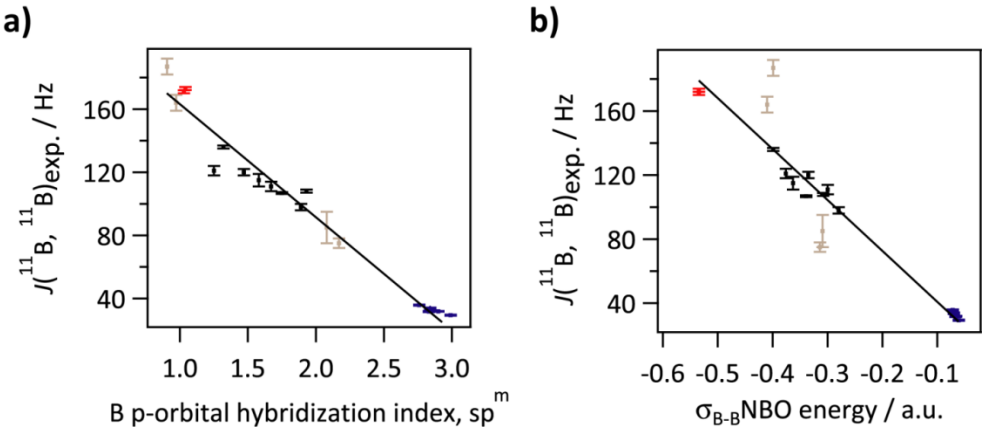

Figure 46 Correlation between the experimental $J(^{11}B, ^{11}B)$ coupling constants and (a) the degree of p-orbital hybridization, m, of the boron orbitals responsible for the B-B bonds (J = -71.7m+ 234 Hz, R^2 = 0.97) and (b) the B-B σ-bonding NBO energies (J = -318E_{NBO} + 9.00 Hz, R^2 = 0.89). The blue squares correspond to **1-5**, the red squares correspond to **6** and **7**, the black squares correspond to the diborane compounds studied in Ref. 29, and the beige squares correspond to the multiply bonded boron spin pairs investigated in Ref. 30. The data for **1-7** are also tabulated in Table 6.

therefore have smaller J coupling constants. Moreover, since an increase in bond strength can be expected from an increase in bond order, the B-B bond energy would then be anticipated to be strongly correlated to the magnitude of the J couplings. These results also explains the difference between the $J(^{11}B, ^{11}B)$ coupling constants of **1-5** and the larger values found in literature for other diborane systems. Previously investigations were conducted on B-B bonds formed from boron orbitals with p-hybridization index of ca. 1 to 2 and B-B σ-bonding NBO energies of ca. -0.3 to -0.4,[29] whereas **1-5** contains $B(sp^3)$-$B(sp^3)$ bonds and therefore the boron orbitals have a greater p-orbital character, and the corresponding B-B bonds are also weaker (NBO energies of ca. -0.07). Consequently, the $J(^{11}B, ^{11}B)$ coupling constants of the $[B_2(CN)_6]^{2-}$ salts can be expected to be smaller.

3.3 Determining the Bonding Structures of the Diboratellurenium Compounds

Since the $J(^{11}B, ^{11}B)$ coupling constants can be correlated to the hybridization state of the boron orbitals which participate in the B-B bond, this suggests that B-B bond orders can be directly extracted from the *J* coupling values. This has been illustrated previously for a diboryne that is stabilized by two N-heterocyclic carbenes (NHC, i.e. NHC→B≡B←NHC).[30] Köppe and Schnöckel argued based on the force constants extracted from vibrational data that this diboryne does not actually consist a B-B triple bond, but a 4-electron 4-center π bond (i.e. NHC=B=B=NHC);[75] whereas the Raman and relaxed forced constant study conducted by Böhnke et al. indicates that this diboryne encompasses a B-B triple bond.[76] Nevertheless, the $J(^{11}B, ^{11}B)$ coupling constant of the diboryne (187 Hz) measured by Perras et al. was found to be larger than that of diborenes (75-85 Hz) and a diboracumulene (164 Hz), revealing that the diboryne consists of a higher bond order.[30] Consequently, insights into the B-B bond order was attained via the $J(^{11}B, ^{11}B)$ coupling constants, and the borons in the diboryne were concluded to be triply bonded to each other. Recently, Braunschweig et al. synthesized a series of diboratellurenium compounds which consist of a three-membered B_2Te ring (**6** and **7** as shown in Figure 23) by nucleophilic attack of diaryltellurides with B_2IDip_2 (**8** of Figure 47; IDip = 1,3-bis[diisopropylphenyl]imidazole-2-ylidene).[38] As compared to **8**, both X-ray diffraction and Raman spectroscopy studies indicated a reduction in bond order upon the addition of the tellurium group.[38] X-ray diffraction revealed a B-B bond length of 1.490 Å for **6** and 1.494 Å for **7**, which is longer than the B≡B bond length in **8** (1.449 Å). This increase in bond length also manifested

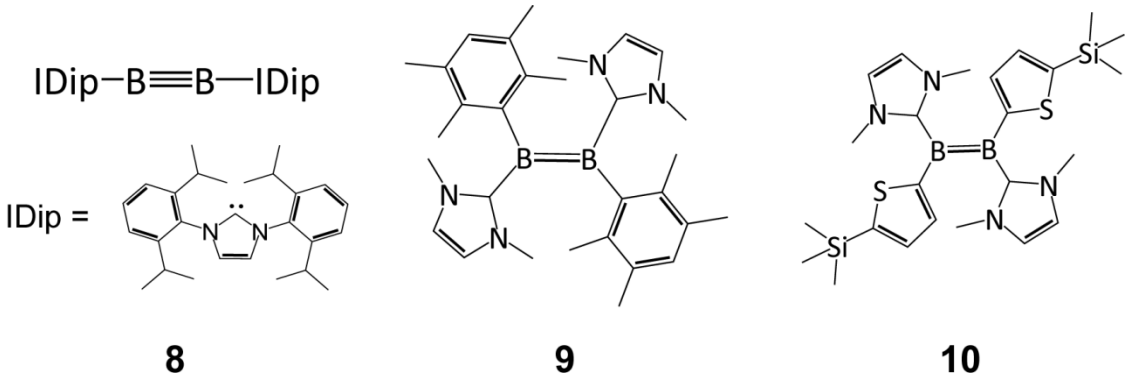

Figure 47 Structures of **8**, **9**, and **10**.

itself in the corresponding Raman spectra, in which the signals for the symmetric B-B stretch of **6** and **7** was found to be shifted to a lower wavenumber as compared to $B_2(IDip)_2$. Nevertheless, it is unclear from these data the degree of which the bond order is decreased, and therefore if the B-B bond in **6** and **7** are closer to a double or a triple bond. Since *J* coupling constants have been shown to be an ideal tool for probing bond orders, here, the $J(^{11}B, ^{11}B)$ coupling constants extracted using ^{11}B DQF *J*-resolved SSNMR spectroscopy were employed to determine the bonding structure of **6** and **7**.

The ^{11}B DQF *J*-resolved spectra of **6** and **7** are provided in Figure 43, and the $J(^{11}B, ^{11}B)$ coupling constants of **6** and **7** were measured to be 171.4 Hz and 172.8 Hz, respectively, (Table 8) which are in agreement with the DFT-calculated values (171.8 Hz for **6** and 171.5 Hz for **7**). In order to extract bonding information from the coupling constants, the measured values were compared to the literature values of **8** and also two NHC-stabilized diborenes (**9** and **10** of Figure 47). In agreement with the X-ray diffraction and the Raman spectroscopy results,[38] the coupling constants of **6** and **7** are smaller than that of **8** (Table 8), indicating that the B-B bond order is lowered upon the addition of the tellurium group. However, the B-B bond order is still larger

Table 8 The experimental $J(^{11}B, ^{11}B)$ coupling constants ($J(^{11}B, ^{11}B)_{exp.}$) and the p-orbital hybridization indexes of the B-B bonds (hybridization index) of **6**-**10**.

sample	$J(^{11}B, ^{11}B)_{exp.}$ / Hz	hybridization index
6	171.4 ± 0.6	1.03[b]
7	172.8 ± 0.7	1.04[b]
8[a]	187 ± 5	0.90
9[a]	85 ± 10	2.08
10[a]	75 ± 3	2.17

[a]Data obtained from Ref. 30. [b]The isopropyl groups of the IDip ligands were replaced with protons in the input structure used for calculations.

than that of a double bond since a stronger $J(^{11}B, ^{11}B)$ interaction was detected as compared to that of the diborenes (**9** and **10**, see Table 8). Nonetheless, the B-B bonding structure in **6** and **7** were concluded to be closer to a triple bond since the $J(^{11}B, ^{11}B)$ values of **6** and **7** (ca. 171-173 Hz) are more similar to that of **8** (187 Hz)[30] than those of **9** and **10** (75-85 Hz)[30]. The trend observed in the measured $J(^{11}B, ^{11}B)$ coupling constants of **6**-**10** is also reflected in the calculated boron p-orbital contributions to the B-B bond. As discussed in the previous section (section 3.2), the magnitude of the $J(^{11}B, ^{11}B)$ values correlates inversely with the p-orbital hybridization index of the boron orbitals responsible for the B-B bond. Here, an increase in the $J(^{11}B, ^{11}B)$ coupling constants can also be seen to be associated with a decrease in the boron p-orbital hybridization index (Table 8). Furthermore, similar to the *J* coupling values, the boron p-orbital hybridization index of **6** and **7** are closer to that of the diboryne than the diborenes. The B-B bonds of **6** and **7** are formed from $sp^{1.03\text{-}1.04}$ hybridized boron orbitals, whereas the B-B bonds of the diboryne and diborenes are formed from $sp^{0.90}$ and $sp^{2.08\text{-}2.17}$ borons,[30] respectively.

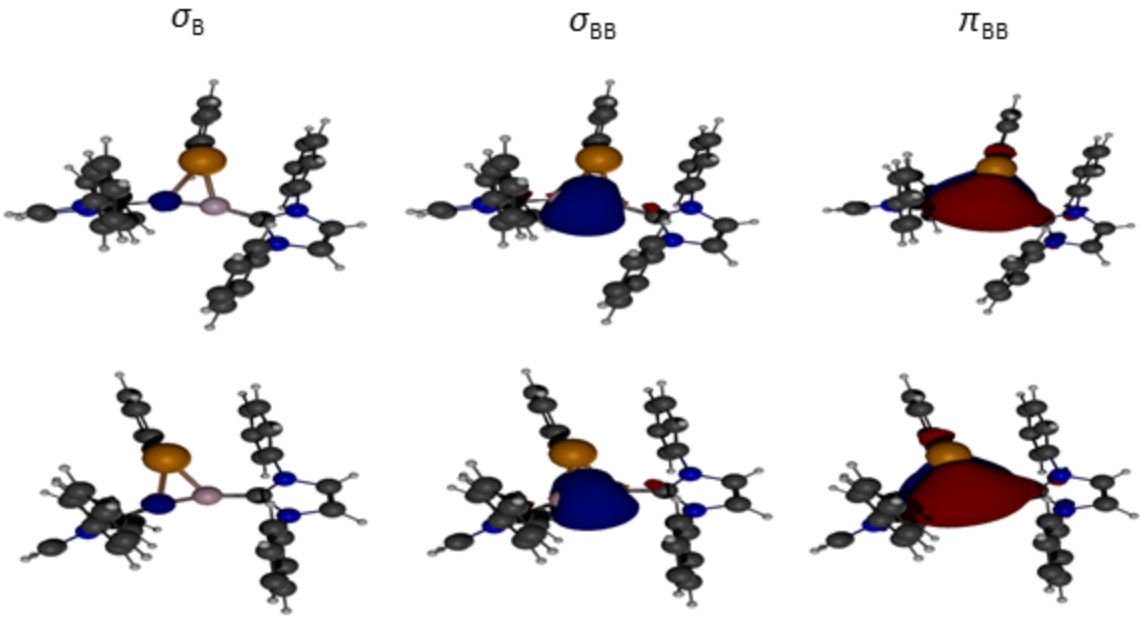

Figure 48 The boron core (σ_B), B-B σ-bonding (σ_{BB}), and B-B π-bonding (π_{BB}) NLMOs of **6** (top) and **7** (bottom). The isopropyl groups in the IDip ligands were replaced with protons.

According to literature,[30] an increase in the π-acidity of the ligands can result in a decrease in the $J(^{11}B, ^{11}B)$ coupling constants. For instance, the cyclic (alkyl)(amino)carbene (CAAC) ligands are more π-acidic than the IDip ligands.[77] Consequently, the π_{BB} NLMO is more delocalized towards the carbene ligand in $B_2(CAAC)_2$ as compared to $B_2(IDip)_2$, resulting in a smaller B-B bond order and a longer bond length.[30] This gives rise to a smaller $J(^{11}B, ^{11}B)$ coupling constant (164 Hz for $B_2(CAAC)_2$ and 187 Hz for $B_2(IDip)_2$) since a decrease in bond order would lead to a reduction in the FC contribution to the J coupling interaction, while an increase in bond length would lessen orbital overlap.[30] As the borons in **6** and **7** are bonded to a positively charge tellurium atom, we suspect that the slight decrease in the $J(^{11}B, ^{11}B)$ coupling constants and B-B bond orders as compared to $B_2(IDip)_2$ can also be justified using a similar rationale as the case of $B_2(CAAC)_2$ vs $B_2(IDip)_2$. In order to investigate this, NLMO analyses were conduct-

ed and the boron core (σ_B), B-B σ-bonding (σ_{BB}), and B-B π-bonding (π_{BB}) and the NLMOs of **6** and **7** are provided in Figure 48. As expected, π_{BB} NLMOs are delocalized toward the IDip ligands, which is consistent with what was previously observed in the NLMOs of $B_2(IDip)_2$.[30] More importantly, in agreement with what was hypothesized, the π_{BB} NLMOs are also delocalized towards the bridging Te. Consequently, the addition of a diaryltelluride group on the B≡B bond of $B_2(IDip)_2$ (therefore forming **6** and **7**) promotes delocalization of the π_{BB} electrons across the C-B-Te-B-C unit, thereby lengthening the B-B bond and reducing the B-B bond order, which then manifest itself into a decrease in the $J(^{11}B, ^{11}B)$ coupling constant through a decrease in the FC contribution and in orbital overlap.

4 Conclusion

In this work, molecular dynamics and electronic structures of a series of diboron compounds were explored via the *J* coupling interaction. The results demonstrate a novel approach for probing the presence of dynamics in solids and illustrate the applicability of the *J* coupling interaction in attaining bonding information. Using the diborane compounds as model systems, it is shown here that the DQF *J*-resolved experiments can provide valuable insights into the molecular motions and the structure of solids since if the crystallographic symmetry of the system is known *a priori*, the presence and/or absent of dynamic disorder can be confirmed based on the appearance of the spectra. Conversely, if *a priori* knowledge on the disorder type of the system (i.e. static vs dynamic) is attained, crystallographic symmetry of the system can be inferred from these experiments. Moreover, the measured $J(^{11}B, ^{11}B)$ coupling constants were found to strongly reflect various electronic features of the B-B bond, such as the bond strength and the bond order. A near linear correlation was found between these electronic parameters and the coupling constants, illustrating that the nature of chemical bonds can be directly characterized using the *J* coupling interaction. This is further demonstrated via the diboratellurenium complexes, where the B-B bond orders were determined from the magnitude of the $J(^{11}B, ^{11}B)$ coupling constants.

Given the growing interest in the synthesis of diboron compounds and the construction of solids with dynamics, this thesis demonstrates the strength of SSNMR-based methodologies for understanding these systems in atomic detail. Further expansion of the correlation data obtained in this thesis by the *J* coupling measurements of other novel diboron systems with different

bonding structures as the ones presented in this work, such as aromatic boron clusters[78] and the dicationic diboron(II) compounds[79], would allow the experimental $J(^{11}B, ^{11}B)$ coupling constants to become a routine tool for determining electronic features, thereby paving the way for a potential experimental substitute to quantum calculations. Moreover, this work describes a convenient method that can be employed to investigate various aspects of solid state structures (i.e. dynamics and crystallographic symmetry) and electronic features simultaneously. This can be beneficial for the synthesis of solids with dynamics (e.g. molecular machines) as it can determine the presence and/or absence of molecular motions as well as provide insights into the corresponding bonding structures and properties. Lastly, the methodology employed here is not just limited to the study of diboron compounds and can potentially be utilized for the characterization of other pairs of homonuclear quadrupolar nuclei with a CT, which includes many of the transition metals and main group elements employed in inorganic chemistry; thus, this thesis provides a solid foundation for the future characterization of inorganic materials, reagents and nanotechnologies.

References

(1) Balci, M. *Basic 1H- and 13C-NMR Spectroscopy*; First ed.; Elsevier B.V.: Amsterdam, Netherlands, 2005.

(2) Levitt, M. H. *Spin Dynamics Basics of Nuclear Magnetic Resonance*; John Wiley & Sons: England, 2008.

(3) Keeler, J. *Understanding NMR Spectroscopy*; Second ed.; John Wiley & Sons: United Kingdom, 2010.

(4) Apperley, D. C.; Harris, R. K.; Hodgkinson, P. *Solid-state NMR Basic Principles & Practice*; Momentum Press: New York, 2012.

(5) Duer, M. J. *Solid-State NMR Spectroscopy Principles and Applications*; Blackwell Science: UK, 2002.

(6) Pavia, D. L.; Lampman, G. M.; Kriz, C. S.; Vyvyan, J. R. *Introduction to Spectroscopy*; Fourth ed.; Brooks/Cole, Cengage Learning: USA, 2009, 2001.

(7) Widdifield, C. M.; Chapman, R. P.; Bryce, D. L. *Annu. Rep. NMR Spectrosc.* **2009**, *66*, 195-326.

(8) Ashbrook, S. E.; Wimperis, S. In *NMR Crystallography*; Harris, R. K., Wasylishen, R. E., Duer, M. J., Eds.; John Wiley & Sons: UK, 2009.

(9) Eichele, K. *WSolids1*, 1.20.18 ed. Universität Tübingen, 2012.

(10) Ramsey, N. F. *Phys. Rev.* **1953**, *91*, 303-307.

(11) *High Resolution NMR Spectroscopy: Understanding Molecules and Their Electronic Structures*; Elsevier B.V.: UK, 2013.

(12) *Multinuclear NMR*; Plenum Press: New York, 1987.

(13) Wasylishen, R. E. In *NMR Crystallography*; Harris, R. K., Wasylishen, R. E., Duer, M. J., Eds.; John Wiley & Sons: UK, 2009.

(14) Kalsi, P. S. *Spectroscopy of Organic Compounds*; 6th ed.; New Age International (P): New Delhi, 2004.

(15) Atta-ur-Rahman *Nuclear Magnetic Resonance: Basic Principles*; Springer-Verlag: New York, 1986.

(16) Haeberlen, U. *Advances in Magnetic Resonance*; Academic Press: New York, 1976.

(17) Bryant, R. G. *J. Chem. Educ.* **1983**, *60*, 933.

(18) Vold, R. L.; Hoatson, G. L. *J. Magn. Reson.* **2009**, *198*, 57-72.

(19) Karunaratne, C. V.; Weldeghiorghis, T. K.; West, C. M.; Taylor, C. M. *J. Am. Chem. Soc.* **2014**, *136*, 15170-15175.

(20) Li, X.; Hopmann, K. H.; Hudecová, J.; Isaksson, J.; Novotná, J.; Stensen, W.; Andrushchenko, V.; Urbanová, M.; Svendsen, J.-S.; Bouř, P.; Ruud, K. *J. Phys. Chem. A* **2013**, *117*, 1721-1736.

(21) Mandhapati, A. R.; Kato, T.; Matsushita, T.; Ksebati, B.; Vasella, A.; Böttger, E. C.; Crich, D. *The Journal of Organic Chemistry* **2015**, *80*, 1754-1763.

(22) Preimesberger, M. R.; Majumdar, A.; Aksel, T.; Sforza, K.; Lectka, T.; Barrick, D.; Lecomte, J. T. J. *J. Am. Chem. Soc.* **2015**, *137*, 1008-1011.

(23) Yamada, S.; Yamamoto, N.; Takamori, E. *The Journal of Organic Chemistry* **2016**, *81*, 11819-11830.

(24) Hung, I.; Uldry, A. C.; Becker-Baldus, J.; Webber, A. L.; Wong, A.; Smith, M. E.; Joyce, S. A.; Yates, J. R.; Pickard, C. J.; Dupree, R.; Brown, S. P. *J. Am. Chem. Soc.* **2009**, *131*, 1820-1834.

(25) Kobera, L.; Southern, S. A.; Rao, G. K.; Richeson, D. S.; Bryce, D. L. *Chem. Eur. J.* **2016**, *22*, 9565-9573.

(26) Perras, F. A.; Bryce, D. L. *J. Chem. Phys.* **2013**, *138*, 174202.

(27) Perras, F. A.; Bryce, D. L. *J. Am. Chem. Soc.* **2013**, *135*, 12596-12599.

(28) Perras, F. A.; Bryce, D. L. *J. Phys. Chem. Lett.* **2014**, *5*, 4049-4054.

(29) Perras, F. A.; Bryce, D. L. *Chem. Sci.* **2014**, *5*, 2428-2437.

(30) Perras, F. A.; Ewing, W. C.; Dellermann, T.; Böhnke, J.; Ullrich, S.; Schäfer, T.; Braunschweig, H.; Bryce, D. L. *Chem. Sci.* **2015**, *6*, 3378-3382.

(31) Wi, S.; Frydman, L. *J. Chem. Phys.* **2000**, *112*, 3248-3261.

(32) Blümich, B.; Haber-Pohlmeier, S.; Wasif, Z. *Compact NMR*; Walter de De Gruyter GmbH: Berlin Boston, 2014.

(33) Perras, F. A.; Bryce, D. L. *eMagRes* **2015**, *4*, 561-574.

(34) *Synthesis and Application of Organoboron Compounds*; Springer International Publishing: Switzerland, 2015; Vol. 49.

(35) Zhou, D.; Doumon, N. Y.; Abdu-Aguye, M.; Bartesaghi, D.; Loi, M. A.; Anton Koster, L. J.; Chiechi, R. C.; Hummelen, J. C. *RSC Adv.* **2017**, *7*, 27762-27769.

(36) Neeve, E. C.; Geier, S. J.; Mkhalid, I. A. I.; Westcott, S. A.; Marder, T. B. *Chem. Rev.* **2016**, *116*, 9091-9161.

(37) Landmann, J.; Sprenger, J. A. P.; Hailmann, M.; Bernhardt-Pitchougina, V.; Willner, H.; Ignat'ev, N.; Bernhardt, E.; Finze, M. *Angew. Chem. Int. Ed.* **2015**, *54*, 11259-11264.

(38) Braunschweig, H.; Constantinidis, P.; Dellermann, T.; Ewing, W. C.; Fischer, I.; Hess, M.; Knight, F. R.; Rempel, A.; Schneider, C.; Ullrich, S.; Vargas, A.; Woollins, J. D. *Angew. Chem. Int. Ed.* **2016**, *55*, 5606-5609.

(39) Harris, R. K. *Nuclear Magnetic Resonance Spectroscopy A Physicochemical View*; Pearson Education: England, 1983, 1986.

(40) Blümler, P.; Hafner, S. In *Encyclopedia of Analytical Chemistry*; John Wiley & Sons, Ltd: 2006.

(41) Head-Gordon, M. *J. Phys. Chem.* **1996**, *100*, 13213-13225.

(42) Wilson, P. J. *Annu. Rep. NMR Spectrosc.* **2003**, *49*, 117-168.

(43) Sholl, D. S.; Steckel, J. A. *Density Functional Theory A Practical Introduction*; John Wiley & Sons: Hoboken, New Jersey, 2009.

(44) Hohenberg, P.; Kohn, W. *Phys. Rev.* **1964**, *136*, B864-B871.

(45) Yates, J. R.; Pickard, C. J. In *NMR Crystallography*; Harris, R. K., Wasylishen, R. E., Duer, M. J., Eds.; John Wiley & Sons: United Kingdom, 2009.

(46) Perdew, J. P.; Burke, K.; Ernzerhof, M. *Phys. Rev. Lett.* **1996**, *77*, 3865-3868.

(47) Weinhold, F.; Landis, C. R. *Chem. Educ. Res. Pract. Eur.* **2001**, *2*, 91-104.

(48) Glendening, E. D.; Landis, C. R.; Weinhold, F. *WIREs Comput Mol Sci* **2012**, *2*, 1-42.

(49) Weinhold, F. *J. Comput. Chem.* **2012**, *33*, 2363-2379.

(50) Alain, A. E.; Shoji, Y.; Fukushima, T.; Bryce, D. L. *Inorg. Chem.* **2015**, *54*, 11889-11896.

(51) Xu, Y.; Viger-Gravel, J.; Korobkov, I.; Bryce, D. L. *J. Phys. Chem. C* **2015**, *119*, 27104-27117.

(52) Weinhold, F.; Landis, C. R. In *Discovering Chemistry with Natural Bond Orbitals*; John Wiley & Sons, Inc.: 2012, pp 155-175.

(53) Fung, B. M.; Khitrin, A. K.; Ermolaev, K. *J. Magn. Reson.* **2000**, *142*, 97-101.

(54) Bennett, A. E.; Rienstra, C. M.; Auger, M.; Lakshmi, K. V.; Griffin, R. G. *J. Chem. Phys.* **1995**, *103*, 6951-6958.

(55) Kentgens, A. P. M.; Verhagen, R. *Chem. Phys. Lett.* **1999**, *300*, 435-443.

(56) Bielecki, A.; Burum, D. P. *Journal of Magnetic Resonance, Series A* **1995**, *116*, 215-220.

(57) te Velde, G.; Bickelhaupt, F. M.; Baerends, E. J.; Fonseca Guerra, C.; van Gisbergen, S. J. A.; Snijders, J. G.; Ziegler, T. *J. Comput. Chem.* **2001**, *22*, 931-967.

(58) Glendening, E. D.; Badenhoop, J. K.; Reed, A. E.; Carpenter, J. E.; Bohmann, J. A.; Morales, C. M.; Weinhold, F. *NBO 5.0*; Theoretical Chemistry Institute, University of Wisconsin, Madison, WI, 2001.

(59) Glendening, E. D.; Badenhoop, J. K.; Reed, A. E.; Carpenter, J. E.; Bohmann, J. A.; Morales, C. M.; Landis, C. R.; Weinhold, F. *NBO 6.0*; Theoretical Chemistry Institute, University of Wisconsin, Madison, WI, 2013.

(60) Frisch, M. J.; Trucks, G. W.; Schlegel, H. B.; Scuseria, G. E.; Robb, M. A.; Cheeseman, J. R.; Scalmani, G.; Barone, V.; Petersson, G. A.; Nakatsuji, H.; Li, X.; Caricato, M.; Marenich, A.; Bloino, J.; Janesko, B. G.; Gomperts, R.; Mennucci, B.; Hratchian, H. P.; Ortiz, J. V.;

Izmaylov, A. F.; Sonnenberg, J. L.; Williams-Young, D.; Ding, F.; Lipparini, F.; Egidi, F.; Goings, J.; Peng, B.; Petrone, A.; Henderson, T.; Ranasinghe, D.; Zakrzewski, V. G.; Gao, J.; Rega, N.; Zheng, G.; Liang, W.; Hada, M.; Ehara, M.; Toyota, K.; Fukuda, K.; Hasegawa, J.; Ishida, M.; Nakajima, T.; Honda, Y.; Kitao, O.; Nakai, H.; Vreven, T.; Throssell, K.; Montgomery, J., J. A. ; Peralta, J. E.; Ogliaro, F.; Bearpark, M.; Heyd, J. J.; Brothers, E.; Kudin, K. N.; Staroverov, V. N.; Keith, T.; Kobayashi, R.; Normand, J.; Raghavachari, K.; Rendell, A.; Burant, J. C.; Iyengar, S. S.; Tomasi, J.; Cossi, M.; Millam, J. M.; Klene, M.; Adamo, C.; Cammi, R.; Ochterski, J. W.; Martin, R. L.; Morokuma, K.; Farkas, O.; Foresman, J. B.; Fox, D. J. *Gaussian 09, Revision B.01,*; Gaussian, Inc.: Wallingford CT, 2009.

(61) Bryce, D. L.; Wasylishen, R. E. *Inorg. Chem.* **2002**, *41*, 4131-4138.

(62) Harris, K. J.; Wasylishen, R. E. *Inorg. Chem.* **2009**, *48*, 2316-2332.

(63) Katz, M. J.; Aguiar, P. M.; Batchelor, R. J.; Bokov, A. A.; Ye, Z. G.; Kroeker, S.; Leznoff, D. B. *J. Am. Chem. Soc.* **2006**, *128*, 3669-3676.

(64) Kroeker, S.; Wasylishen, R. E.; Hanna, J. V. *J. Am. Chem. Soc.* **1999**, *121*, 1582-1590.

(65) Wu, G.; Kroeker, S.; Wasylishen, R. E. *Inorg. Chem.* **1995**, *34*, 1595-1598.

(66) Zhang, Y.; Lucier, B. E. G.; Huang, Y. *Phys. Chem. Chem. Phys.* **2016**, *18*, 8327-8341.

(67) Karlen, S. D.; Reyes, H.; Taylor, R. E.; Khan, S. I.; Hawthorne, M. F.; Garcia-Garibay, M. A. *Proc. Natl. Acad. Sci. USA* **2010**, *107*, 14973-14977.

(68) Khuong, T.-A. V.; Dang, H.; Jarowski, P. D.; Maverick, E. F.; Garcia-Garibay, M. A. *J. Am. Chem. Soc.* **2007**, *129*, 839-845.

(69) Zhu, K.; O'Keefe, C. A.; Vukotic, V. N.; Schurko, R. W.; Loeb, S. J. *Nat Chem* **2015**, *7*, 514-519.

(70) Ahumada, H.; Kurkiewicz, T.; Thrippleton, M. J.; Wimperis, S. *J. Phys. Chem. B* **2015**, *119*, 4309-4320.

(71) Harris, R. K.; Bowles, J.; Stephenson, I. R.; Wong, E. H. *Spectrochim. Acta A Mol. Spectrosc.* **1988**, *44*, 273-276.

(72) Griffin, J. M.; Miller, A. J.; Berry, A. J.; Wimperis, S.; Ashbrook, S. E. *Phys. Chem. Chem. Phys.* **2010**, *12*, 2989-2998.

(73) Xue, Y.; Pavlova, M. S.; Ryabov, Y. E.; Reif, B.; Skrynnikov, N. R. *J. Am. Chem. Soc.* **2007**, *129*, 6827-6838.

(74) Perras, F. A.; Bryce, D. L. *J. Magn. Reson.* **2014**, *242*, 23-32.

(75) Köppe, R.; Schnöckel, H. *Chem. Sci.* **2015**, *6*, 1199-1205.

(76) Böhnke, J.; Braunschweig, H.; Constantinidis, P.; Dellermann, T.; Ewing, W. C.; Fischer, I.; Hammond, K.; Hupp, F.; Mies, J.; Schmitt, H.-C.; Vargas, A. *J. Am. Chem. Soc.* **2015**, *137*, 1766-1769.

(77) Böhnke, J.; Braunschweig, H.; Ewing, W. C.; Hörl, C.; Kramer, T.; Krummenacher, I.; Mies, J.; Vargas, A. *Angew. Chem. Int. Ed.* **2014**, *53*, 9082-9085.

(78) Kupfer, T.; Braunschweig, H.; Radacki, K. *Angew. Chem. Int. Ed.* **2015**, *54*, 15084-15088.

(79) Kong, L.; Lu, W.; Li, Y.; Ganguly, R.; Kinjo, R. *J. Am. Chem. Soc.* **2016**, *138*, 8623-8629.

Appendix

A.1 Sample Input Files for the DFT Calculations of the Hexacyanodiborane(6) Dianion Salts

A.1.1 J Coupling and NLMO/NBO Calculations

```
#!/bin/bash
#$ -N test.run
#$ -S /bin/bash

#$ -m be

#$ -o test.out
#$ -e test.err

#$ -cwd
#$ -V

#$ -pe dist.pe 28

#!/bin/sh

$ADFBIN/adf << eor

ATOMS
 B                  1.52020000    0.81680000    8.92500000
 C                  1.93520000    2.25900000    9.45250000
 N                  2.21600000    3.28040000    9.85840000
 C                  2.81230000   -0.03020000    8.54590000
 N                  3.72970000   -0.65700000    8.30280000
 C                  0.55000000    0.95000000    7.66710000
 N                 -0.17770000    1.02140000    6.79310000
 B                  0.63840000   -0.03030000   10.22120000
 C                  0.22330000   -1.47240000    9.69380000
 N                 -0.05750000   -2.49390000    9.28790000
 C                 -0.65380000    0.81670000   10.60030000
 N                 -1.57120000    1.44350000   10.84350000
 C                  1.60850000   -0.16350000   11.47910000
```

```
 N                  2.33630000   -0.23490000   12.35320000
END

CHARGE -2

save TAPE15
FULLFOCK
AOMAT2FILE

BASIS
 type TZ2P
 core None
END

XC
  GGA revPBE
End

SCF
 converge 1.0e-8
END

SYMMETRY nosym

INTEGRATION
 accint 4.5
 accsph 5.5
end

end input
eor

$ADFBIN/adfnbo << eor
write
spherical
fock
TESTJOB
end input
eor

rm adfnbo.37 adfnbo.39 adfnbo.49 adfnbo.48
cp TAPE21 NLMO.t21
$ADFBIN/gennbo < FILE47

$ADFBIN/adfnbo << eor
 copy
 spherical
 fock
end input
```

```
eor

$ADFBIN/adfnbo << eor
 spherical
 fock
 read
end input
eor

rm adfnbo.37 adfnbo.39 adfnbo.49 adfnbo.48

rm TAPE15 TAPE21 TAPE13 logfile

$ADFBIN/cpl << eor
maxmemoryusage 40
nmrcoupling
atompert {1}
atomresp {8}
 dso
 pso
 sd
 fc
 scf {convergence=1e-7}
 contributions 1e19 nbo
end
endinput
eor

rm TAPE15 TAPE21 TAPE13 logfile

$ADFBIN/adf << eor
ATOMS
 B                  1.52020000    0.81680000    8.92500000
 C                  1.93520000    2.25900000    9.45250000
 N                  2.21600000    3.28040000    9.85840000
 C                  2.81230000   -0.03020000    8.54590000
 N                  3.72970000   -0.65700000    8.30280000
 C                  0.55000000    0.95000000    7.66710000
 N                 -0.17770000    1.02140000    6.79310000
 B                  0.63840000   -0.03030000   10.22120000
 C                  0.22330000   -1.47240000    9.69380000
 N                 -0.05750000   -2.49390000    9.28790000
 C                 -0.65380000    0.81670000   10.60030000
 N                 -1.57120000    1.44350000   10.84350000
 C                  1.60850000   -0.16350000   11.47910000
 N                  2.33630000   -0.23490000   12.35320000
END

CHARGE -2
```

```
BASIS
 Type TZ2P
 core None
END

XC
  GGA revPBE
End

SYMMETRY nosym

SCF
 converge 1.0e-8
END

INTEGRATION
 accint 4.5
 accsph 5.5
end

end input
eor

rm TAPE15

$ADFBIN/cpl << eor
maxmemoryusage 40
nmrcoupling
atompert {1}
atomresp {8}
 dso
 pso
 sd
 fc
 scf {convergence=1e-7}
 contributions 1e19 nbo
end
endinput
eor
```

A.1.2 CS and EFG Tensor Calculations

```
#! /bin/bash
#$ -S /bin/bash
#$ -q abaqus.q
#$ -l qname=abaqus.q
#$ -M ywong042@uottawa.ca
#$ -m be
#$ -e test.err
#$ -V
#$ -cwd
#$ -pe shm.pe 8
adf -n $NSLOTS <test.adf >test.log

#!/bin/sh

$ADFBIN/adf << eor
Title BMncat - scf

Basis
 Type TZ2P
 Core None
End

Symmetry NOSYM

Atoms
 B                  1.52020000    0.81680000    8.92500000
 C                  1.93520000    2.25900000    9.45250000
 N                  2.21600000    3.28040000    9.85840000
 C                  2.81230000   -0.03020000    8.54590000
 N                  3.72970000   -0.65700000    8.30280000
 C                  0.55000000    0.95000000    7.66710000
 N                 -0.17770000    1.02140000    6.79310000
 B                  0.63840000   -0.03030000   10.22120000
 C                  0.22330000   -1.47240000    9.69380000
 N                 -0.05750000   -2.49390000    9.28790000
 C                 -0.65380000    0.81670000   10.60030000
 N                 -1.57120000    1.44350000   10.84350000
 C                  1.60850000   -0.16350000   11.47910000
 N                  2.33630000   -0.23490000   12.35320000
End

Charge -2

Integration 6.0
```

```
qtens

XC
 GGA revPBE
End

SAVE TAPE10

End Input
eor

$ADFBIN/nmr << eor
NMR
 U1K BEST
 Out TENS
 Atoms 1 8
 SCF 1.d-4
END
Eor
```

A.2 Sample Input Files for the DFT Calculation of the Diboratellurenium Compounds

A.2.1 Geometry Optimization of the Diboratellurenium Cations

```
%chk=A1+2DITFB_Xray.chk
%mem=222MW
%nproc=8
# PBEPBE/3-21G opt=modredundant

A1+2DITFB_Xray

1 1
 Te -1              3.93720000    8.64620000   21.69220000
 C -1               6.34690000    9.10470000   19.36500000
 B -1               4.82750000    8.99870000   19.65900000
 N -1               7.17460000   10.15140000   19.63160000
 B -1               3.34230000    8.97000000   19.53580000
 C -1               8.43640000    9.91810000   19.11270000
 H                  9.18470000   10.50070000   19.16640000
 C -1               8.40590000    8.71170000   18.51660000
 H                  9.12210000    8.28380000   18.06490000
 C -1               6.83400000   11.33280000   20.40360000
 N -1               7.12060000    8.21270000   18.69290000
 C -1               6.48600000   12.49930000   19.73120000
 C -1               6.31820000   13.56720000   21.90580000
 H                  6.14630000   14.34820000   22.41980000
 C -1               6.21520000   13.61840000   20.53480000
 H                  5.95460000   14.43180000   20.12100000
 C -1               6.66620000   12.39950000   22.53610000
 H                  6.71270000   12.37450000   23.48300000
 C -1               6.95160000   11.24550000   21.80240000
 H                  6.46730000   12.71760000   18.22740000
 H                  7.47770000    9.99790000   22.48910000
 C -1               7.32370000    5.84480000   19.22480000
 C -1               6.76690000    6.83660000   18.40330000
 C -1               7.00630000    4.53240000   18.92240000
 H                  7.35270000    3.83500000   19.46650000
 C -1               5.67090000    5.20730000   17.05150000
 H                  5.11570000    4.97530000   16.31520000
 C -1               6.20340000    4.20930000   17.85290000
 H                  6.01240000    3.29850000   17.66260000
```

```
 H                  8.21880000    6.15800000   20.42180000
 C -1               5.94450000    6.54590000   17.31550000
 H                  5.39430000    7.62130000   16.38540000
 C -1               2.89180000   12.95340000   16.36210000
 H                  3.11740000   13.18170000   15.46910000
 C -1               3.08090000   13.87910000   17.35730000
 H                  3.44060000   14.73240000   17.14850000
 C -1               2.74660000   13.56970000   18.66260000
 H                  2.88890000   14.21970000   19.34200000
 C -1               2.20870000   12.33090000   19.01280000
 C -1               2.05700000   11.40020000   17.96170000
 H                  0.32040000    8.65310000   22.14690000
 H                  0.88430000    5.73500000   17.97830000
 C -1               0.49720000    7.29450000   21.50480000
 C -1               0.39320000    6.12430000   22.24520000
 H                  0.26810000    6.17920000   23.18610000
 C -1               0.46640000    4.88420000   21.64530000
 H                  0.39490000    4.10200000   22.17720000
 C -1               0.64030000    4.76690000   20.29060000
 H                  0.67610000    3.90240000   19.89750000
 C -1               0.76540000    5.89720000   19.48210000
 C -1               0.72780000    7.13850000   20.12650000
 N -1               1.39920000   10.14390000   18.27340000
 C -1               0.05010000    9.95180000   18.02270000
 H                 -0.50840000   10.51320000   17.49650000
 C -1              -0.32750000    8.83520000   18.65620000
 H                 -1.19890000    8.45600000   18.66190000
 N -1               0.78960000    8.33370000   19.30050000
 C -1               1.87510000    9.12960000   19.05780000
 C -1               2.37670000   11.68460000   16.63190000
 H                  1.74320000   12.06270000   20.42720000
 H                  2.17470000   10.69910000   15.49370000
 C -1               3.93080000    6.50730000   21.97250000
 C -1               3.99600000    5.65020000   20.88950000
 H                  4.05310000    5.99330000   20.00610000
 C -1               3.97650000    4.27790000   21.11400000
 H                  4.01890000    3.67910000   20.37640000
 C -1               3.89330000    3.77890000   22.40200000
 H                  3.87540000    2.83940000   22.54440000
 C -1               3.83610000    4.63220000   23.47830000
 H                  3.77900000    4.28790000   24.36110000
 C -1               3.86380000    6.00700000   23.26080000
 H                  3.83590000    6.60460000   24.00030000


I     0
S   5   1.00
 444750.0000000             0.0008900
  66127.0000000             0.0069400
```

```
  14815.0000000             0.0360900
   4144.9000000             0.1356800
   1361.2000000             0.3387800
S   2   1.00
    508.4400000             0.4365900
    209.5900000             0.1837500
S   1   1.00
     81.9590000             1.0000000
S   1   1.00
     36.8050000             1.0000000
S   1   1.00
     13.4950000             1.0000000
S   1   1.00
      6.8859000             1.0000000
S   1   1.00
      2.5520000             1.0000000
S   1   1.00
      1.2088000             1.0000000
S   1   1.00
      0.2734000             1.0000000
S   1   1.00
      0.1009000             1.0000000
P   4   1.00
   2953.6000000             0.0122100
    712.6100000             0.0858700
    236.7100000             0.2949300
     92.6310000             0.4784900
P   1   1.00
     39.7320000             1.0000000
P   1   1.00
     17.2730000             1.0000000
P   1   1.00
      7.9570000             1.0000000
P   1   1.00
      3.1529000             1.0000000
P   1   1.00
      1.3328000             1.0000000
P   1   1.00
      0.4947000             1.0000000
P   1   1.00
      0.2160000             1.0000000
P   1   1.00
      0.0829300             1.0000000
D   3   1.00
    261.9500000             0.0314400
     76.7340000             0.1902800
     27.5510000             0.4724700
D   1   1.00
     10.6060000             1.0000000
```

```
D   1   1.00
      3.4217000              1.0000000
D   1   1.00
      1.1370000              1.0000000
D   1   1.00
      0.3020000              1.0000000
****
O     0
S   6   1.00
   8588.5000000              0.00189515
   1297.2300000              0.0143859
    299.2960000              0.0707320
     87.3771000              0.2400010
     25.6789000              0.5947970
      3.7400400              0.2808020
SP   3   1.00
     42.1175000              0.1138890              0.0365114
      9.6283700              0.9208110              0.2371530
      2.8533200             -0.00327447             0.8197020
SP   1   1.00
      0.9056610              1.0000000              1.0000000
SP   1   1.00
      0.2556110              1.0000000              1.0000000
D   1   1.00
      1.2920000              1.0000000
****
B Te N C H 0
6-311G**
****
```

A.2.2 J Coupling and NLMO/NBO Calculations

```
#!/bin/bash
#$ -S /bin/bash
#$ -q abaqus.q
#$ -l qname=abaqus.q
#$ -M ywong042@uottawa.ca
#$ -m be
#$ -e test.err
#$ -V
#$ -cwd
#$ -pe shm.pe 8
adf -n $NSLOTS <test.adf>test.log

#!/bin/sh

$ADFBIN/adf << eor

ATOMS
 1  Te                0.35282200   -0.05602700   -1.63435000
 2  C                -1.18745900   -2.06692800    0.60541500
 3  B                -0.65548500   -0.64527900    0.28577800
 4  N                -2.31369100   -2.66095800    0.12533800
 5  B                -0.29941200    0.80058100    0.35301700
 6  C                -2.51460000   -3.88712800    0.73522900
 7  H                -3.36346500   -4.51387400    0.49203400
 8  C                -1.50406900   -4.07038300    1.60523500
 9  H                -1.27772800   -4.89018000    2.27496800
 10 C                -3.17149700   -2.14027800   -0.92383300
 11 N                -0.68418800   -2.95246200    1.50460500
 12 C                -4.34142300   -1.47701200   -0.56985900
 13 C                -4.81517400   -1.28406700   -2.94384000
 14 H                -5.47699300   -0.93999000   -3.74253500
 15 C                -5.15003400   -1.04101300   -1.63171700
 16 H                -6.07777600   -0.51051800   -1.39939300
 17 C                -3.65367300   -1.94355700   -3.25672100
 18 H                -3.39367800   -2.12945600   -4.30218100
 19 C                -2.79976300   -2.40824500   -2.25353200
 20 H                -4.59151800   -1.28308900    0.47271900
 21 H                -1.87464200   -2.94056800   -2.47443000
 22 C                 1.62249400   -3.73067300    1.57332800
 23 C                 0.63377200   -2.88968900    2.10599100
 24 C                 2.86870600   -3.68761500    2.17306600
 25 H                 3.66742900   -4.31950600    1.77467500
 26 C                 2.12791900   -2.06163700    3.76883500
 27 H                 2.33381200   -1.42394200    4.63213800
 28 C                 3.12376900   -2.87851100    3.25619300
```

```
 29 H                  4.11454600   -2.88165600    3.71703000
 30 H                  1.41195000   -4.36393200    0.71122500
 31 C                  0.85878900   -2.05266000    3.19819300
 32 H                  0.05657900   -1.41913700    3.57715400
 33 C                 -4.67111300    2.43418900    2.44164100
 34 H                 -5.20726400    2.34248400    3.39066100
 35 C                 -5.36423200    2.36244000    1.25946400
 36 H                 -6.44739700    2.21976100    1.26720100
 37 C                 -4.69550800    2.49201400    0.05642200
 38 H                 -5.25919700    2.44790400   -0.88013800
 39 C                 -3.31758300    2.70271900   -0.00298400
 40 C                 -2.64142700    2.74244500    1.23607300
 41 H                  1.59370800    3.23411300   -1.93898300
 42 H                  2.98601800    2.56359700    2.11610900
 43 C                  2.41273800    2.99570200   -1.26084200
 44 C                  3.71023200    2.76345800   -1.69781600
 45 H                  3.92979600    2.82170900   -2.76712100
 46 C                  4.72678200    2.47244800   -0.81179800
 47 H                  5.73360500    2.28869200   -1.19325400
 48 C                  4.48809400    2.40765500    0.53655000
 49 H                  5.30856000    2.18913800    1.22515600
 50 C                  3.20772100    2.61704300    1.05007000
 51 C                  2.19158700    2.86952000    0.12205100
 52 N                 -1.22691100    3.06921700    1.21346300
 53 C                 -0.77828800    4.35874300    1.44944100
 54 H                 -1.43884500    5.12789100    1.83008500
 55 C                  0.51010700    4.41412300    1.09213200
 56 H                  1.21689100    5.23395400    1.10703900
 57 N                  0.86120500    3.15651300    0.63422000
 58 C                 -0.20593400    2.30522200    0.71900800
 59 C                 -3.28861100    2.62378700    2.46836100
 60 H                 -2.77722300    2.81797900   -0.94168300
 61 H                 -2.72544000    2.67770200    3.40030300
 62 C                  2.43660800   -0.55561300   -1.38585100
 63 C                  2.98393000   -0.70671000   -0.12514900
 64 H                  2.35311000   -0.58265500    0.76239000
 65 C                  4.33471000   -1.01660000   -0.00961100
 66 H                  4.77532600   -1.14339300    0.98381800
 67 C                  5.11809200   -1.17134700   -1.13975900
 68 H                  6.17900400   -1.41686700   -1.03292000
 69 C                  4.57091300   -1.02821600   -2.39272400
 70 H                  5.18403200   -1.15964400   -3.28849500
 71 C                  3.21739200   -0.72639200   -2.51532800
 72 H                  2.77584300   -0.61921000   -3.51273300
END

CHARGE 1

save TAPE15
```

```
FULLFOCK

AOMAT2FILE
BASIS
 type ZORA/TZP
 core None
END

XC
 GGA PBE
END

SCF
 converge 1.0e-8
END

SYMMETRY nosym

BeckeGrid
 Quality good
end

relativistic scalar zora

end input
eor


$ADFBIN/adfnbo << eor
write
spherical
fock
TESTJOB
end input
eor

rm adfnbo.37 adfnbo.39 adfnbo.49 adfnbo.48

$ADFBIN/gennbo6 FILE47

$ADFBIN/adfnbo << eor
 copy
 spherical
 fock
end input
eor

$ADFBIN/adfnbo << eor
```

```
 spherical
 fock
 read
end input
eor

rm adfnbo.37 adfnbo.39 adfnbo.49 adfnbo.48
rm TAPE15 TAPE21 TAPE13 logfile

$ADFBIN/cpl << eor
nmrcoupling
 xalpha
 dso
 pso
 sd
 scf convergence 1e-5 iterations 10
 contributions 1e19 nbo
 nuclei 38 39
end
endinput
eor

rm TAPE15 TAPE21 TAPE13 logfile

$ADFBIN/adf << eor
ATOMS
 1  Te                0.35282200   -0.05602700   -1.63435000
 2  C                -1.18745900   -2.06692800    0.60541500
 3  B                -0.65548500   -0.64527900    0.28577800
 4  N                -2.31369100   -2.66095800    0.12533800
 5  B                -0.29941200    0.80058100    0.35301700
 6  C                -2.51460000   -3.88712800    0.73522900
 7  H                -3.36346500   -4.51387400    0.49203400
 8  C                -1.50406900   -4.07038300    1.60523500
 9  H                -1.27772800   -4.89018000    2.27496800
 10 C                -3.17149700   -2.14027800   -0.92383300
 11 N                -0.68418800   -2.95246200    1.50460500
 12 C                -4.34142300   -1.47701200   -0.56985900
 13 C                -4.81517400   -1.28406700   -2.94384000
 14 H                -5.47699300   -0.93999000   -3.74253500
 15 C                -5.15003400   -1.04101300   -1.63171700
 16 H                -6.07777600   -0.51051800   -1.39939300
 17 C                -3.65367300   -1.94355700   -3.25672100
 18 H                -3.39367800   -2.12945600   -4.30218100
 19 C                -2.79976300   -2.40824500   -2.25353200
 20 H                -4.59151800   -1.28308900    0.47271900
 21 H                -1.87464200   -2.94056800   -2.47443000
 22 C                 1.62249400   -3.73067300    1.57332800
 23 C                 0.63377200   -2.88968900    2.10599100
```

24	C	2.86870600	-3.68761500	2.17306600
25	H	3.66742900	-4.31950600	1.77467500
26	C	2.12791900	-2.06163700	3.76883500
27	H	2.33381200	-1.42394200	4.63213800
28	C	3.12376900	-2.87851100	3.25619300
29	H	4.11454600	-2.88165600	3.71703000
30	H	1.41195000	-4.36393200	0.71122500
31	C	0.85878900	-2.05266000	3.19819300
32	H	0.05657900	-1.41913700	3.57715400
33	C	-4.67111300	2.43418900	2.44164100
34	H	-5.20726400	2.34248400	3.39066100
35	C	-5.36423200	2.36244000	1.25946400
36	H	-6.44739700	2.21976100	1.26720100
37	C	-4.69550800	2.49201400	0.05642200
38	H	-5.25919700	2.44790400	-0.88013800
39	C	-3.31758300	2.70271900	-0.00298400
40	C	-2.64142700	2.74244500	1.23607300
41	H	1.59370800	3.23411300	-1.93898300
42	H	2.98601800	2.56359700	2.11610900
43	C	2.41273800	2.99570200	-1.26084200
44	C	3.71023200	2.76345800	-1.69781600
45	H	3.92979600	2.82170900	-2.76712100
46	C	4.72678200	2.47244800	-0.81179800
47	H	5.73360500	2.28869200	-1.19325400
48	C	4.48809400	2.40765500	0.53655000
49	H	5.30856000	2.18913800	1.22515600
50	C	3.20772100	2.61704300	1.05007000
51	C	2.19158700	2.86952000	0.12205100
52	N	-1.22691100	3.06921700	1.21346300
53	C	-0.77828800	4.35874300	1.44944100
54	H	-1.43884500	5.12789100	1.83008500
55	C	0.51010700	4.41412300	1.09213200
56	H	1.21689100	5.23395400	1.10703900
57	N	0.86120500	3.15651300	0.63422000
58	C	-0.20593400	2.30522200	0.71900800
59	C	-3.28861100	2.62378700	2.46836100
60	H	-2.77722300	2.81797900	-0.94168300
61	H	-2.72544000	2.67770200	3.40030300
62	C	2.43660800	-0.55561300	-1.38585100
63	C	2.98393000	-0.70671000	-0.12514900
64	H	2.35311000	-0.58265500	0.76239000
65	C	4.33471000	-1.01660000	-0.00961100
66	H	4.77532600	-1.14339300	0.98381800
67	C	5.11809200	-1.17134700	-1.13975900
68	H	6.17900400	-1.41686700	-1.03292000
69	C	4.57091300	-1.02821600	-2.39272400
70	H	5.18403200	-1.15964400	-3.28849500
71	C	3.21739200	-0.72639200	-2.51532800
72	H	2.77584300	-0.61921000	-3.51273300

```
END

CHARGE 1

BASIS
 type ZORA/TZP
 core None
END

XC
 GGA PBE
END

SYMMETRY nosym

SCF
 converge 1.0e-8
END

BeckeGrid
 Quality good
end

relativistic spinorbit zora

end input
eor

rm TAPE15

$ADFBIN/cpl << eor
nmrcoupling
 xalpha
 dso
 pso
 sd
 scf convergence 1e-5 iterations 10
 contributions 1e19 nbo
 nuclei 39 38
end
end input
eor
```